An Experimental Investigation on the Strength and Failure Behavior of Freshwater Ice Rubble

By

Hamid Shayanfar

A Thesis submitted to the

School of Graduate Studies

In partial fulfillment of the requirements for the degree of

Master of Engineering

Faculty of Engineering and Applied Science

Memorial University of Newfoundland

March 2018

St. John’s, Newfoundland and Labrador, Canada

This page is intentionally left blank

ABSTRACT

Ice ridges are common features in Arctic and sub-Arctic regions. They are large accumulations (typically 5-30*m*) of ice rubble formed due to compressive or shear forces in ice cover. Understanding the deformation behavior and strength of ice rubble is key to estimating ice ridge loads on offshore structures. Medium-scale punch tests were conducted at C-CORE's Cold Room facility to measure and observe the strength and failure behavior of freshwater ice rubble. A custom-built punch box measuring 3.05*m* in length and 0.94*m* in width and height was used to perform the tests. The box walls were made from Plexiglas so that failure mechanisms could be observed. Ice rubble beams of nominal thickness 50*cm* were produced by placing randomly sized ice pieces into the punch box, filled with water at its freezing temperature. After a specified consolidation time and rubble confinement, the ice rubble beam was deformed by pushing a platen vertically downwards though the center of the beam until failure. In this study the effects of consolidation time, pressure confinement, sintering process and small ice block dimensions on the strength and failure behavior of freshwater ice rubble beam were investigated. Results showed that the failure behavior of the ice rubble beam is controlled by the degree of freeze bonding between the blocks.

KEY WORDS

Ice rubble; Ridges; Freeze-bonds (FBs), Consolidation time; Pressure confinement; Sintering, Shear strength; Flexural strength

ACKNOWLEDGEMENT

It is a humbling experience to acknowledge those people who have, mostly out of kindness, helped along the journey of my Master's. I am indebted to so many for encouragement and support.

First and foremost, I would like to express my sincere gratitude to my supervisors, Dr. Rocky Taylor and Dr. Eleanor Bailey, for their continuous support, guidance, help and understanding throughout the project, as the successful completion of this work would not have happened without their help.

Special thanks to Robert Pritchett for designing and constructing the laboratory apparatus and helping me with conducting the tests. I am also grateful for his technical expertise ability to solve any problems that arose.

I would also like to extend my thanks to Ken Croasdale for his valuable suggestions and advice during this project.

Many thanks to the following work-term students, Timothy Purdy, Dustin Francis, Harrison Lake, Claudia Joy, Toni Jerrett, Zoe Collins and Zachary Burt, who helped to prepare ice samples in a -20℃ Cold Room, conducting the tests and analyzing data.

A big thanks to all my colleagues and friends at C-CORE, Marjan Taghi Boroojerdi, Reza Zeinali, Soroush Afzali, Renat Yulmetov, Ian Turnbull, Mohamed Aly, and Robert Sarracino for their friendly help and support during this program at C-CORE.

My gratitude also extends to my friends, Javad Hashemi and Alireza Dehghani, for providing me with deep knowledge and expertise in writing my proposal.

None of this would have been possible without the financial support of the Hibernia Management and Development Company, Ltd (HMDC), Research and Development Corporation of Newfoundland and Labrador (RDC), Centre for Cold Ocean Resources Engineering (C-CORE), and Memorial University of Newfoundland, Faculty of Engineering and Applied Sciences, School of Graduate Studies (SGS).

I would also like to thank my sister and brother-in-law, Farzaneh and Amir, for their help, support and encouragement in every moment of this journey.

Last but by no means least, I thank my parents. They raised me, taught me, loved me, encouraged me and supported me to reach the position that I am now in. To them I dedicate this thesis.

TABLE OF CONTENTS

LIST OF TABLES

LIST OF FIGURES

CHAPTER 2

CHAPTER 3

CHAPTER 4

CHAPTER 5

CHAPTER 6

APPENDIX A

APPENDIX B

APPENDIX C

APPENDIX D

APPENDIX E

APPENDIX F

APPENDIX G

APPENDIX H

NOMENCLATURE

τ	Shear strength
$\sigma_{flexural}$	Flexural strength
σ_n	Normal stress
σ_1	Major principle stress
σ_2	Minor principle stress
F_{peak}	Peak load at failure
F_{B}	Buoyancy force
F_{max}	Maximum net force
F_{net}	Net force
F_{H}	The load measured by load cell
F_{R}	Residual force
F_{I}	Inertia force
p	Mean pressure
E_{eff}	Effective Young's modulus
c	Cohesion
$\emptyset$	Angle of internal friction
$\emptyset'$	Effective angle of internal friction
$\emptyset_m$	Mobilized angle of internal friction
T_0	Initial ice block temperature at the time of submersion
T_a	Ambient air temperature
T_{eq}	Equilibrium temperature
ρ_{w}	Density of water
g	Gravity
δ	Water level displacement during the ice rubble beam deformation
V_{b}	Nominal volume of submerged ice beam during deformation
V_{s}	Submerged volume of ice rubble beam before the test (after consolidation)
Δh	Change in water level during filling the box by ice blocks
h_1	Water level before filling the box

h_2	Water level after filling the box
y_0	Height of water level before the test
y	Height of water level at the time of beam failure
m_{ice}	Mass of ice
η	Beam porosity (Volume)
η'	Beam porosity (Area)
d	Corresponding beam deflection
A	Projected failure area
S	The area of beam deformation at underside of the beam
W	Ice rubble beam width
H	Ice rubble beam thickness
H_s	Submerged depth of the ice rubble beam
l	Box length
w	Box width
B	Platen width
e	The distance from the edge of the platen to the support (bracket)
H_k	Ice ridge keel depth
H_s	Ice ridge sail height
W_k	Ice ridge keel width
W_s	Ice ridge sail width
t_{eq}	Equilibrium time
A_{platen}	Platen area
$A_{ice(avg)}$	The average area of individual ice block
A_{box}	Horizontal area of the box
n	Number of ice blocks interacted with platen
R	The ratio of the platen width to the box length

1 Introduction

1.1 Background

With global population growth the demand for energy is ever increasing. Despite increased development of renewable energy sources, oil and gas will continue to play a key role. Hydrocarbons are predicted to provide about two-thirds of our energy demand in the following decades (Energy outlook, 2015). The U.S. Geological Survey (USGS) has estimated reservoirs of undiscovered oil and gas of up to 90 billion barrels of oil, 1.7 trillion cubic feet of natural gas, and 44 billion barrels of natural gas liquids in the Arctic and sub-Arctic; approximately 84 percent is expected to be in offshore areas (USGS, 2008). It is estimated that there are more than six billion barrels of oil and 60 trillion cubic feet of natural gas in offshore Newfoundland and Labrador (CAPP, 2015). This plays an important role in the province, since 28.4% of its 2014 Gross Domestic Product (GDP) was related to oil and gas extraction (The Economy, 2015).

In addition to the hydrocarbon potential, with the decline in sea ice Arctic shipping is becoming more economically viable linking the European and Asian markets (Guy and Lasserre, 2016), as well as increasing business opportunities in tourism and fishing. While these new resources and shipping routes present great economic opportunities for Northern countries, many challenges remain. These challenges include harsh environmental conditions, such as low temperatures, dark winters, ice and remoteness.

First-year (FY) ice ridges are one of the most common features in Arctic and sub-Arctic regions, as they consist of 10-40% of the volume of the sea ice (Leppäranta, 2011). As such they impact the design of ships, offshore structures and subsea infrastructures. The

failure mechanics of ice ridges are more complicated than those of solid ice, since ice ridges are accumulations of rubble that form in a highly random manner. The bottom side of an ice ridge, termed the "ice keel," may scour the seabed, threatening the integrity of pipelines and other subsea infrastructure, especially in shallow waters. Remote sensing techniques can be used to help determine the geometric and spatial characteristics of ice ridges. Estimating the loads caused by these ice ridges requires knowledge of the mechanical properties of ice rubble. Many experiments have been conducted on mechanical properties of solid ice, but their application to ice rubble and ridges are not well understood due to the rubble structure's inherent complexity. Therefore, developing insight into the deformation behaviour and strength of ice rubble and ridges is important for evaluating risks to offshore structures.

1.2 Purpose

This thesis presents the results of a series of medium-scale laboratory ice rubble experiments conducted to gain insights into the inhomogeneity of ice rubble and associated mechanical characteristics. During these experiments, a plate was pushed vertically down through an ice rubble beam to measure its average strength. The aim of this work is to investigate the effects of confining pressure, consolidation time, sintering and block size on the strength and failure behaviour of ice rubble. For this study, advanced instrumentation, such as a High Speed Video camera (HSV) and Micro-Ts temperature loggers, were used to provide insights into the development of ice ridge strength, its failure behavior, as well as its thermo-physical aspects.

In Chapter 2, a literature review was conducted covering previous investigations of the mechanical characteristics of ice rubble and ice ridges, with a focus on test methodologies and corresponding results. This chapter has been sectioned based on the test scale. First, tests conducted on microscopic scale to investigate the mechanical characteristics of freeze bonds in ice block-block contacts are described. Next, special attention was paid to highlighting the effects of various parameters on the behavior of ice rubble and ridges in medium-scale laboratory tests and field tests. The final part of this chapter describes parameters that this study intends to investigate in further detail using the ice rubble beam test.

Chapter 3 describes the test procedure, setup at C-CORE's Cold Room facility, and also the instrumentation and measurement equipment that were employed during this study. In this chapter, special attention was given to describing the ice blocks' preparation and image processing analysis.

The failure behavior for each test phase is described in Chapter 4, where Phase I corresponds to consolidation time tests, phase II to pressure confinement tests, Phase III to sintering tests and Phase IV to the small ice blocks test. Then, the results of load-displacements as well as a schematic of the locations of the ice rubble beam failures are shown and discussed. Later the temperature data for blocks, air and water for representative tests in the different phases are given.

In Chapter 5, the methods used for measuring the mechanical characteristics of ice rubble beam, such as porosity, buoyancy force and strength are described. The effects of ice

blocks positioning and their dimensions on reaching the equilibrium temperature are also discussed in this chapter.

In Chapter 6, the effects of consolidation time, pressure confinement, the sintering process and the small ice blocks on the strength of ice rubble beam are compared. Also, the failure behaviors of the ice rubble beam on both microscopic and macroscopic scales are compared in further detail.

Finally, in Chapter 7, a summary of main conclusions and potential future research in this area are recommended.

2 Overview

In this chapter, previous studies that have been carried out to investigate the mechanical properties of ice ridges and ice rubble are reviewed. In Section 2.1, the structural characteristics of an ice ridge feature are defined. The microscopic aspects of ice rubble are then discussed in Section 2.2, in particular, the formation and shear strength of freeze bonds. The macroscopic aspects of ice rubble and ridges are then reviewed, which have been further classified by scale, starting with laboratory tests (Section 2.3) and then *in-situ* field tests (Section 2.4). Finally, a summary of the results and the goal of this project is given in Section 2.5.

2.1 Ice ridge characteristics

Ice ridges are common features in Arctic and sub-Arctic regions. They form when the ice cover, forced by winds and currents, is compressed or sheared producing an accumulation of ice rubble (see Figure 2.1). Ice ridges are categorized into two types based on their primary formation process: pressure ridges and shear ridges. Pressure ridges form by compression of ice sheets (see Figure 2.1a), while shear ridges form in the boundary contact region when ice sheets deform in shearing, which usually occurs in fast ice or pack ice (see Figure 2.1b).

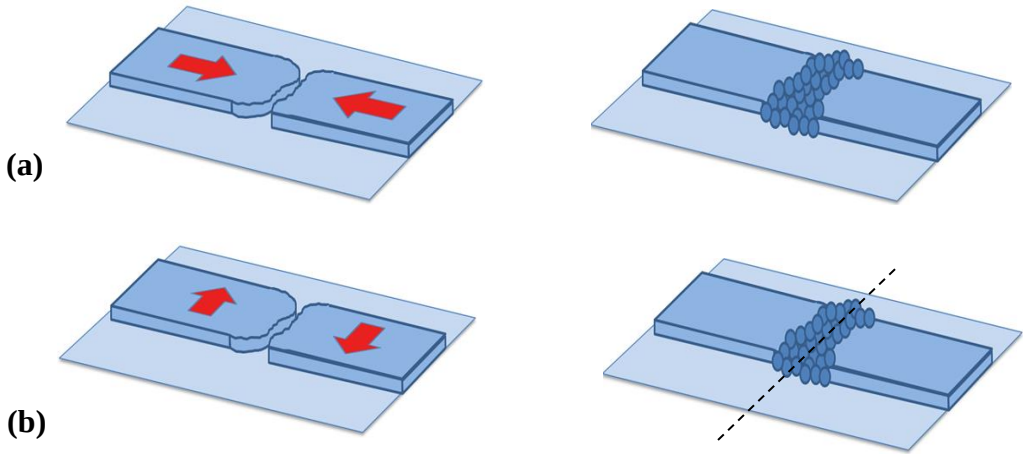

Figure 2.1. (a) Compressive (pressure) ice ridge formation. (b) Shear ice ridge formation.

Figure 2.2 shows a schematic of an ice ridge. Due to the inherent randomness of their nature, sea ice ridges come in a wide variety of shapes, sizes and structures. Numerous field studies have been undertaken in an attempt to better characterize the morphology of these features. Very good reviews of these have been written by Timco and Burden (1997), Sudom *et al.* (2011) and Strub-Klein and Sudom (2012). According to Timco *et al.* (2000), the ice broken in the ridge building processes creates rubble above and below the waterline. As the rubble is in hydrostatic equilibrium, the depth of the submerged part, known as the "keel" is approximately five times larger than that of the non-submerged part which is called the "sail". As shown in Figure 2.2, the sail is the non-submerged section of the ice ridge, in which the accumulated ice blocks were randomly positioned and combined with slush, air and snow. Also, the ice blocks in the sail may be partially frozen together or unconsolidated. The central portion of the ridge along the waterline is often refrozen and is referred to as the "consolidated layer" or "refrozen layer". As reported by Timco and Burden (1997), the consolidated layer is usually

thicker than the surrounding level ice. For instance, in a region with a water level about 1m in thickness the consolidated layer thickness may reach 2.5m.

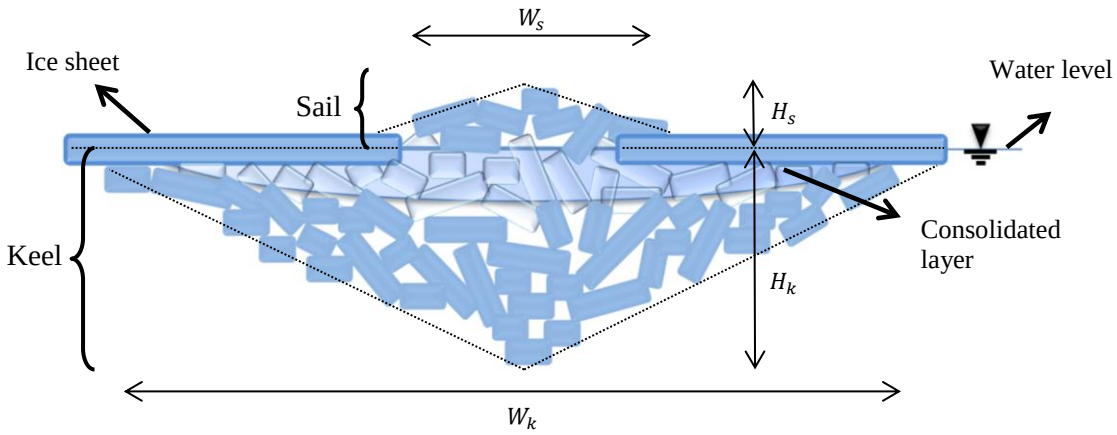

Figure 2.2. Schematic of a First-year sea ice.

The keel is the submerged and the largest part of the ice ridge. It may be consolidated at the top or not. The depth of the keel is much larger than the height of the sail. Most studies describe the keel and ice rubble strength as a function of cohesion and friction between ice blocks, which is known as Mohr-Coulomb material. Based on this approach, the ice rubble fails in shearing. Equation (2.1) defines the shear strength of the Mohr-Coulomb material,

$$\tau = \sigma_n \, tan \, \emptyset + c \tag{2.1}$$

In which τ is shear strength, $\emptyset$ is the angle of internal friction, c is cohesion and σ_n is normal stress.

As reported by Timco and Burden (1997), the depth of ice ridge keels may reach 16m at the West Coast of Newfoundland or even greater than 50m in the Arctic. They also found

that the ratios of keel and sail height and width (H_k/H_s and W_k/W_s) for 112 first-year ridges are 4.4 and 3.9, respectively. In this study, most of the focus is on the keel properties, since they are of interest for industry, as they pose a risk due to their potential interaction with subsea pipelines.

2.2 Freeze-bond tests

As soon as an ice ridge forms, ice blocks initiate to bond at their contact points to form freeze-bonds (FBs). In the sail, the degree of freeze-bonding is largely controlled by atmospheric and sintering processes. While in the keel, the freeze-bonding process is highly affected by cold reserves in the ice blocks at the initiation of the process. Once the ice blocks have warmed to the surrounding water temperature, the freeze bonding processes will be controlled by oceanic conditions. Sintering may also act to 'smooth out' the keel and increase FB area (Bailey et al., 2015).

Sintering is a phenomenon that describes the bonding formation between particles close to their melting point. It is usually known to be a slow process which can occur due to vapor diffusion, surface diffusion, surface flow, volume diffusion, plastic diffusion, plastic flow and grain boundary diffusion (Kingery, 1960; Kuriowa, 1962; Hobbs and Mason, 1964). The only processes that have been suggested to explain fast bond formation are the freezing of liquid layers at the contact region (Szabo and Schneebeli, 2007) and the freezing of water in a confined space (Dolan and Gupta, 2004). Liquid layer freezing was first suggested by Faraday (1859), when he observed that two contacted ice blocks bond together. This idea was later supported by employing advanced equipment techniques, such as ion and proton backscattering, x-ray scattering, low

electron diffusion, and atomic force microscopy, which showed that the liquid layer exists at -40℃ ice temperature.

The pressure melting process was also suggested by Thomson (1860) to address the origin of the liquid layer at the interfacial region. Pressure melting is a phenomenon in which ice pieces reach their melting point or may temporarily melt due to the application of external pressure. By removing the applied pressure, the ice pieces refreeze and bond together. However, this phenomenon fails to explain the sintering process of ice. As Bowden and Hughs (1939) later found, the pressure needed to melt ice is significantly higher than its mechanical strength (except at temperatures close to the melting point). The liquid layer's existence may also be due to collisional melting as shown by Dash and Wettlaufer (2003) and Dash *et al.* (2001). In this process, by impacting ice pieces, a significant amount of heat is produced due to the plastic deformation of ice. This large amount of heat results in temporary melting at the interfacial region. It has been argued that due to cooling process, the ice pieces begin to refreeze; however, it still has not been shown that the cooling process is fast enough to bond the ice pieces together (Szabo and Schneebeli, 2007).

Reduction of the surface energy is the driving force in sintering, which can be described by Young-Laplace equation ($\sigma = \frac{2\gamma}{r}$), in which γ is the surface energy and r is the curvature radius. Therefore, a smaller sphere-shaped piece of ice has higher surface energy, which results in a smoother surface. This is why ice with a rough surface gradually smooths over time.

Investigating the physical aspects of the sintering phenomenon is important for understanding ridge properties, as rubble in the keel is usually close to its melting point; an insightful review of this has been written by Blackford (2007). However, further investigating the physical aspects of the sintering process is outside the scope of the presented research. Therefore, in the presented research, only some mechanical properties of freeze bonding have been reviewed, as they have been shown to influence the mechanical properties of ice rubble and have been linked to the observed peak load before failure (Ettema & Urroz, 1989; Liferov and Bonnemaire, 2005).

Many tests have been carried out to investigate the effective parameters that influence FB formation and its failure processes (Ettema and Schaefer, 1986; Shafrova and Høyland, 2008; Repetto-Llamazares *et al.*, 2011; and Møllegard, 2012; Boroojerdi *et al.*, 2016). Ettema and Schaefer (1986) tested the shear strength of freshwater FB under a range of environmental conditions (air, distilled, tap and saline water), contact periods (0-4 minutes), confining pressures (0-4kPa), loading rates (0.44mm/s and 0.84mm/s) and contact areas ($4.52 \times 10^{-3} m^2, 9.03 \times 10^{-3} m^2$, and $19.35 \times 10^{-3} m^2$) which have a relative area ratio of 1:2:4. Air and water temperatures were approximately 0℃ and the ice blocks' initial temperature was -10℃. The test setup involved a tank which had an ice base surface with measuring in $0.71m \times 0.28m \times 0.05m$ in length, width and thickness, respectively. After placing an ice block on an ice base surface in a water filled tank, they were confined by a load for a specified amount of time. Afterwards, the top block was pulled by a cable. By measuring the load and failure area, they assessed the shear strength of the FB.

Ettema and Schaefer (1986) observed that the shear strength for ice blocks submerged in distilled water and tap water increases by increasing the contact time. In contrast, no significant changes were observed for ice blocks submerged in saline water or in air. However, the authors noted a stronger FB in air compared to saline water, and that by increasing the salinity of the solution, the shear strength decreases. They then discussed that shear strength increases at higher pressure confinement. This increase is lower for distilled water and air. Their analysis indicated that the contact areas have no significant effect on the shear strength.

Further FB tests were conducted by Shafrova and Høyland (2008) in both the field and laboratory tests at The University Center in Svalbard (UNIS). They measured the shear strength of individual submerged sea ice blocks and the FB between two sea ice blocks under uniaxial compression, which fail along the contact area. Shafrova and Høyland (2008) investigated the effects of various parameters on the strength of both FB and individual submerged ice block, such as submersion time, confining pressure, ice block dimensions, their initial temperature, salinity and density. For this, they carried out the test by submerging six ice blocks in an opening in landfast ice. After preparing the cubic ice blocks ($0.24m$ in length), they cut them in half diagonally, mounted them back together in a frame and submerged them in water. After a specified time length, the ice blocks were removed from the water and compressed in a uniaxial compression machine to measure the strength of FB. They also did some tests in the laboratory, in which the ice blocks were kept confined through the test period.

Shafrova and Høyland (2008) found that the strength of FB is affected by its physical properties. For examole, by increasing initial ice temperature, salinity and density the FB strength decreases. The results showed that the FB strength in freshwater ice is about 5-10 times higher than in saline ice. The authors also concluded that by increasing the submersion time, the strength of both FB and submerged ice block decreases. In fact, they observed during the field tests that FB strength decreases by increasing the submersion time from 24 hours to 48 hours where the initial ice temperature varied between -2℃ and -7℃. Similar behavior was observed for laboratory tests with an initial temperature of -10℃. However, no changes were observed for initial ice temperature of -5℃.

Shafrova and Høyland (2008) suggested additional tests to find a more accurate relationship between the initial ice temperature, submersion time and FB strength. They proposed a bell-shaped curve for the uniaxial strength of FB, which reaches a maximum rapidly and gradually decreases. They also investigated the effects of ice block dimensions on the FB strength. They found that at bigger ice block contact, the FB strength increases, which they attributed to the higher negative heat resource to create FBs between the blocks.

Shafrova and Høyland (2008) carried out a number of tests to investigate the variation of ice blocks strength by increasing submersion time, as they believed the strength of individual ice blocks may contribute to the overall strength of ice rubble and ridge. Analysis of their results showed that for 24 hours and 48 hours submersion, the sea ice compressive strength reaches about 1*MPa*. Bailey *et al.* (2015) found similar values for

24 hours. However, for low consolidation time the compressive strength reached about 6*MPa*. Timco and Frederking (1990) also argued that the ice block compressive strength is highly affected by the type of ice and the load direction.

Repetto-Llamazares *et al.* (2011) and Møllegard (2012) carried out FB tests for saline ice in saline water and found that the data matched the bell-shaped curve suggested by Shafrova and Høyland (2008). They suggested that the first phase is dominated by freezing. As shown in Figure 2.3, in this phase, FB temperature and consequently the porosity reach their minimum values causing the FB strength to reach its maximum value at t^*. The second phase is dominated by heating, as the FB equilibrates to the surrounding water temperature at t_{eq}. The authors propose that this acts to increase the porosity of the bond and hence reduces its strength. The third phase starts when the FB temperature is equal to the surrounding ambient and ice temperature. The authors suggested that the initial temperature, sample size, as well as thermal properties, govern the width and height of the bell-shaped curve.

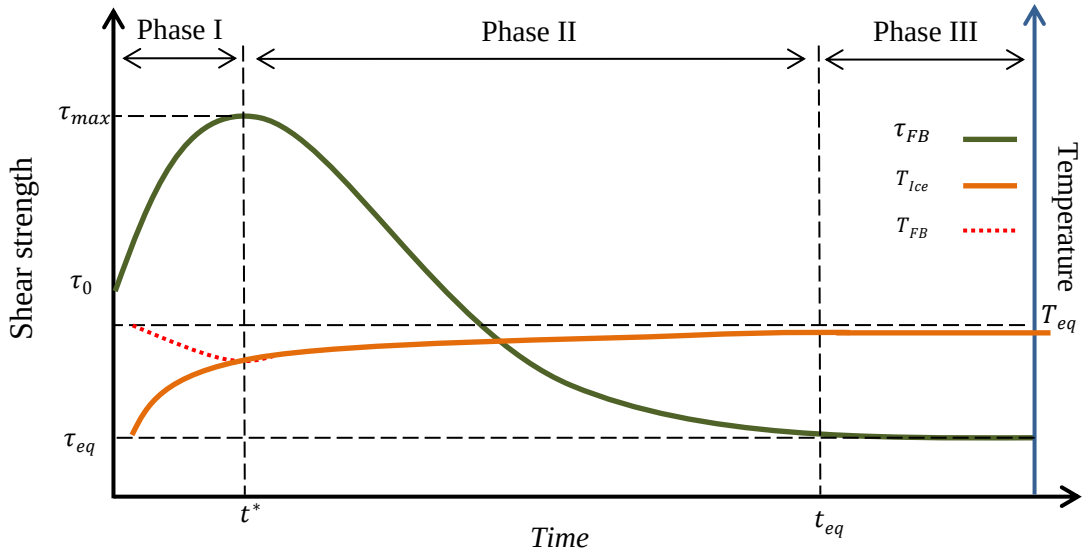

Figure 2.3. A schematic of shear strength and temperature vs. submersion time for in freeze-bonding for ice with an initial temperature lower than freezing temperature.

Boroojerdi *et al.* (2016) used the Asymmetric Four Point Bending (AFPB) method to investigate the effects of contact period time (1 minute to 26 hours), initial ice block temperature (0℃ to -18℃), confining pressure (10kPa to 100kPa) and deformation rate (5mm/s to 20mm/s) on the strength of FB in the contact area of two cylindrical fresh-water ice blocks. Similar to the results of Repetto-Llamazares *et al.* (2011), Boroojerdi *et al.* (2016) found that the FB shear strength versus time follows a bell-shaped curve for saline ice suggesting that this dependency is driven by thermal processes rather than brine drainage mechanisms. The results showed that the peak value (τ_{max}) and the equilibrium time of the bell-shaped curve (t_{eq}) are functions of initial temperature and confinement. Boroojerdi *et al.* (2016) found that in the tests with -18℃ initial ice temperature the peak shear strength reached 250kPa (τ_{max}) after 5 minutes

submersion (t^*), and after 3 hours reached phase III (t_{eq}). In the tests with initial ice temperature equal to -10℃, the values of τ_{max}, t^* and t_{eq} were reported 180kPa, 3-5 minutes, and 1 hour, respectively. Moreover, Boroojerdi *et al.* (2016) argued that the FB strength is highly affected by the confinement, as by increasing the confinement from 10kPa to 100kPa for 30 minutes submersion, the FB strength linearly increased from 70kPa to 250kPa.

2.3 Laboratory ice rubble tests

Investigating the effects of various parameters on FB strength is crucial for estimating the strength and failure behavior of ice rubble and ridges. However, it is believed that the blocks' geometry, positioning and dimensions are parameters that influence the strength of ice rubble and ridges. Many laboratory and *in-situ* tests have been conducted to investigate theses parameters. Laboratory tests have the advantage that test conditions can be controlled and monitored closely; however, it is difficult to scale the properties of ice rubble. In this section, previous laboratory tests on ice rubble are reviewed.

2.3.1 Direct Shear box tests

Initial tests began with the design, construction, and application of a direct shear box in order to measure ice rubble properties (Keinone and Nyman, 1978; Prodanovic, 1979; Weiss *et al.*, 1981; Hellmann, 1984; Fransson and Sandkvist, 1985; and Serré *et al.*, 2011). Figure 2.4 illustrates a schematic of a direct shear test setup sectioned into two large parts. Ice rubble is pushed by a normal load on top of the box, resulting in shear forces at the sides and shear failure plane to occur.

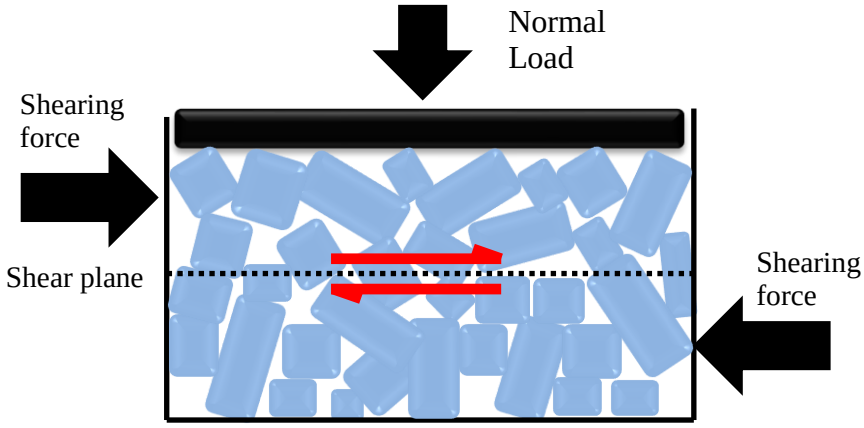

Figure 2.4. Schematic illustrating the direct shear box technique.

Weiss *et al.* (1981) conducted direct shear box tests on saline ice rubble. The designed box was 1*m* in height and it was able to move 0.28*m* horizontally. After each test, they settled back the confining plate and moveable box to its pre-test position, and after stirring the rubble they conducted another test. The applied normal pressure in this study varied between 0*kPa* and 28*kPa*. However, Weiss *et al.* (1981) observed a cohesive behaviour in ice rubble, and found that the shear strength decreases by increasing speed and it increases by increasing pressure confinement. Similar behaviour was reported by Hellman (1984) for freshwater ice. In his experiments, he argued that the observed failure behaviour could be divided into three different phases. In the first phase (2*mm* displacement), which they called primary shear mode, a significant increase in shear strength was observed while there was little to no change in normal force, which they attributed to a packing of the ice particles. In the second phase (50*mm* to 150*mm*), which they called secondary shear mode, the peak force was reached and an increase in the normal force was measured which they attributed to dilation of ice fragments. In the third phase, which they called tertiary shear mode, the shear strength remained constant,

although the normal load still increased. The author addressed that to the continuous residual friction force that exists after the initial failure. Hellman suggested that in the first two phases the rubble behaviour was dominated by cohesion and in the third no FBs remained.

Ettema and Urroz (1989, 1991) reviewed the generated data for the direct shear box tests and reported that friction angle ($\emptyset$) and cohesion (c) values are ranged between 11° and 65°, and $0kPa$ and $4kPa$, respectively. Timco and Cornett (1999) argued that the wide range of values may be due to the characteristics of the shear box setup, which induces non-uniform deformation and stress distribution in ice rubble and forces the sample to fail along an induced failure plane (but not necessarily the weakest one).

Figure 2.5 illustrates the values of the internal friction angle and cohesion versus the maximum value of confining pressure reported from prior studies. Referring to the figure, a wide range of values for the internal friction angle ($\emptyset$) was reported. It also shows that the values of cohesion increase by increasing confinement. It is noteworthy that the values of cohesion and the angle of friction for ice rubble are much larger than those for particles such as sands and gravel (Ettema and Urroz, 1989). This may be a result of ice rubble freeze bonding, locking and crushing, which are associated with values of several orders of magnitude larger than those for particles comprising soils.

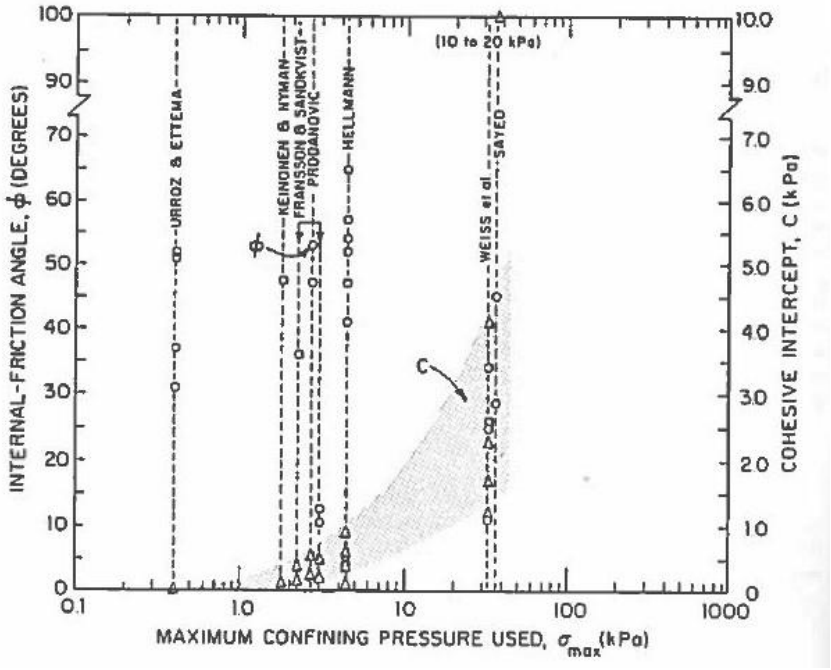

Figure 2.5. Reported values of internal friction angle ∅ and cohesive c vs. maximum pressure confinement σ_{max} (Ettema and Urroz, 1989).

Referring to Figure 2.5, Ettema and Urroz (1991) argued that low confined ice rubble behaves more like a cohesionless material as they have lower cohesive (c) value, while by increasing confining pressure (σ_{max}) the ice rubble behaves more like a cohesive material as cohesion increases consequently. Therefore, the authors argued that cohesion is a function of confinement (2.2).

$$c_i = f(\sigma_i) \tag{2.2}$$

In which c_i is cohesion and σ_i is confinement.

Therefore, the authors suggested by combining Equation (2.2) and Equation (2.1) the following equation for unconsolidated ice rubble is obtained;

$$\tau_i = \sigma_i \, tan \, \emptyset_i + f(\sigma_i) \tag{2.3}$$

By assuming that there is a linear relationship between cohesion (c_i) and confinement (σ_i) (i.e. $c_i = \beta \sigma_i$), Equation (2.3) can be modified to,

$$\tau_i = \sigma_i(\tan \emptyset_i + \beta) = \sigma_i \tan \emptyset' \tag{2.4}$$

In which, Ettema and Urroz (1989) argued that $\emptyset'$ refers to the effective angle of internal friction.

The authors also suggested that the degree of packing of either cohesive and cohesionless ice rubble, affects its shear stress behavior (see Figure 2.6). In fact, for densely packed ice rubble, the peak strength is initially observed to gradually decrease to reach a constant value, which is known as continuous shear strength. For loosely packed rubble, the ice pieces initially pack together and reach a continuous shear strength with increasing load/time. Therefore, it is important to define the cohesion and internal angle of friction for both the peak strength and continuous shear phases. Additionally, Ettema and Urroz (1989) argued the values of both peak strength and continuous shear strength are highly affected by rubble porosity and confining pressure.

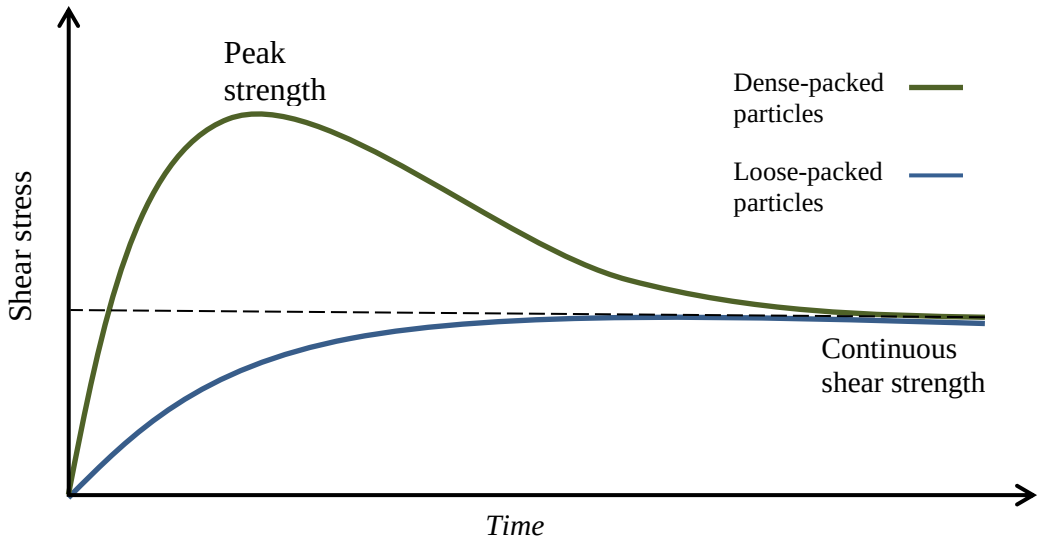

Figure 2.6. Shear stress vs. time for dense-packed particles and loose-packed particles (after Ettema and Urroz, 1989).

2.3.2 Shear box tests

The simple-shear box test was a new method suggested by Urroz and Ettema (1987) to measure the shear strength of vertically unconstrained floating freshwater ice rubble. The setup was installed in an ice tank measuring 6*m* by 0.91*m* and 0.61*m* in length, width and depth, respectively. As shown in Figure 2.7, one sidewall of the box was fixed to the tank wall, while at the opposite side a moving sidewall was pushed through the rubble mass by a vertical ram. A minimum gap of 0.53*m* was left between the moving and fixed sidewall, where the maximum end-wall rotation was 45°. In this case, they measured the applied shear force to the sidewalls by a dynamometer which linked the vertical arm to the carriage.

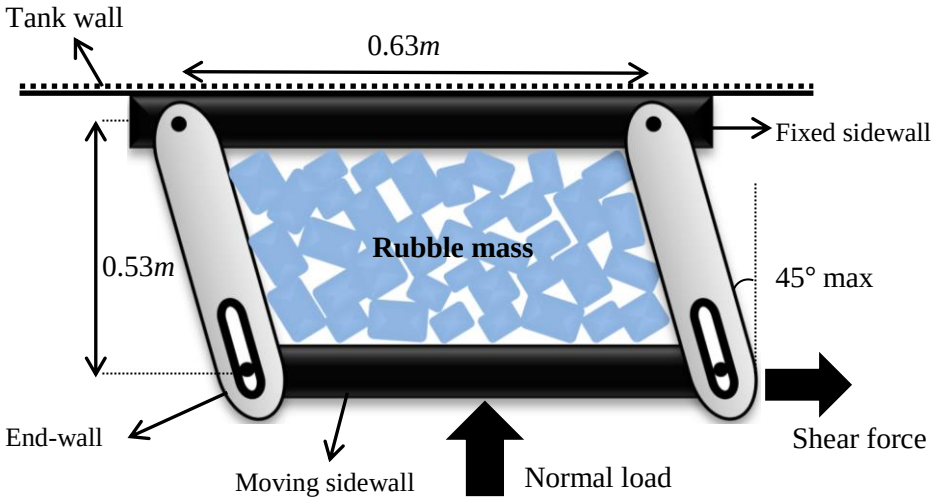

Figure 2.7. Plane view of the experimental shear box (after Urroz and Ettema, 1987).

Urroz and Ettema (1987) found that the shear strength of rubble is affected by its thickness, layer porosity and shear deformation rate. The results of low shear rates showed a distinct ice rubble failure, where both normal load and shear force significantly dropped. In this case, they observed a periodic failure behavior after the first failure, both forces again reached a second peak with the same order of magnitude and again rapidly dropped, which represents the second failure. Therefore, the third mode of shear failure did not occur at low shear rates as was observed by Hellman (1984). Urroz and Ettema (1987) found that by increasing the shear rate, the shear strength decreases. However, in contrast to low shear rates, at the higher shear rates the failure points were not obvious, since both the shear and normal forces did not significantly drop after the failure, which represents the third mode of shear failure as observed by Hellman (1984). In general, they could not identify a primary shear failure mode as defined by Hellman (1984). Urroz and Ettema (1987) addressed this discrepancy to the different test setup, as the rubble mass was dilated vertically and not confined in that direction. They also observed that ice

rubble in higher shear rates behaves like a cohesionless material, which they attributed to less FB development in this condition.

2.3.3 Bi-axial test

The bi-axial compression chamber setup was developed by Timco *et al.* (1992) at the Canadian Hydraulic Centre (CHC). As shown in Figure 2.8, in the bi-axial compression chamber, two walls were fixed while the other two were free to move, generating $50kN$ of load capacity. When fully expanded, the box dimensions were $1m \times 1m$ horizontally and $0.5m$ height. A confining load could be applied to the top of the box to resist sample deformation in vertical direction.

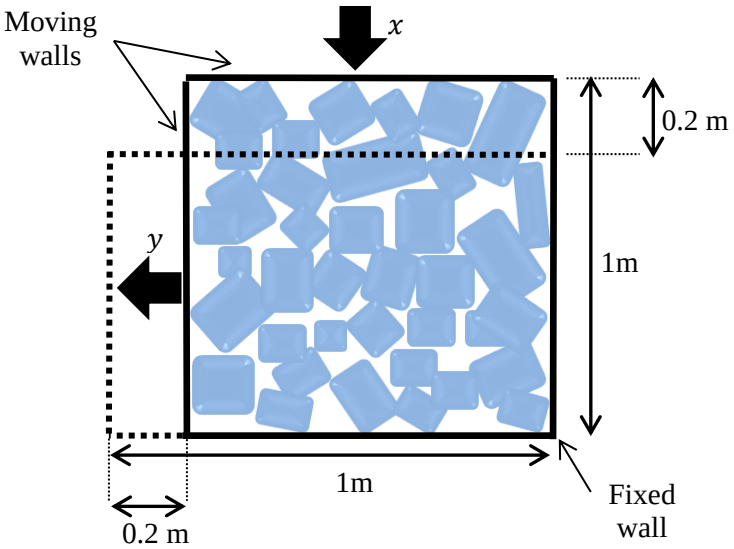

Figure 2.8. Schematic illustrating the bi-axial compression setup, where the solid and dash lines represent the shape of the walls before and after a test (after Sayed *et al.*, 1992).

Although the bi-axial test resembles the direct shear box test, it has the advantage to apply a uniform stress and strain and the rubble is not forced to fail on a pre-defined

failure plane. Also, in this method the mechanical properties of ice rubble can be investigated in both plane-stress and plane-strain configurations.

A number of bi-axial tests were conducted by Sayed *et al.* (1992), Løset and Sayed (1993) and Cornett and Timco (1995, 1996) to investigate the strength of both dry and submerged ice rubble under continuous shear, as they assumed the ice rubble has a cohesionless nature. For this they used the following equation to estimate the mobilized angle of internal friction,

$$\emptyset_m = sin^{-1}(\frac{\tau}{p}) = sin^{-1}(\frac{\sigma_1 - \sigma_3}{\sigma_1 + \sigma_3}) \quad (2.5)$$

in which, τ is the shear stress, p is the mean pressure, and $\sigma_1$and σ_3 are major and minor principal stresses (σ_x and σ_y), respectively.

Initial bi-axial tests were carried out by Sayed *et al.* (1992) in order to investigate the stress-strain behavior of model ice rubble. In this study, they used EGADS model ice in which the maximum ice sample length was around 0.2-0.25m and thickness about 30mm to 40mm. They tested both dry and submerged ice samples for constant displacement rates under a range of confinements. For this, the sample size was $1m \times 0.8m \times 0.5m$ in X, Y and Z directions, respectively, where the X and Y directions were contracted and extended and the sample dimension in Z direction was constant during the test. Analysis of their results revealed that there was a direct relationship between stress and strain in which the ice rubble porosity did not affect the relation. They also found that

the EGADS ice rubble[1] deformed plastically since the deformation was not recoverable. As a result, they argued that modeling ice rubble as an elastic-plastic or a rigid-plastic material is not appropriate.

Sayed *et al.* (1992) found an inverse relation between the strain ratio ($\left|\frac{\varepsilon_y}{\varepsilon_x}\right|$) and mobilized angle of internal friction ($\emptyset_m$), as their results revealed that for dry and submerged ice the mobilized angle of internal friction varies between 32°- 58° and 15°- 47°, respectively. Although Sayed *et al.* (1992) found that stress-strain for both dry and submerged ice samples had similar trends, a higher scatter was observed in the mean pressure-ice concentration plots for dry ice rubble tests.

Similar tests were conducted by Løset and Sayed (1993) at the Hydraulics Laboratory of the National Research Council Canada, where they used an identical setup to that which was employed by Sayed *et al*. (1992). In this study, they investigated the effects of different freshwater ice blocks dimensions on the stress-strain relationships. For this, they examined the freshwater ice rubble with uniform ice blocks' dimensions; small ice blocks (25*mm* in length) and large ice blocks (100*mm* × 100*mm* × 130*mm*). They also conducted tests on freshwater ice rubble with a mixture of half small blocks and half large blocks.

Similar to the results analyzed by Sayed *et al.* (1992), Løset and Sayed (1993) found a direct relation between stress and strain, in which the sample deformed plastically. Their

[1] EG/AD/S stands for: Ethylene glycol (EG), aliphatic detergent (AD) and sugar (S), A new type of model ice for refrigerated towing tanks that was suggested by Timco (1986)

results showed that the mobilized angle of friction for freshwater ice rubble varied between 44° and 58°. They found that the mixed ice rubble sample produces lower stress than the uniform distribution ice rubble samples (both small and large). The authors also found that the produced stress is higher in freshwater ice rubble in comparison to the model ice rubble conducted by Sayed *et al.* (1992).

Further tests were conducted by Cornett and Timco (1995, 1996) to investigate the mechanical properties of both dry and submerged saline ice in bi-axial tests. They found that the submerged rubble is lower in both the initial yield strength and the strength under the deformation and reduced the mobilized angle of internal friction by about 30%. Moreover, the results showed that curing under pre-stress can significantly increase the initial yield strength of the ice rubble likely because of bonding, but has little influence on the mobilized friction angle after the yield.

2.3.4 Indentation tests

Indentation tests were conducted by Bruneau (1996) at C-CORE's Cold Room facility to model first-year ice ridge interaction with offshore structures on a laboratory scale. For this, an indenter was pushed through stationary ice rubble, which was prepared in a steel tank measuring 1m by 1m and 0.76m in length, width and height, respectively (see Figure 2.9). To observe the ice rubble-indenter interaction, two Plexiglas walls ($0.6m^2$) were installed at the side and rear of the tank. Roughly cylindrical freshwater ice (concave at the end) measuring 25mm and 30mm in diameter and length, respectively, were used to model the first-year ice ridge on a small scale. A 100mm gap was prepared

between the ice rubble and the end wall. Also, four support frames were mounted to keep the ice rubble fixed during the test; therefore, there was no contact between the ice rubble and the wall during the test. Two 1.1kN cantilever load cells were used for load measurement, and a displacement transducer was attached to the top of the drive mechanism to measure the indenter displacement during interaction. The ice temperature ranged between -24℃ and 0℃, and the Cold Room temperature was set to 0℃. The penetration rate of the indenter was set to 6*mm/s*.

The depth and width of the ice rubble were chosen between 100*mm*-250*mm* and 300*mm*-450*mm*, respectively. Therefore, the overall dimensions of ridge keels and ratios were geometrically scaled approximately at 1 to 100; however, the particle and dynamic modeling were not scaled. Analysis of the results showed for the ice rubble that consolidated in approximately 10 minutes, the maximum applied force due to rubble-indenter interaction ranged between 30*N* to 60*N*, while the maximum force for the ice rubble that took 1140N minutes to consolidate reached 167*N*, which indicates the effects of consolidation on the strength of ice rubble and ridges.

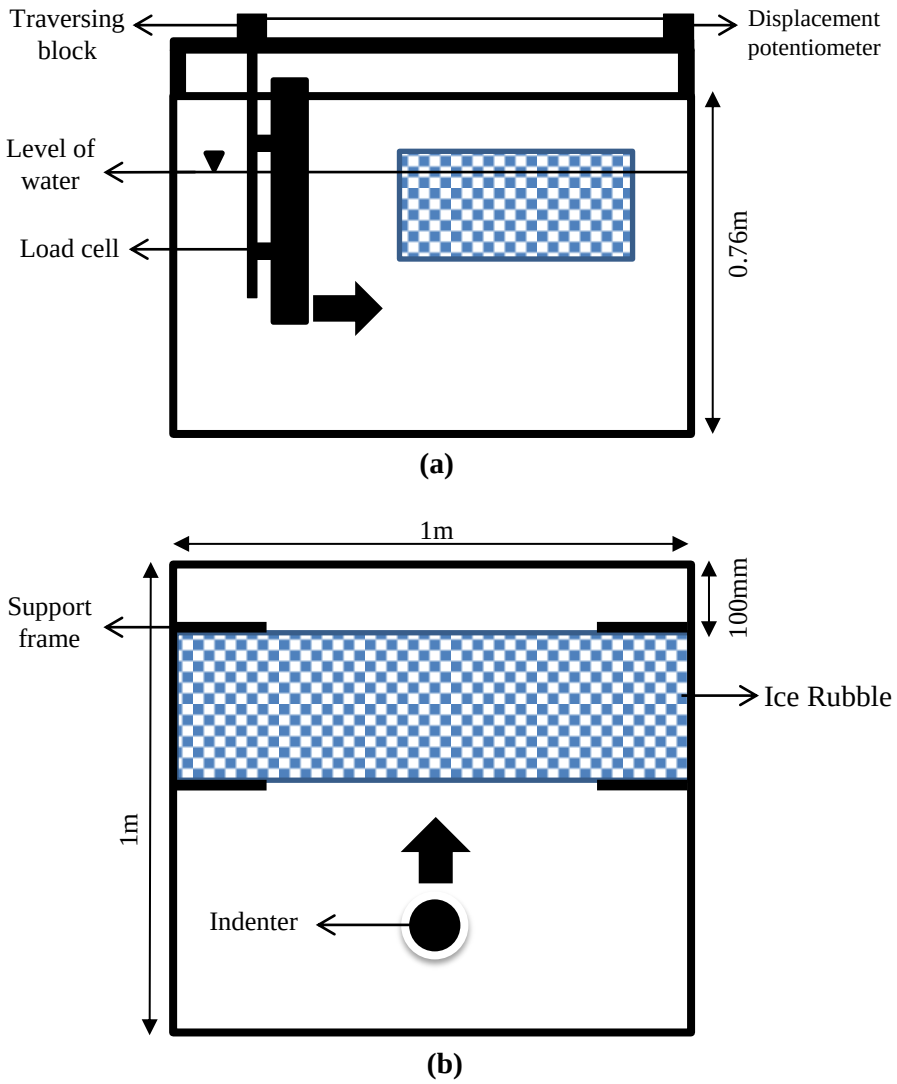

Figure 2.9. Schematic illustrating the indentation test setup (after Bruneau, 1996), (a) side view, (b) plane view

Bruneau (1996) found that the geometry of plug and local passive failure surfaces are random; however, he generally observed that the plug failure was preceded by some local failure. Bruneau (1996) also argued that the shear resistance and structural strength of ice rubble at the laboratory scale are highly influenced by the ice temperature, normal stress, consolidation time (residence time), and the geometry of the ice blocks. Bruneau (1996) found that resistance to indentation of floating laboratory ice rubble accumulations

increased non-linearly with rubble depth, and decreased with rubble width as well as higher ice temperature (at the time of placement).

2.3.5 Laboratory Punch Test

Azarnejad and Brown (1998, 2001) carried out punch tests in the laboratory at the University of Calgary. They investigated the influence of indenter speed (10-115mm/s), consolidation time (0-3 hours) and ice rubble beam thickness (0.2-0.5m) on the strength and failure behavior of an ice rubble beam. Figure 2.10 shows the punch box test setup designed for this study, in which a rectangular tank was fabricated, measuring $2.45m \times 0.5m \times 0.9m$ in length, width and height, respectively. The walls were constructed of Perspex, and the middle part of the tank was kept clear to observe the failure mode. The load was applied by a hydraulic ram attached to a rectangular aluminium platen that spanned the entire width of the box (minus a gap for tolerance) and was $0.25m$ in width. This therefore resolved the experiment from 3D to a 2D plane-strain allowing observation of failure planes. Freshwater ice rubble with dimensions $20mm \times 15mm \times 7.5mm$ was prepared by ice machines. The room temperature was kept at a nominal temperature of -3℃. However, no initial temperature of the ice blocks was reported by the authors. In order to avoid displacements in the non-loaded portion of the rubble, small pieces of Perspex were glued to the walls to artificially increase the friction of the tank walls (see Figure 2.10). During the tests, the applied force and displacement were measured by using a load cell and a string potentiometer and failure modes were observed by video camera.

For tests conducted with greater consolidation times (2 hours or more), a consolidated layer started to form at the top surface of the ice rubble beam. The consolidated layer was cut through by saw before the tests, as would be the case for a traditional punch test in the field (see Section 2.4.2). The majority of the 0 hours consolidation tests were generally carried out directly after conducting a higher consolidation test with the same ice rubble beam. In order to break the consolidated layer and possible residual FBs, the ice rubble was stirred before the 0 hours tests. This method therefore likely ensured that no negative sensible heat reserves remained in the ice rubble; however, ice block dimensions may not have been consistent.

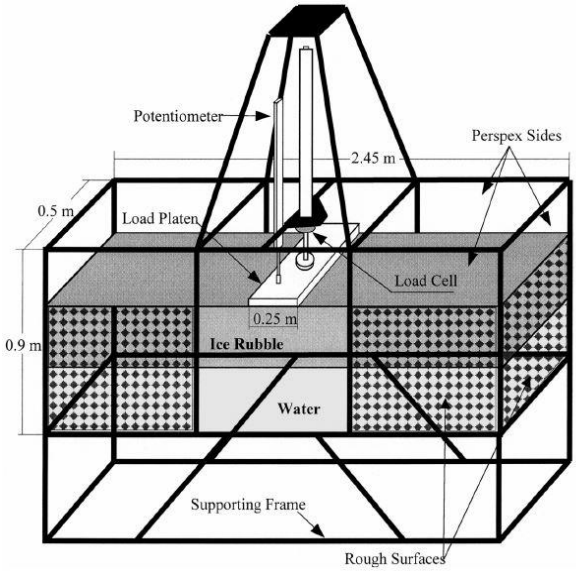

Figure 2.10. Punch test setup designed by Azarnejad and Brown (2001).

Azarnejad and Brown (1998, 2001) found that the deformation rate has the most significant effect on the strength and failure mode of ice rubble. At slow loading rates (< 40*mm/s*), a rectangular or trapezoidal plug of undisturbed ice rubble that spanned the

entire thickness was pushed down by the platen and failure occurred mainly at the edges of the plug, while the surrounding rubble remained undisturbed. In comparison, at high deformation rates (> 40*mm/s*) the failure occurred over a larger area, both under the platen and in the surrounding ice rubble. In most cases, a triangular or wedge shape was formed and did not span the entire thickness of the rubble beam (see Figure 2.11).

Figure 2.11 shows a schematic of a typical load-displacement curve (Figure 2.11a) and associated failure mode (Figure 2.11b) at both slow and fast loading rates. The load traces show that in both tests a peak load associated with FB failure was evident, followed by residual frictional force. At slow loading rates, the peak load was 1.2-2 times lower than in the fast tests and occurred at a smaller platen displacement. Also, referring to the figure, due to a progressive failure in the fast tests, the rate of the load reduction after the peak failure is lower than that in slow tests and reached a lower residual load. Azarnejad and Brown (2001) referred that to the existence of frictional shear resistance force in the fast tests, as they maintained further during the punch test due to progressive failure in the fast tests. They also observed that by increasing the thickness, the peak loads occurs earlier.

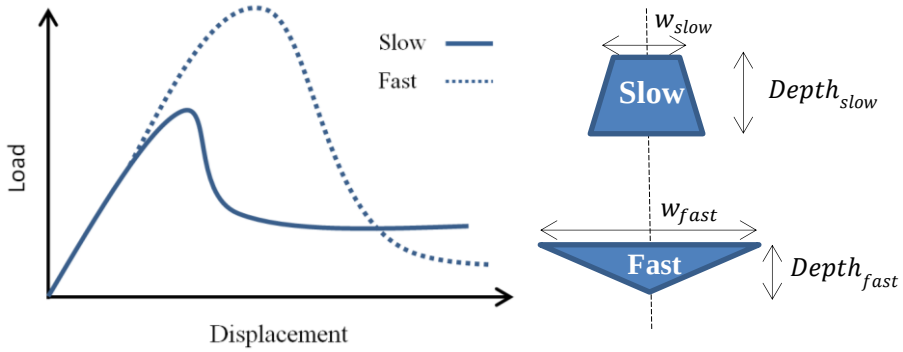

Figure 2.11. (a) Schematic of load vs. displacement for constant beam thickness and consolidation time. (b) Schematic of the failure mode for constant beam thickness.

Azarnejad and Brown (2001) suggested that the observed difference in failure mode with loading rate could be caused by hydrodynamic effects. As a result, they conducted additional tests to investigate the effects of inertia using just the platen in open water and with an ice block of similar porosity as the rubble of dimensions $22cm \times 28cm \times 45mm$. Results showed that at low loading rates, the inertial component was negligible; however, at high loading rates it could be sufficient to effect failure modes. They argued that at higher loading rates, the water inside the voids does not have time to escape, thus influencing failure mechanisms and the loading patterns. In addition, they also suggested that the shear strength of FB could be rate dependent. They introduced Equation (2.6) to estimate the shear strength

$$\tau = \frac{F_{peak} - F_R - F_I}{2WH} \tag{2.6}$$

Where τ is shear strength, F_{peak} is the peak load, F_R is residual force, F_I is inertial force, and W and H are the width and thickness of the ice beam, respectively, in which the

former is assumed to be equal to the platen width. Therefore, the defined shear strength is the nominal shear strength, as the failure area for all tests is assumed constant. This results in the shear strength being only the function of the punch load.

Azarnejad and Brown (2001) observed that the shear strength increased by increasing the ice rubble beam thickness and consolidation time. They estimated that for $0.2m$ ice rubble thickness and $15mm/s$ displacement speed, the shear strength was about $0.05kPa$ and $0.1kPa$ for 0 hours and 1 hours consolidation time, respectively. For the thicker ice rubble beam ($0.5m$ thickness) and a similar ram speed, the shear strength reached about $0.1kPa$ and $0.4kPa$ for 0 hours and 1 hours consolidation time, respectively. Moreover, by increasing the hydraulic ram speed to about $115mm/s$, the shear strength range was $0.15kPa$ and $0.25kPa$ for $0.2m$ thickness, and $0.3kPa$ and $0.5kPa$ for $0.5m$ thickness, for 0 hours and 1 hours consolidation time, respectively.

Azarnejad and Brown (2001) observed that by increasing the consolidation time from 0 hours to 1 hours, not only does the peak load increase, but the beam fails at a lower displacement, which indicates that the ice rubble beam is more heavily bonded at higher consolidation times. In general, they argued that the ice rubble beam failure at lower displacement represents a FB failure, while in higher displacement it is due to friction failure, which was more common in low consolidation time (0 hours).

Additional tests were conducted by Lemee and Brown (2002) using the same equipment and methodology to investigate the effects of ice block dimensions (small, medium, big and graded), initial ice temperature (-1℃ and -30℃) and deformation rates (9-105mm/s).

The main difference composed to the test setups of Azarnejad and Brown (2001) was the cold room temperature, which was set to -1℃ in this study compared with -3℃ used in their work. In Table 2.1, the ice block dimensions and porosity of the rubble beam are given for the work of Lemee and Brown (2002). Referring to the table, no consistant relation was found between the porosity and the dimensions of the employed ice blocks. The porosity of the graded Arctic ice was much lower, which is expected, as the smaller blocks would fall into the voids of the larger blocks. Results showed that in the big block tests, the failure area was greater than the size of the platen width, even at low loading rates. This was because the ice blocks which were partially loaded effectively increased the platen width. Increasing the ice block dimensions also caused the ice beam to fail at greater displacements. Lemee and Brown (2002) argued that this may be due to a failure processes as in larger blocks a higher beam deformation is required to mobilize the friction between the blocks. In addition, they found that in 0 hours consolidation tests the block size does not significantly affect the ice beam strength. However, by increasing the consolidation time, the ice beam consisted of smaller blocks that had a higher strength, for which it may be concluded that in an ice beam consisting of smaller blocks the consolidation may increase due to a greater number of block-block contacts.

Similar to small scale FB tests described by Boroojerdi *et al.* (2016), Lemee and Brown (2002) observed that by decreasing initial temperature from -1℃ to -30℃, the ice beam has much stronger bonds between blocks, where the friction angle increases about 10°. They also observed a similar behavior as Azarnejad and Brown (2001) for both slow and fast tests.

Table 2.1. Dimensions and ice rubble porosity based on ice rubble type (after Lemee and Brown, 2002).

Rubble Type	**Dimensions (*mm*)**	**Porosity**
Small blocks	20×15×7.5	0.5
Medium blocks	35×35×15	0.648
Graded	20.5	0.386
Big blocks	100×150×25	0.526

Further laboratory punch tests were carried out by Jensen *et al.* (2000) in the large ice tank at the Hamburg Ship Model Basin (HSVA). In this study, they scaled the physical and mechanical properties of ice ridges to some extent, as they argued that scaling the temperature is not possible since unconsolidated ice rubble is naturally at the freezing point.

In order to scale the physical and mechanical properties of ice ridges, after the preparation of ice rubble the freezing continued until level ice thickness was reached at 48*mm*. The level ice thickness increased during the consolidation period by approximately 10*mm*, while the thickness of the ice rubble was found between 10*cm* to 15*cm* (about 2-3 times larger than level ice thickness).

Jensen *et al.* (2000) used three different loading platen geometries: a large circular platen of 0.7*m* diameter, a small circular platen of 0.2*m* diameter and a rectangular platen of 1.5*m* long and 0.5*m* wide (2D test). For this, the platen was pushed through the beam until it was observed that the ice beam failed. The platen was then lifted up and reloaded again until the total failure occurred. Jensen *et al.* (2000) suggests a cohesion of

$c < 500Pa$ and an angle of internal friction of $25° < \emptyset < 40°$. They suggested that assuming a scale factor of 25 would give a full-scale cohesion of $c < 12kPa$.

Liferov *et al.* (2002) simulated the punch tests conducted by Azarnejad and Brown (2001) and Jensen *et al.* (2000) using a 3D Finite Element Method (FEA) model, which assumed the ice rubble was as an elastic-plastic material. Their simulations showed that the initial loading caused bending of the ice sheet and that the rubble failed in tension at the bottom of the beam. Also they found that the strength of the interface between the rubble and the out-of-plane tank walls had no significant influence on the ultimate load. Increasing cohesion and friction angle of the rubble caused the angle of the failure planes and the deformed plug area to increase. This increase was much more sensitive to the friction angle than the cohesive term.

Liferov and Bonnemaire (2005) compared the force-displacement curves for both *in-situ* and laboratory punch tests. As shown in Figure 2.12, they found that *in-situ* tests may have one or two peak loads in which the first peak is higher than the second one. However, only one peak load was observed in laboratory tests. The maximum load that was measured at *in-situ* tests was between $0.5MN$ and $1.5MN$, whereas, this value was less than $1kN$ in laboratory tests. Liferov and Bonnemaire (2005) argued that the first peak load in the *in-situ* tests was due to breakage of the rubble matrix (FB failing at the block-block level), after which the behaviour of the broken rubble is dominated by interlocking, friction forces between blocks and dynamic freeze bonding. In the laboratory punch tests, no distinct peak was observed and failure occurred at a higher

beam deflection. They also suggested that the delayed failure in the laboratory tests was caused by the beam initially bending before punching through. Further, the absence of a distinct peak load suggested thermodynamic scaling of the rubble was not appropriate, causing insufficient bonding between the ice blocks.

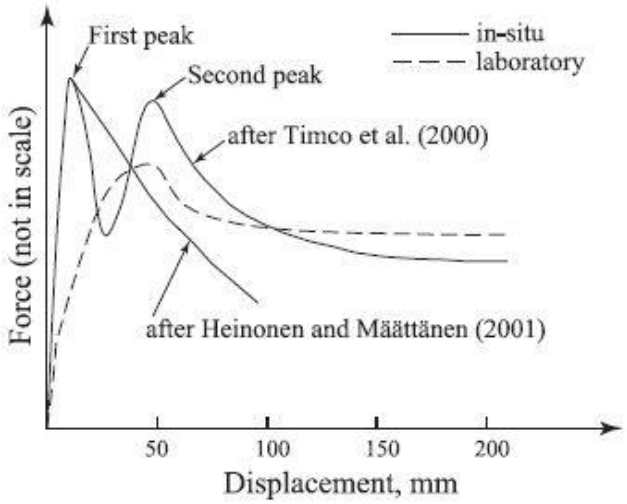

Figure 2.12. Typical force-displacement diagrams for *in-situ* and laboratory punch tests (Liferov and Bonnemaire, 2005).

2.4 Field Tests

In-situ field tests are one of the most promising methods for investigating the mechanical properties of ice ridges at realistic scale (Croasdale *et al.*, 2001). A number of *in-situ* field tests with different methods and setups have been conducted to investigate these properties. For example, the "Direct Shear Test", the "Punch Shear Test" and the "Pull-up Test" measure the shear strength of ice ridges, which is required as input for ridge keel load estimation (Timco *et al.*, 2000). Each of these methods, and associated results will be discussed in the subsections below.

2.4.1 Direct Shear test

The direct shear test is an appropriate method to measure the maximum shear strength at or near the bottom of the ice ridge consolidated layer. Figure 2.13 illustrates the schematic of the direct shear test setup. In this experiment, a section of the consolidated layer (referred to as the ice slab in the image) is pushed horizontally, inducing failure in the rubble below. The ice slab was pushed using a hydraulic ram and associated support frame, which was lowered into a pre-cut trench. At the opposite side, another trench was created to accommodate the displaced ice slab. In order to minimize friction between the ice slab and the surrounding ice cover, a 2*cm* to 3*cm* gap was prepared.

The direct shear setup was successfully used in four separate field campaigns, two in Canada and two in Russia (Croasdale *et al.* 1997, 1998). However, the tests conducted in Sakhalin (Russia) from 1997 to 1998 are still proprietary and only data from the Canadian tests are available. In these studies, the shear strength between the consolidated layer and the ice keel was measured. For this, a 25 tonne hydraulic ram with a 0.6*m* stroke was used, and the displacement was measured by string potentiometers. Also, in order to assess the degree of deformation along the shear plane, Styrofoam rods were placed vertically in holes drilled through the ice slab.

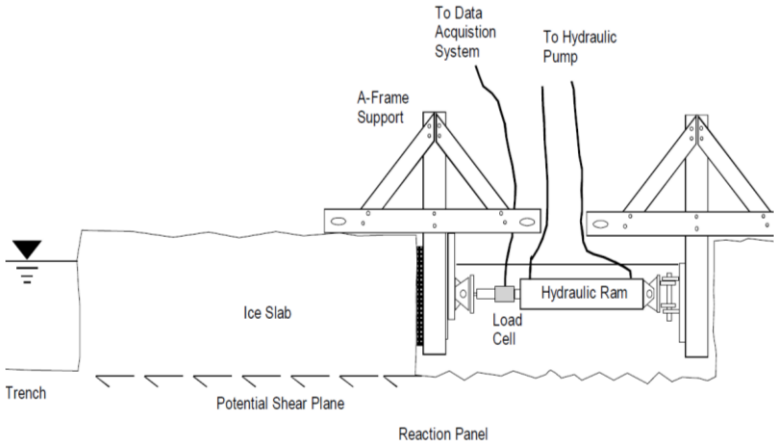

Figure 2.13. Direct Shear Test setup cross section (Timco *et al.*, 2000).

A total of 16 direct shear tests were performed in Canada (11 tests in 1997 and 5 tests in 1998). Croasdale *et al.* (2001) argued that the maximum shear strength can be estimated by dividing the peak load by the plan failure area. Based on that, the results of the tests conducted in Canada in 1997 showed that the maximum shear strength between the keel rubble and the refrozen layer was 22.6*kPa*, with an average of 14.1*kPa* (Croasdale *et al.*, 2001). In addition, by assuming pure friction for the direct shear tests the maximum and average friction angles are 83° and 74°, respectively (Croasdale *et al.*, 2001). The values for the tests conducted in 1998 in Canada were 13.2*kPa* for the maximum shear strength and 9.2*kPa* for the average shear strength.

Figure 2.14 illustrates a typical measured force-displacement in a direct shear test. Referring to the figure, Croasdale *et al.* (2001) argued that the peak loads in the force-displacement curve represent the cohesive bond, in which no movement occurred before the cohesive failure. They also mentioned that the residual constant force is related to the friction force. Timco *et al.* (2000) suggested that this method is appropriate for

modeling and estimating the “global shear plug” failure mode, as in the direct shear test the failure plane approximately occurs near the bottom of the consolidated layer. However, Palmer and Croasdale (2013) argued that the measured shear strength is at maximum value since it is near to the refrozen layer.

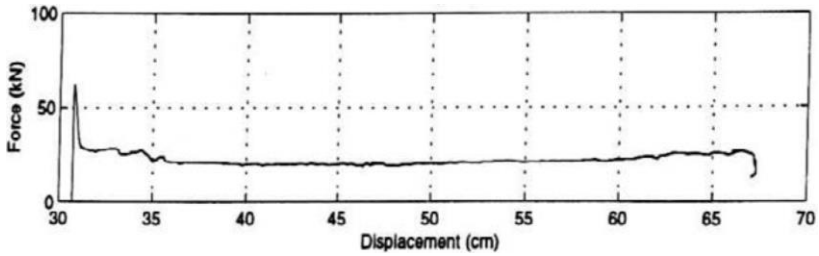

Figure 2.14. Direct Shear Test, load vs. displacement (Croasdale *et al.*, 2001).

Understanding the load applied by ice ridges during the interaction with a structure is crucial, since local passive failure of the ice ridge occurs through the ridge depth and is a function of the average strength of the ice ridge on the failure plane. Therefore, the ice ridge shear punch test is a useful method to measure the average shear strength through the keel thickness.

2.4.2 Punch shear tests

Punch tests are a suitable method to measure the average strength of an ice ridge through its thickness. In a punch test, the indenter (plate) is pushed through the ridge vertically to fail. During the failure, a plug of the ice rubble is pushed down, which provides an estimate of average strength in an ice ridge local passive failure during interaction with offshore structure (Palmer and Croasdale, 2013). Figure 2.15 illustrates a schematic of a punch test setup. Similar to the direct shear test, a section or slab is cut in the

consolidated layer. This slab is then loaded vertically using a hydraulic ram, which pushes a plug of rubble directly downward through the base of the ridge keel. The maximum strength is derived by dividing the pure maximum load (minus buoyancy force) by the failure platen area.

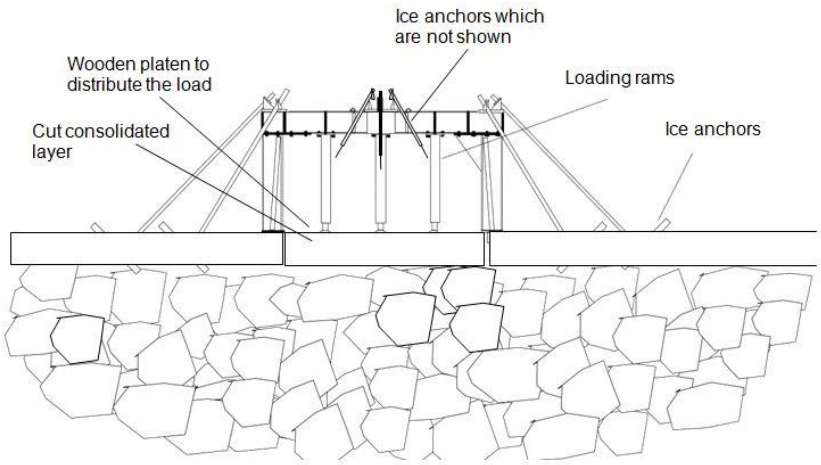

Figure 2.15. Configuration of the Punch Test setup (Timco *et al.*, 2000).

Punch tests were conducted by Leppäranta and Hakala (1992), Timco *et al.* (2000), and Heinonen and Määttänen (2000). Initial *in-situ* punch tests were conducted by Leppäranta and Hakala (1992) to measure the keel strength of first-year ice ridges in the Baltic Sea. However, some of these tests were unsuccessful because the ridges did not fail in those tests. That is because the load was applied by piling up concrete blocks, resulting in an insufficient force to fail an ice ridge. The results of their successful tests showed that the shear strength varied between 1.5*kPa* to over 4*kPa*. A more refined test setup was later developed by Croasdale and Associates Ltd. (1996), which was used in the Northumberland Strait, Canada, and offshore Sakhalin, Russia. In the Northumberland Straight tests a 30 tonne (0.3*MN*) hydraulic ram was employed; whereas, for offshore

Sakhalin the ram capacity was increased to 2*MN*. Toggles and strings where inserted at various locations throughout the keel to measure deformation.

A total of 9 punch tests were conducted in Canada in 1997; however, the results of Sakhalin are still proprietary. The maximum and average shear strength reported in Canada were 12.8*kPa* and 8.5*kPa*, respectively (Croasdale *et al.*, 2001). By assuming pure friction the values of the maximum and average friction angle change to 69° and 57°, respectively (Timco *et al.*, 2000).

Further punch tests were conducted by Heinonen and Määttänen (2000) in the Gulf of Bothnia, Finland. They found the cohesive strength and friction angle values of 2.3*kPa* and 14°, respectively, which are in the same order as the results of Leppäranta and Hakala (1992) and Weiss *et al.* (1981). Heinonen and Määttänen (2000) were of the opinion that the strength parameters analyzed above are the minimum values due to the uneven stress distribution, which causes a progressive failure to occur. The authors also argued that a higher frictional load may exist in the middle part of the ice ridge keel, where the failure pressure against the failure surface is higher.

Figure 2.16 illustrates a typical force-displacement sample for a punch shear test conducted by Timco *et al.* (2000). Similar to the direct shear test (see Figure 2.14), the maximum force value is reached after a very small displacement. However, Figure 2.16 shows no drop in the punch shear load. Croasdale *et al.* (2001) argued that it may be due to a progressive failure in the ice ridge or high residual friction between the blocks. In contrast, Figure 17 demonstrates a typical force-displacement observed by Smirnov *et al.*

(1999) in Sakhalin, where two peak loads occurred. Timco *et al.* (2000) argued that the first failure results were due to the breaking of cohesive bonds and the later one relates to the global plug failure.

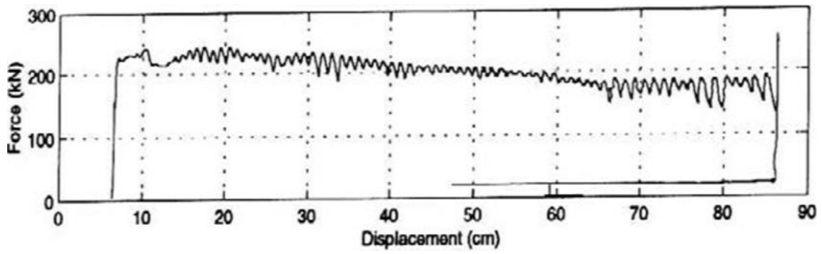

Figure 2.16. Load and displacement plots, punch shear test (Timco *et al.*, 2000).

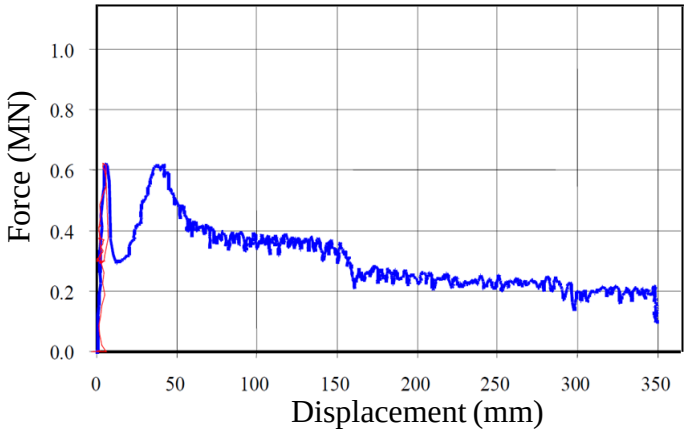

Figure 2.17. Typical load trace from a punch shear test (Smirnov *et al.*, 1999).

It is noteworthy that based on the results of the 1997 study (Croasdale *et al.*, 2001), the average punch shear strength was about half of the average direct shear test strength. Croasdale *et al.* (2001) argued that the ridge keel shear strength may vary from near zero at the bottom of the keel to its maximum value just below the refrozen layer.

Liferov and Bonnemaire (2005) compared the results of *in-situ* punch tests which had two peak loads with the direct shear box test conducted by Hellman (1984). Although in the later study mush ice was used, a similar behavior was observed between the force-displacement curves (see Figure 2.18). Referring to the figure, the maximum shear force occurred at the second peak load in the direct shear box test. However, this was observed at the first peak in the *in-situ* punch test. Liferov and Bonnemaire (2005) addressed that to the dissimilarity in the test setup, thermodynamic scaling and density of ice rubble.

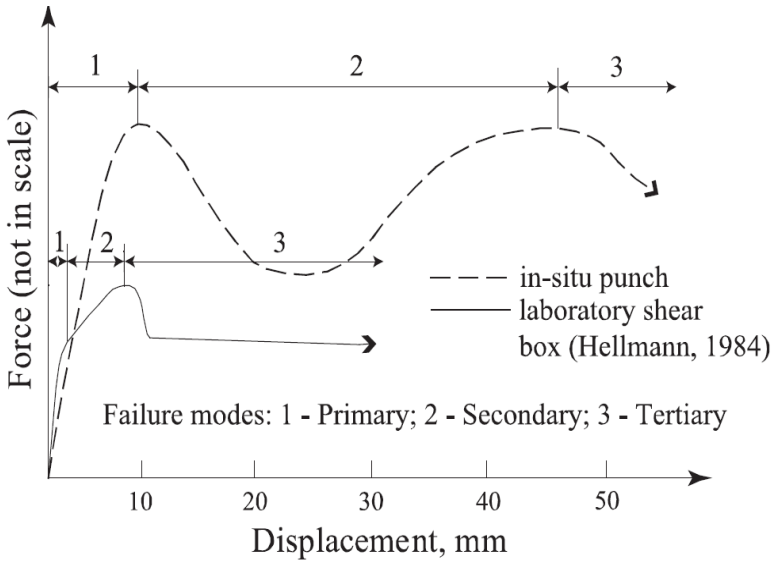

Figure 2.18. A schematic force-displacement diagram compares the *in-situ* punch tests with laboratory shear box tests conducted by Hellman in 1984 (Liferov and Bonnemaire, 2005).

2.4.3 Pull-up test

The pull-up test was employed in order to measure the tensile "cohesive" strength between the consolidated layer and the underlying ice rubble. This method is largely

similar to the punch test, with the difference being that the consolidated layer is pulled up to fail any bonds between the ice slab and underlying rubble. Figure 2.19 illustrates the configuration of the pull-up test. Croasdale *et al.* (1997, 1998) performed *in-situ* pull-up tests to measure the cohesive strength between the ice ridge consolidated layer and underlying ice rubble. These tests were conducted in both Canada and Sakhalin (Russia); however, the results of Sakhalin tests are proprietary.

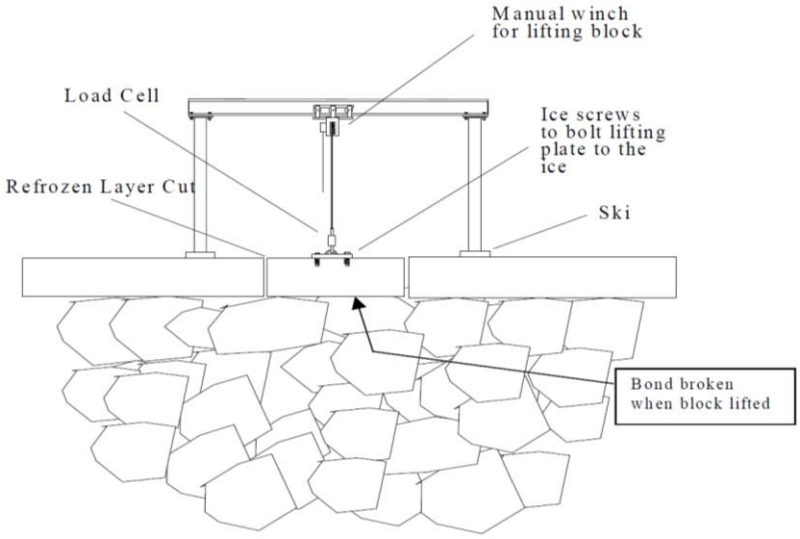

Figure 2.19. Configuration of the pull-up test setup (Timco *et al.*, 2000).

The authors defined the tensile strength as the maximum load divided by the area of the block being pulled. In the tests conducted in 1997, the highest and the average tensile strength were measured at 26*kPa* and 17*kPa*, respectively (Croasdale *et al.*, 2001). However, the maximum and average values for the 1998 tests were 9*kPa* and 6.2*kPa*, respectively. The authors argued that the lower values in the 1998 tests were likely due to air temperature, as the average ambient air temperature in 1998 was significantly higher (-1.6℃) than in 1997 (-4.5℃). This is not surprising as the ice blocks are beneath the

consolidated layer, and may be influenced by atmospheric cooling. As the measured tensile strength area is exactly under the consolidated layer, which is influenced by heat conduction through ice blocks and by decreasing the air temperature, ice freezing increases and results in a higher number of contacts between the ice blocks (Palmer and Croasdale, 2013).

Figure 2.20 illustrates a typical result for the pull-up test. According to the figure, the first peak load represents the tensile cohesion failure and the residual increasing trend shows the effect of buoyancy, since the buoyancy force decreases when the ice plug is pulled up and more force is required to resist gravity (Palmer and Croasdale, 2013). They also predicted that if no cohesion existed in the interaction area, the whole load trace would be similar to the second slope.

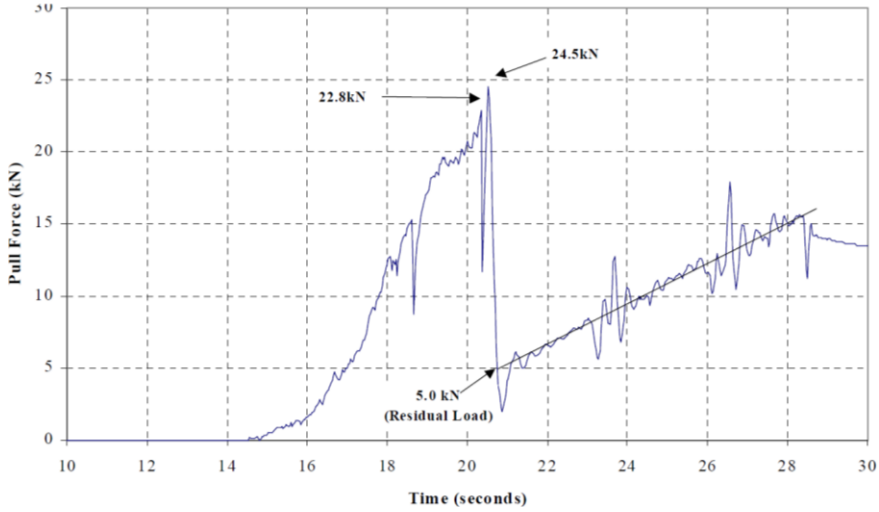

Figure 2.20. Typical pull-up test load trace showing distinct tensile bond (Timco *et al.*, 2000).

The keel strength in the direct shear tests and punch tests was determined by two frictional and cohesion parameters; however, the results of pull-up tests demonstrate that cohesion plays a key role. This is in support of Liferov and Bonnemaire's argument (2005), as they discussed that the cohesive and frictional properties are not additive, because at the initial phase of the tests the ice ridge bonds have to fail and then reach the residual friction. Additionally, Palmer and Croasdale (2013) expected a considerable scatter in their results as they argued the number of contact points between the underlying ice blocks and the blocks being pulled up may not be the same. Moreover, Croasdale *et al.* (2001) argued that the higher cohesive strengths could have been attributed to the consolidated layer not being completely cut through.

2.5 Summary

As reviewed in previous sections, a wide range of methods have been employed to investigate the mechanical properties of ice rubble and ice ridges in both laboratory and field tests. *In-situ* field tests have the advantage of being able to measure the strength and other mechanical characteristics of full-scale ice rubble and ridges. However, developing and validating a constitutive model is complicated with this method. This is because manipulating boundary conditions and observing ice rubble and ridges failure are difficult tasks in field tests. Also, *in-situ* tests are costly, logistically complex and time consuming, which is why only a limited number of field tests have been conducted worldwide (about 40 – 50 data points in total).

Laboratory tests are valuable for investigating the mechanical properties of ice rubble and ridges at the microscopic level (block-block contact) to see the possible failure modes.

Unlike *in-situ* field tests, laboratory scale tests have the advantage of being able to manipulate the boundary conditions, such as the history of ice and ambient temperature, as well as the geometry and dimensions of the blocks. Therefore, laboratory tests are a valuable approach for investigating the mechanical properties of ice rubble and ice ridges, such as possible failure modes for block-block contact.

As discussed, most studies describe the strength of ice rubble and ice ridges as a function of cohesion and friction between ice blocks, which is known as the Mohr-Coulomb constitutive model. Timco and Cornett (1999) argued that the wide range of results seen across various laboratory experiments can be interpreted as the direct effect of different test setups and methodologies. In other words, the wide range of values may be because no standardised method exists for producing ice rubble in modelling facilities and experiment setups. Bailey *et al.* (2015) argued that the Mohr-Coulomb model is not an appropriate tool for determining the strength of ice ridges, as the friction of ice ridges and ice rubble is a combination of contact friction and interlocking between the blocks, which the model does not account for. Additionally, they argued that the cohesion between ice blocks is dependent on freezing/sintering, making it a unique solid particle, as soil particles, which are generally dependent on electrostatic attraction. Bailey *et al.* (2015) further argued that in the Mohr-Coulomb model, the FB is assumed to only fail in shearing. In reality, many different scenarios are possible during ice rubble and ridge deformation, such as FB failure, locking, rotation and rearrangement of the ice blocks, and failure of the individual ice blocks (Shafrova and Høyland, 2008). Also, the ice blocks' failure as well as tensile or compressive FB failure may contribute to the failure

of the whole sample, allowing the possibility that the sample fails in a combination of shearing and tension (Liferov *et al.* 2002).

While laboratory scale punch tests have been conducted in a way that provides a general overview of the mechanical properties of ice ridges, the effects of parameters such as initial ice temperature, consolidation time, pressure confinement, ice blocks' dimensions and beam porosity are still unknown.

To address these gaps, the program of research presented in this thesis has been conducted to investigate the effects of: I) consolidation time, II) pressure confinement, III) sintering and IV) ice block dimensions, on the strength and failure behavior of a freshwater ice rubble beam. Additional discussion of each parameter is described below, along with identification of specific aspects studied in this thesis:

I) Consolidation time: As shown in Section 2.2, FB strength varies by increasing consolidation time, and reported strength varies between $1 kPa$ and $1583 kPa$ (Bailey *et al.*, 2015). As a consequence, consolidation time is one of the parameters identified as potentially having a high impact on the strength of ice rubble and ridges. As reviewed in Section 2.3.5, in prior test programs the strength of the longest consolidated ice rubble beam was 3 hours, which was conducted by Azarnejad and Brown (2001). In this project, the effects of higher consolidation times (up to 3 days) have been investigated, since rubble in nature has much longer to consolidate than has been captured in previous tests reported in the literature.

II) Confining pressure: There is a lack of knowledge about the effects of confining pressure on the degree of freeze bonding between ice blocks. As mentioned in Section 2.2, confinement significantly affects the degree of consolidation. Investigating the effects of confinement has been identified as a valuable topic for understanding the mechanics associated with the development of strength and also the failure behavior of freshwater ice rubble. As estimated by Bruneau (1997) and Bailey *et al.* (2015), the confinement pressure for a 10*m* ice ridge with 0.3 porosity can reach about 70*kPa* by assuming that only 10% of blocks are in contact. In this project, pressure confinements of 10*kPa*, 25*kPa* and 40*kPa* were investigated.

III) Initial temperature: As previously discussed in this chapter, the temperature of ice rubble considerably affects the strength of ice, FB and sintering processes. However, the specific effects of the initial temperature and sintering on ice rubble strength have yet to be studied in depth. In this work, two temperatures have been tested (-18℃ and 0℃) to investigate the effects of freeze bonding/sintering on the mechanical characteristics of ice rubble.

IV) Ice block dimensions: In this experiment, larger ice blocks were used to model a medium-scale ice rubble beam. This allowed the ice blocks to have sufficient cold reserves to establish FBs. In comparison to previous studies (Azarnejad and Brown, 1998, 2001; Lemee and Brown, 2002) this project had varying ice length and width dimensions ranging from 10*cm* to 50*cm* in which the majority of the blocks' lengths and widths fell in a range between 30*cm* to 40*cm* and 20*cm* to 30*cm*, respectively. The

thickness of ice rubble was approximately 10*cm*. In addition, one test was conducted to investigate the effects of smaller ice blocks on the strength and failure behavior of ice rubble. In this test, the maximum ice block lengths fall in the range of 20*cm* and 30*cm* and the maximum ice blocks width between 10*cm* to 20*cm*.

Based on the gaps and specific tasks identified above, a systematic research program has been completed. The approach used in this program was to conduct a series of medium-scale laboratory ice rubble beam tests (punch tests). The aim of this work has been to measures the average strength of the ice rubble through the thickness. Furthermore, this model mimics the local passive failure during ice ridge-structure interaction (Palmer and Croasdale, 2013). In this study, the box setup allows the boundary conditions to be controlled, and through the use of load cells, string potentiometer, Micro-T wireless temperature sensor, High Speed Video Camera (HSV) and Resistance Temperature Detectors (RTDs), the effects of the above variables on ice rubble strength could be studied. By studying the effects of these parameters the goal of this work is to help develop deeper insight about the mechanical characteristics of ice rubble and ice ridges and the underpinning physics.

Details of the experimental setup and methodology are provided in the next chapter.

3 Methodology

In the previous chapter, laboratory and *in-situ* field tests on ice rubble were reviewed and gaps in previous research identified. It was found that the effects of consolidation time, pressure confinement and freeze bonding/sintering on the mechanical characteristics of ice rubble and ridges are still uncertain. As a result, a series of ice rubble beam tests were conducted in C-CORE's Cold Room facility to investigate these parameters in more detail. In this chapter the methodology for the test program is presented. In Section 3.1, the apparatus and instrumentation is described. The methodology for producing ice rubble is described in Section 3.2, as well as the image analysis process used for measuring the ice block dimensions. The test procedures for the 'punch' and 'friction' test are described in Section 3.3.

3.1 Apparatus and Instrumentation

3.1.1 Testing Box

A custom-made box has been constructed for the experiment program with dimensions of 3.05m in length and 0.94m in width and height (see Figure 3.1). As illustrated in Figure 3.2, the box is on wheels and has a steering mechanism so that it can be easily moved into and out of the cold room for setup and testing. The walls are made from Plexiglas (with a grid drawn on) so that failure mechanisms and ice block motions can be observed and tracked. The platen was chosen to be rectangular and span the entire width of the box so that failure mechanisms can be observed. A platen width of 0.4m was chosen based on careful consideration of the influence that the platen width will have on the bending/shearing properties of the beam. The platen area is a critical parameter in the

test program, as it influences the stress distribution through the ice rubble, the type of failure behavior (trapezoidal or rectangular), the nominal pressure, the effective platen width (Lemee and Brown, 2002) and the effects these have on the deflection of the beam in bending. Based on a thorough investigation of these factors (see Appendix A for more details), a platen dimension of $0.94m \times 0.4m \times 0.02m$ (length, width, thickness) was chosen. Load was applied to the platen using a $20{,}000lbs$ (9 tonne) hydraulic ram, which has a stroke of $30.5cm$ and a bore diameter of $8.25cm$.

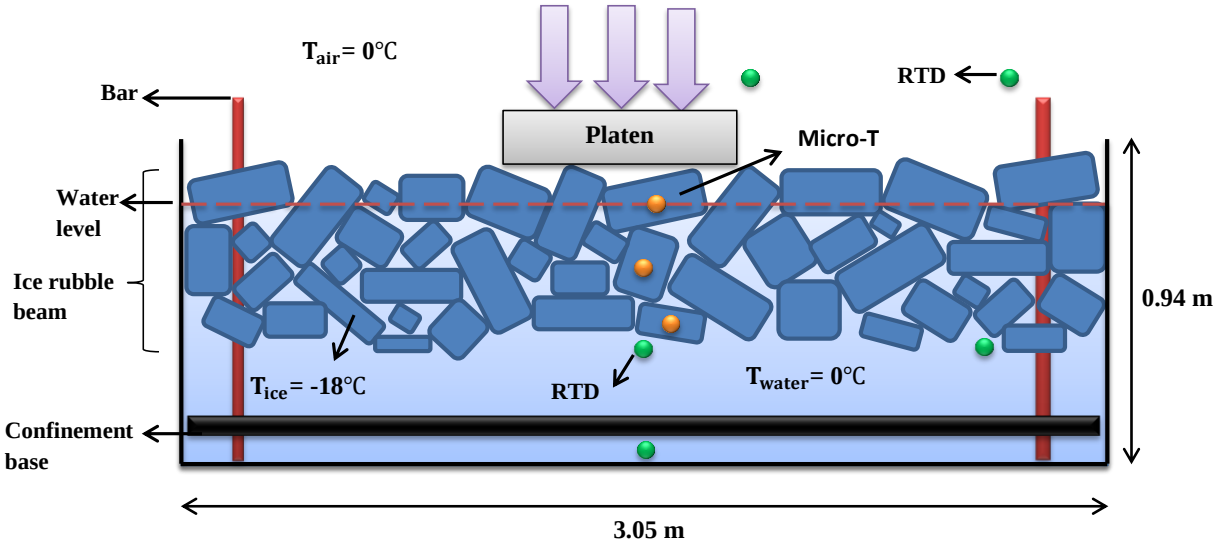

Figure 3.1. Schematic of the ice rubble beam test showing approximate Micro-T and RTD positions (not all rods included in this schematic).

Confinement was applied to the rubble using two plates positioned above and below the ice beam (see Figure 3.2). The bottom confinement plate is mounted on 8 threaded rods, which allow it to travel the full depth of the box. The bottom plate is brought up to help construct a leveled ice rubble beam and to apply confinement. The top confinement plate is mounted on the hydraulic ram, which applies the load to the rubble during

confinement. The confinement system has the capacity to apply a stress of up to $40kPa$. Note that confinement is only applied during the consolidation period. Therefore prior to failing the beam, the top confinement plate is removed from the ram and replaced with the $0.4m$ wide punch platen and the bottom plate is lowered to the bottom of the box.

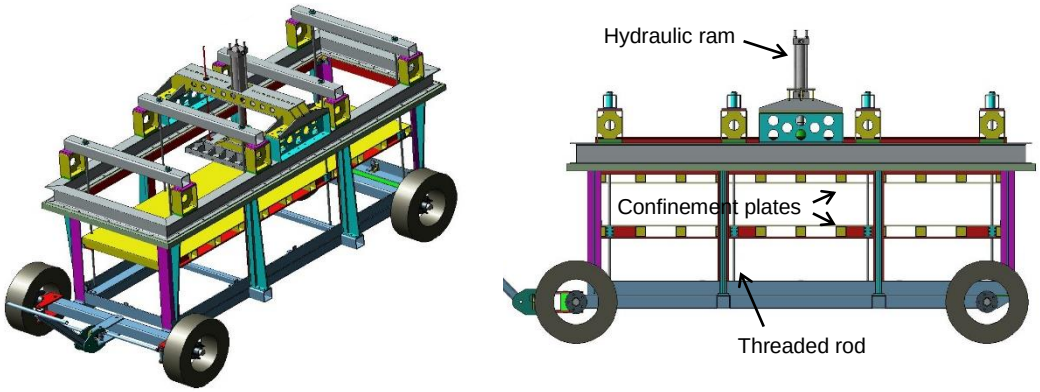

Figure 3.2. Computer aided design (CAD) images of the box assembly.

During tests where the rubble was heavily bonded, the buoyancy of the non-loaded portion of the rubble was not sufficient to resist the applied load. As such, brackets had to be added to the end of the box to cause the beam to fail. This is similar to the procedure used by Azarnejad and Brown (2001) where they glued small Plexiglas pieces on the tank walls to artificially increase friction between the tank walls and the ice rubble. The only difference here is that friction was only added to the ends of the box rather than the whole box, to allow beams to fail in bending as well as shearing.

Two types of brackets were used to apply friction, which are referred to as E- and C-brackets (Figure 3.3a). The distance between the prongs on the E- and C-brackets were

15*cm* and 30*cm*, respectively. The brackets were made to hang over the side of the testing box so they could be easily moved depending on test conditions. For the consolidation time and sintering tests, four (4) E-brackets were used, two positioned at each end of the beam. In the tests where confinement was applied, additional frictional resistance was needed to fail the beam, therefore an additional four (4) C-brackets were added, one on each sidewall 30*cm* from the end-wall (Figure 3.3c).

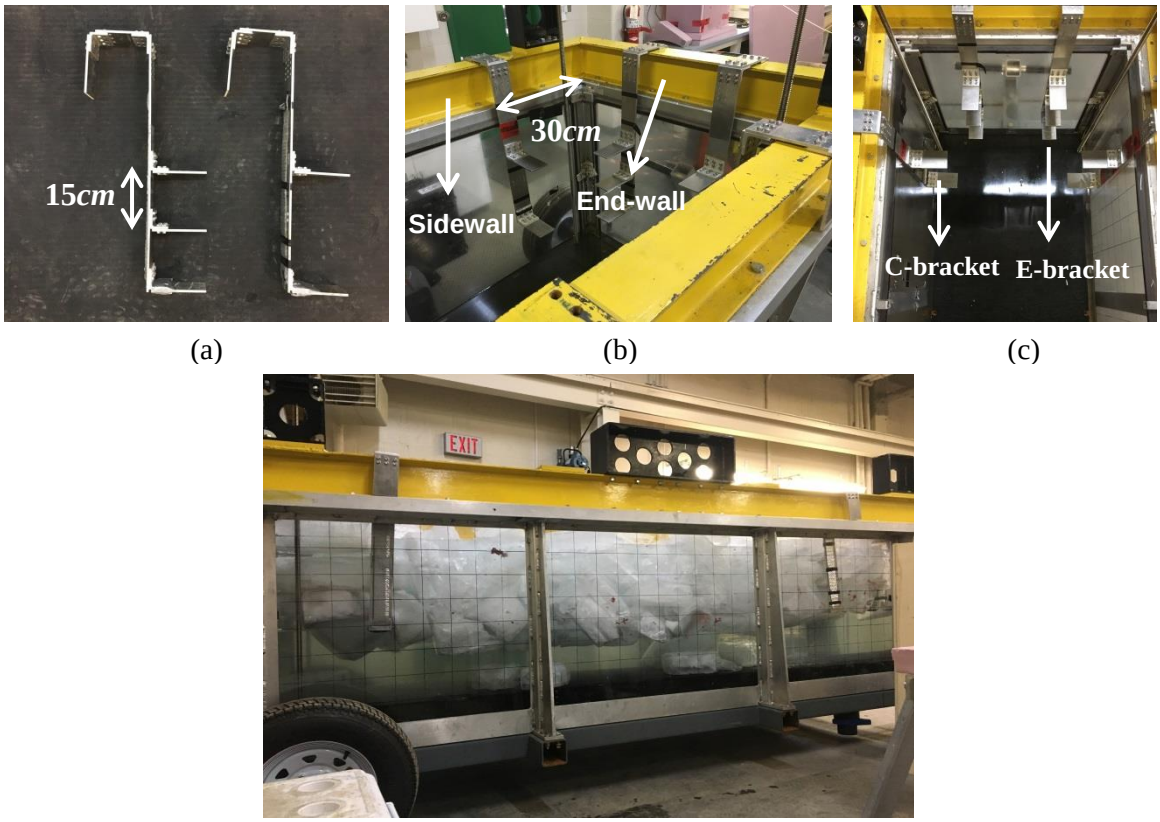

(a) (b) (c)

(d)

Figure 3.3. (a) E-bracket (left) and C-bracket (right). (b) The brackets hang on the edges. (c) Brackets position from the top view (in one side of the box). (d) The ice rubble beam with C-brackets.

3.1.2 Instrumentation

A summary of the instrumentation that was used in this study is given in Table 3.1. All instrumentation was tested, calibrated, and data sheets prepared prior to the start of the test program. More detail for each item is provided in the subsections below.

Table 3.1. Instrumentation.

Instrument	Quantity	Function
String Potentiometer	1	Measure vertical displacement and velocity of platen/ram
Load Cell	1	Measure the vertical applied load on platen
Micro-Ts	6	Measure ice block temperature at strategic locations
Resistance Temperature Detectors (RTD)	5	Measure air and water temperatures at strategic locations
High Speed Video Camera	1	Monitor deformations and failure planes during the test
GoPro Camera/Camera	4	Provide additional angles for viewing the test

3.1.2.1 Load, Displacement, and Velocity Measurements

A 25,000*lbs* load cell was placed in line with the hydraulic ram to measure the force applied to the platen. A string potentiometer was used to measure the vertical displacement and velocity throughout indentation. These measurements provided a representation of the strength of the ice rubble matrix under various test parameters.

3.1.2.2 Temperature sensors

Measuring the temperature changes in the ice blocks during consolidation provides valuable information about the rates of heat transfer through the rubble. This is important, as it will directly influence the degree of bonding between ice blocks (freeze bonding) and in turn the mechanical properties of the rubble. Micro-T sensors from Phase IV

Engineering were used to measure the temperature of the ice blocks. Micro-Ts are small (1.3*cm* diameter) wireless data loggers that can be frozen into selected ice blocks prior experimentation. They were inserted into the ice blocks by drilling a small hole, slightly larger than the diameter of the sensor, placing it in the hole and re-filling it (see Figure 3.4). As Figure 3.5 shows, a ribbon was also frozen into each ice block containing a Micro-T to make it easily identifiable for recovery after the test. A total of six (6) ice blocks contained Micro-Ts during the test, which were placed at strategic locations in blocks of varying sizes (see Figure 3.6). Micro-Ts logged data at a sample rate of 2 minutes, initiating when they were in the container.

Figure 3.6 illustrates half of the box filled with ice rubble. Referring to the figure, the ice blocks were positioned at three different levels; the top, the middle and the bottom of the ice rubble beam, respectively. In most of the tests, the Micro-T ice blocks were positioned in the 1, 2 and 3 locations. One block was positioned at the central part of the beam (location A) and one at the left side of the beam (location B).

Five (5) resistance temperature detectors (RTDs) were used to measure air and water temperatures. Three (3) RTDs were placed in the water, two directly underneath the ice rubble beam (one at the centre of the box and the other at one end) and one at the bottom of the box (see Figure 6). As shown in the figure, the RDTs were passed through the tubes to protect them from getting squeezed by ice rubble. Two (2) RTDs were placed in the air to measure cold room temperature at different locations. In some tests, one of the RTDs that measured air temperature was placed at the ice rubble-air interface. RTDs

measurements were logged at a sample rate of 1 minute, starting from the time that the box filled with ice rubble. Once testing was finished, the Micro-Ts were removed from the blocks, and the data uploaded and synchronized with the RTD's readings.

Figure 3.4. Micro-T placement in ice blocks.

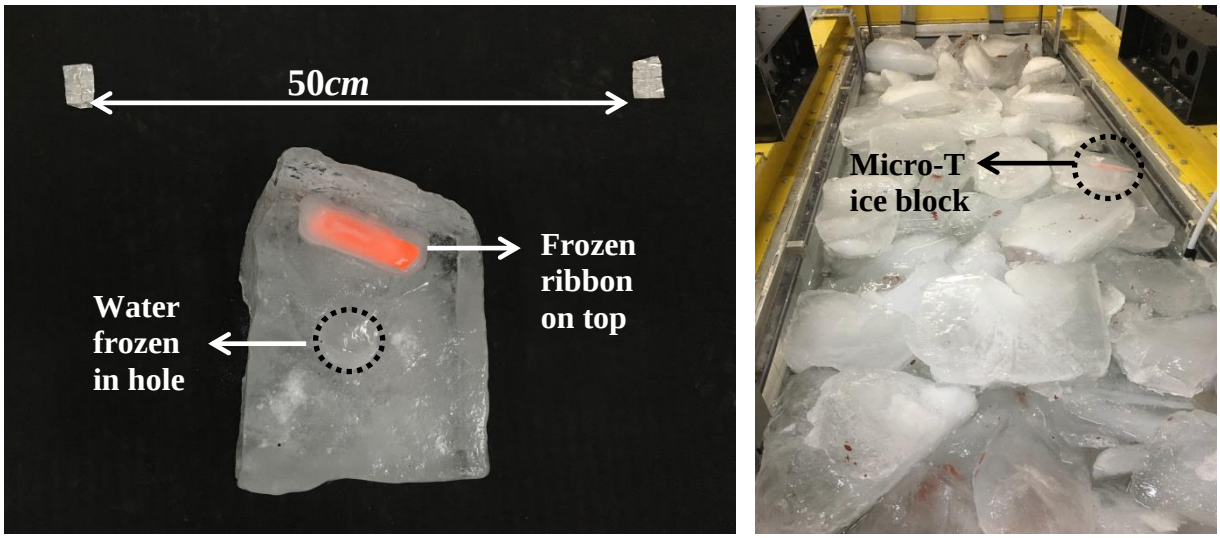

Figure 3.5. Ribbon frozen into the ice block containing the Micro-T (a) so that it can easily be identified in the ice rubble beam (b).

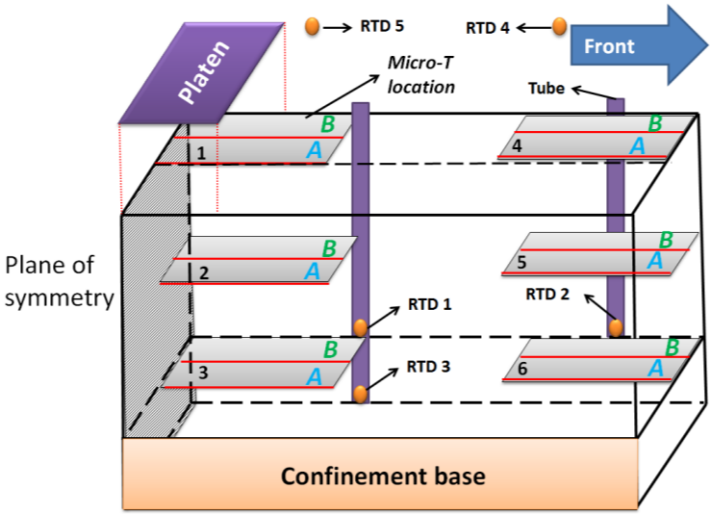

Figure 3.6. Micro-Ts and RTDs positions in the ice rubble tests.

3.1.2.3 Observation Equipment

To ensure clear observation of the test, the walls of the box were constructed from transparent Plexiglas. A 10*cm* grid was drawn on the side of the box to track block movements as a function of a known distance. A total of five (5) cameras were used to observe the tests from different views. Four were placed side-on to view the test through the Plexiglas window and one from the top of the box (see Figure 3.7a). A High Speed Video camera (HSV) was used to view the mid-point of the beam and two Digital SLRs (Camera 1 and 2) to view the left and right side of the beam (Figure 3.7b). Two GoPro cameras were used to observe a wide angle view: one was mounted on top of the HSV and the other at the top of the box. Three LED work lights were mounted on the opposite side of the punch box to illuminate the ice rubble beam (see Figure 3.7c). Cameras were syncronizedwith the load and displacement data so that each load drop could be linked to an observed failure, which is needed to estimate the failure area and mode of failure (shearing or bending).

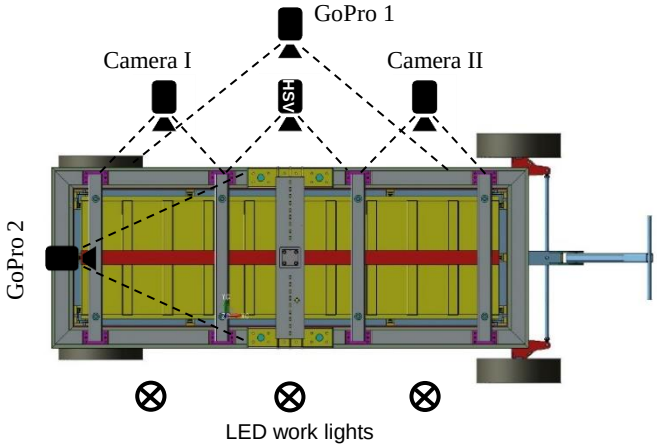

(a)

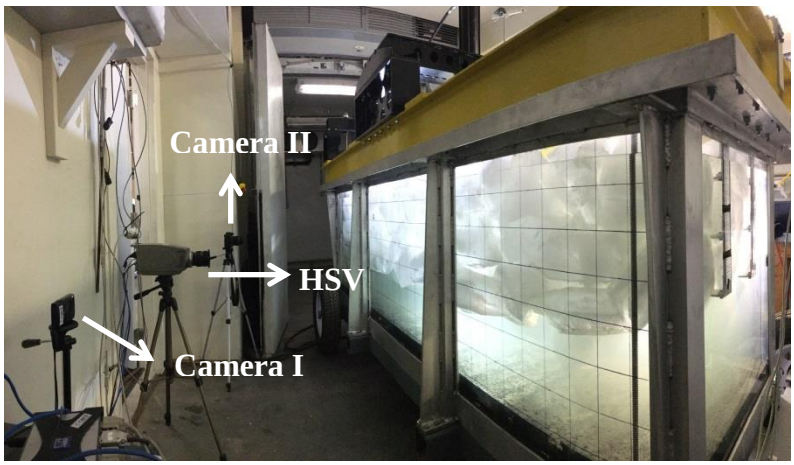

(b)

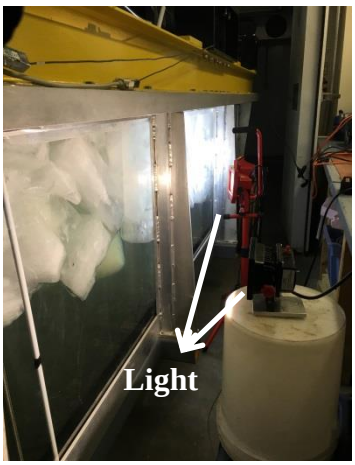

(c)

Figure 3.7. Camera and lighting locations.

3.2 Ice Rubble Production

Freshwater ice rubble was produced using the same methodology as in the DIRKS tests program (Bailey *et al.* 2014a,b). Ice rubble was fabricated and stored in a 40*ft* refrigerator container (length: 12*m*, width: 2.3*m*, height: 2.3*m*) located outside the C-CORE centrifuge building (see Figure 3.8a). A set of $1m^2$ pans were filled with tap water to an approximate depth of 10*cm* and left to freeze at a nominal temperature of -18℃. Two

dividers were placed in each pan prior to freezing to facilitate later ice breakage (see Figure 3.8b).

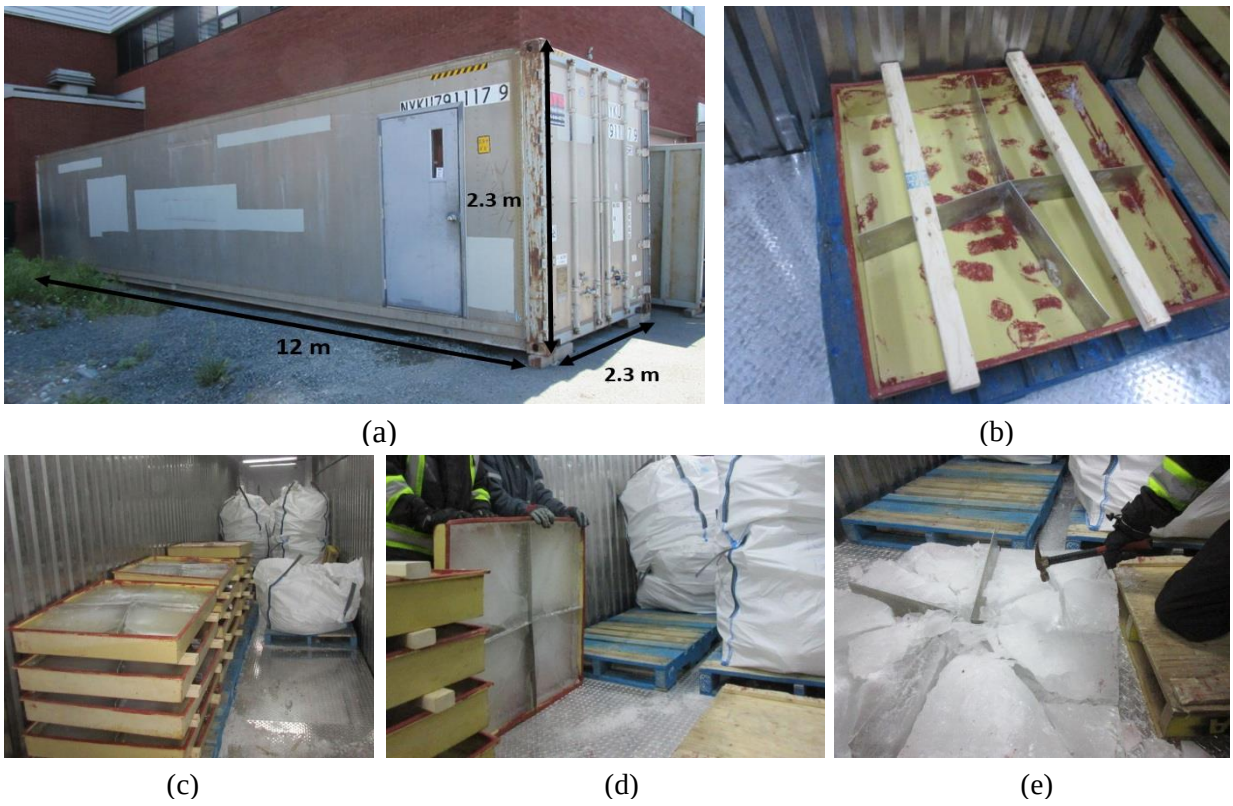

Figure 3.8. (a) Reefer Unit and its dimensions. (b) Ice pan atop a pallet with L-dividers and 2 × 4 wooden spacers. (c) Frozen pans, storage bags. (d) Breaking ice out of pans. (e) Separating ice into blocks.

Up to five pans were stacked on top of a pallet with wooden two-by-fours between the pans to provide sufficient air circulation. Once the water was frozen (approximately 5-6 days), pans were manually flipped over, allowing the ice to break into randomly sized pieces. Larger sized ice pieces were broken with a hammer to yield target lengths. Target lengths for the large block tests (Tests 1-Test 18) were between 10*cm* and 50*cm* and for the small ice block test (Test 19) were 10*cm* to 30*cm*. Small fragments and crushed ice less than 10*cm* in thickness were swept away and discarded, so that boundaries between

ice blocks could be clearly identified and to simplify the ice block dimensions analysis. It is recognized that this resulted in less brash ice being present between the ice blocks (which also resulted in a slightly higher porosity), but this was seen as necessary to be able to view the block-block interactions with greater clarity. It is recommended that future experiments be conducted including this brash to study the influence of the brash on the processes and associated strengths, but it was beyond the scope, schedule and budget to conduct additional tests containing brash in the present program. The ice rubble was then collected by hand and stored in large soil bags, atop a pallet so that they can be easily maneuvered when ready for testing. Each soil bag was labeled with the nomenclature shown in Figure 3.9. Approximately 10-12 pans of ice were needed to produce a 50*cm* thick ice rubble beam.

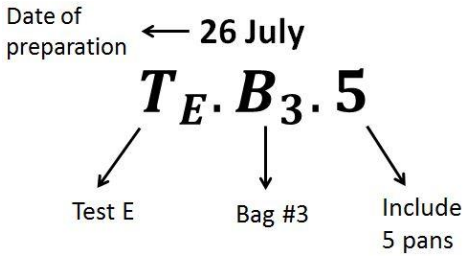

Figure 3.9. Soil bags are labeled with test letter, bag letter, and number of pans.

Ice rubble was stored at two different temperatures; -18℃ for consolidation time, pressure confinement and small ice block tests. Ice for tests on initial ice block temperature/sintering was stored at -5℃. In sintering tests, after preparing and storing a sufficient number of ice blocks in soil bags, the container temperature was set to -5℃ for a week. Before making the ice rubble beam, the soil bags were left at room temperature in the lab to warm up approximately 0℃. For this, the temperature of some ice blocks

was monitored by drilling a hole into the centre of the blocks and inserting a handheld temperature probe.

3.2.1 Ice Block Dimensions Analyzed Through Image Processing

An analysis of the ice block dimensions was carried out to determine ice block length, width and volume distributions, which are important for understanding the mechanical behavior of ice rubble. This data can also be helpful to estimate the number of interactions between blocks for the comparing future numerical simulation. Photos of the ice blocks were taken during ice rubble fabrication and later analyzed using image processing software. Ice blocks were placed on a sheet of black rubber (area of $1.8m^2$) to take the photograph, which provides a good color contrast to the ice and does not reflect light. An adequate separation between ice blocks ($\sim 5cm$) was needed so ice pieces could be easily distinguished by the image analysis software. A scale was also placed on the rubber as a reference length for pixel sizes. In addition, the thickness of some ice blocks was measured to estimate the ice volume. The image processing software eCognition Developer was used to analyze the photographs, which detects the ice blocks and measures the maximum length and width in pixels. The pixels were then converted to centimeters (using the reference scale) in Excel and plotted in a histogram in MATLAB.

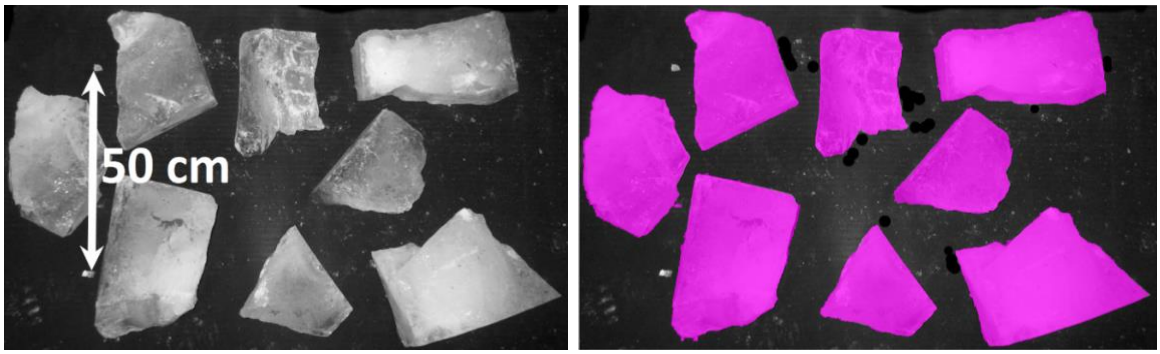

(a) (b)

Figure 3.10. (a) Example photograph taken for ice block dimension analysis. Note the 50*cm* scale and non-reflective black material used to provide sufficient contrast to ice for image analysis. (b) Detected ice blocks in eCognition Developer software.

For the first five tests[2] and Test 19, images were taken of each ice piece used. From the sixth test onwards, images were no longer taken as it was very time consuming and the analysis showed that there was little variability between tests. Figure 3.11 gives the histogram of the length, width and length to width ratio for all images taken of the large ice blocks (for histograms broken down by test see Appendix B). The length distribution of the large ice blocks varied between 10*cm* and 70*cm*, with the majority falling in the range of 30*cm* to 40*cm*. The width distribution varied from 10*cm* to 50*cm*, with over 60% of the blocks being between the ranges of 20*cm* to 30*cm*. The length to width ratio distribution shows that the ice blocks are generally square shape with a maximum length to width ratio between 1 and 1.5. The thickness of the ice blocks that were measured manually showed that the majority of ice block thicknesses fall between 10*cm* and 12*cm*.

[2] This include three shakedown tests and Test 3 and Test 6

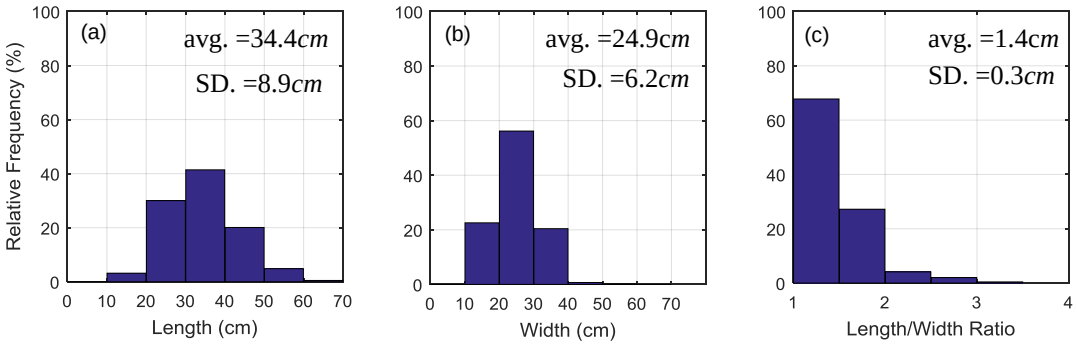

Figure 3.11. Histograms of the length (a), width (b) and length to width ratio (c) of the ice blocks for the first five tests.

One test was carried out (Test 19) to investigate the effects of smaller ice blocks on the strength and failure behavior of ice rubble beams. Figure 3.12 illustrates the histogram of the smaller ice block dimensions measured for Test 19. The distributions for length and width varied between 10*cm* to 60*cm* and 10*cm* to 40*cm*, respectively. While the range of the length and width distributions was similar to the large block tests (Figure 3.11), the majority of the blocks (approximately 90%) had lengths that were 20*cm* to 30*cm* and widths that were 10*cm* to 20*cm*. The length to width ratio of the small blocks (Figure 3.12c) varied from 1 to 3, with the majority of the ice blocks length to width ratios falling between 1 and 1.5.

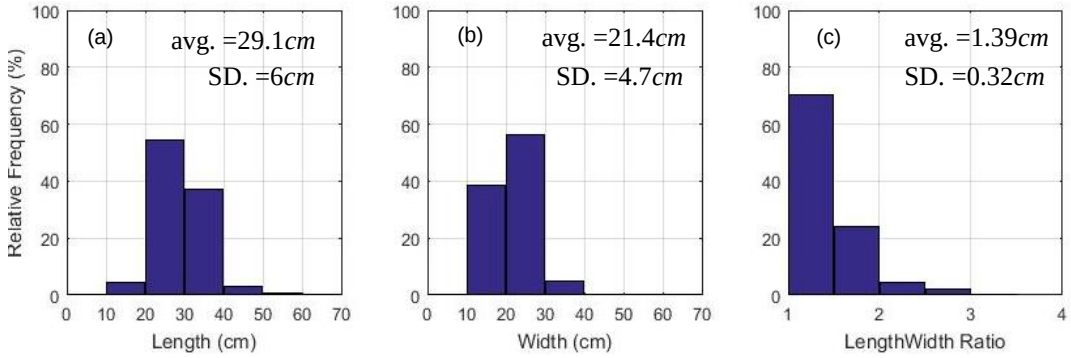

Figure 3.12. Histograms of the length (a), width (b) and length to width ratio (c) of the ice blocks for Test 19.

3.3 Test Procedure

Throughout the tests, the cold room was set to a nominal temperature of $0°C$ to keep the water as close to its freezing point as possible without a consolidated layer forming. Approximately $750kg$ of ice rubble (about 12 pans or 2-3 bags) were needed to produce a 50-cm-thick ice rubble beam. Bags were transported using a forklift from the refrigerator container to C-CORE's Centrifuge building area (just outside the cold room), where they were loaded into the box with the use of an overhead crane. The mass of each ice rubble bag was measured using the crane scale, which is needed to derive porosity. While loading the ice rubble into the box, the bottom confinement plate was positioned $50cm$ from the top of the box (Figure 3.13a), which helped to produce a beam of even geometry. The process of loading the ice rubble into the box was conducted by ripping the ice rubble bags on top of the box. This helped to make an ice rubble beam with a randomized blocks orientation. However, some blocks were randomly relocated and distributed by hand to level the beam. It should be noted that local ice block impacts on the confinement plate was minimized in this process, as the bottom confinement plate

was lower than the water level during the box filling process. During preparation of the ice rubble beam, ice blocks containing Micro-Ts were added at strategic locations (see Figure 3.6) and the time inserted was noted for analytical purposes. Once the ice rubble beam was prepared (Figure 3.13b), the bottom confinement plate was lowered (Figure 3.13c) allowing the rubble beam to float in hydrostatic equilibrium. For tests where no confinement pressure was applied, the box was returned and the ice rubble left to consolidate for a set period of time.

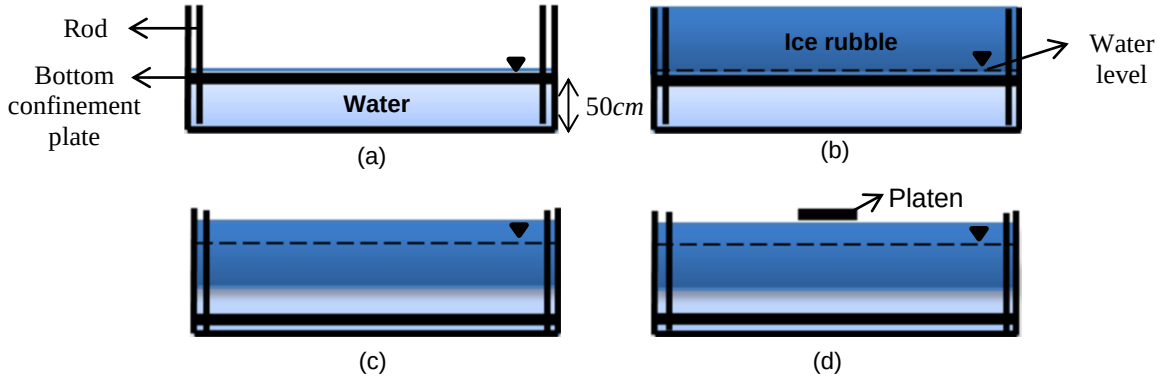

Figure 3.13. The test procedure for consolidation time and sintering tests: (a) Bringing up the bottom confinement plate. (b) Filling the box with ice rubble. (c) Lowering down the bottom confinement plate. (d) Pushing the platen through the ice rubble beam (punch test).

For tests where a pressure confinement was applied, the bottom confinement plate was brought up until a small load was registered on the load cell. The top confinement plate was then lowered using the hydraulic ram until the required load/confining pressure was reached (Figure 3.14d), which was maintained for the full consolidation period. After consolidation, the top confinement plate was removed and the bottom plate lowered to the base of the tank ready for testing.

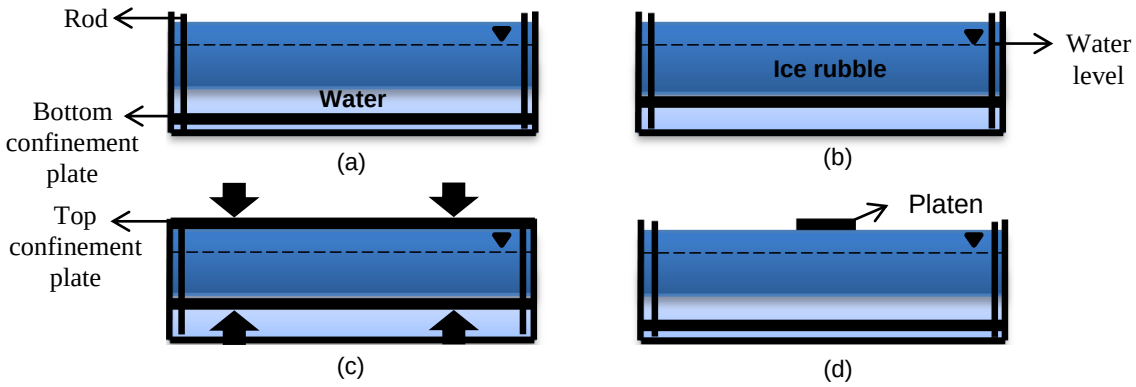

Figure 3.14. The test procedure for the pressure confinement test: (a) Filling the box with ice rubble. (b) Bringing up the bottom confinement plate. (c) Lowering down the top confinement plate and confining the ice rubble beam. (d) Removing the top confinement and lowering down the bottom confinement to do the punch test.

Two tests were carried out on each ice rubble beam: 1) punch test and 2) friction test. The punch test on the ice rubble beam was completed by deforming it at a constant rate of 5*mm/s* until the beam failed. After each punch test, the hydraulic ram was retracted, causing the rubble beam to settle back to its pre-test position. A second test was then performed that was referred to as the friction test as it was assumed that all bonds would have failed in the previous test and as such would be a measure of the friction and interlocking between ice rubble blocks.

The results of these experiments are discussed in the next chapter.

4 Results

In this chapter the results of freshwater ice rubble tests are presented. The test matrix, which details the parameters and conditions used for each test are first discussed in Section 4.1. The video and load data, which details the failure behaviour of each test, are then presented in Section 4.2. Finally, the temperature data measured in the air, water and ice blocks are given in Section 4.3.

4.1 Test matrix

A total of nineteen (19) ice rubble tests were conducted under this test program that were classified into four different phases (see Table 4.1). In Phase I, special attention was given to understanding the effects consolidation time had on the strength and failure behavior of a freshwater ice rubble beam. The consolidation time was varied between 0.2 hours to 70.5 hours, where the shortest consolidation time was governed by how quickly a test could be setup. In Phase II, the effects of pressure were investigated by confining the ice rubble beam between two platens during the consolidation period. The confinement was set at values between $0kPa$ to $40kPa$. In Phase III, initial investigations into the effects of sintering carried out, and in Phase IV one test was done with smaller ice blocks. In all tests (with the exception of the sintering tests – Phase III), the initial temperature of the ice blocks was held constant at $-18°C$, whereas in the sintering tests, the target ice block temperature was $0°C$. This was done to investigate the effects of sintering without the influence of heat transfer processes influencing freeze bonding. An additional eight (8) shakedown tests were also conducted in the process of determining the best testing setup and methodology, which are given in Appendix C.

Table 4.1. Test matrix

	Test number	Pressure confinement (*kPa*)	Initial ice temperature (°C)	Consolidation time (hrs)	Block size
Phase I	Test 1	0	-18	0.2	Same as DIRKS (Length 30-40*cm*; Width 20-30*cm*)
	Test 2			2.4	
	Test 3			4.2	
	Test 4			4.4	
	Test 5			10.1	
	Test 6			28.5	
	Test 7			70.5	
Phase II	Test 8	0	-18	3.96	
	Test 9	10		4.18	
	Test 10	10		4.05	
	Test 11	25		4.17	
	Test 12	25		3.48	
	Test 13	40		4.2	
	Test 14	40		3.89	
Phase III	Test 15	0	0	0.3	
	Test 16			25	
	Test 17			66.2	
	Test 18			139.7 (6days)	
Phase IV	Test 19	0	-18	4.2	Small Blocks (Length, 20-30*cm*; Width 10-20*cm*)

4.2 Video and Load Data

4.2.1 Effects of consolidation time (Phase I)

In Phase I, seven (7) tests were carried out to investigate the effects of pressure confinement on the ice rubble beam's strength and failure behavior.

For Test 1, analysis of the video and load data from the test carried out after 0.2 hours of consolidation (see Figure 4.1) showed that a shear plug failure took place on the macroscopic scale, where the central part of beam was punched through, while the non-loaded portion of the beam remained in place. Failure of the shear plug was

progressive, where the first failure took place to the right of the platen at 52*mm* of displacement, followed by a second failure to the left of the platen at 85*mm* of displacement. The load trace from the friction test showed that no load drops were observed, demonstrating that the loads were associated with frictional forces and not bond failure, as was expected. It is interesting to note that the forces measured during the friction test are relatively close in magnitude to those measured during the punch test, which is not unexpected as minimal bonds would have formed between the ice pieces for zero consolidation time. The load drops observed during the punch test are likely due to a combination of interlocking between ice blocks or potentially some initial FBs that may have formed in the time it took to setup and run the test.

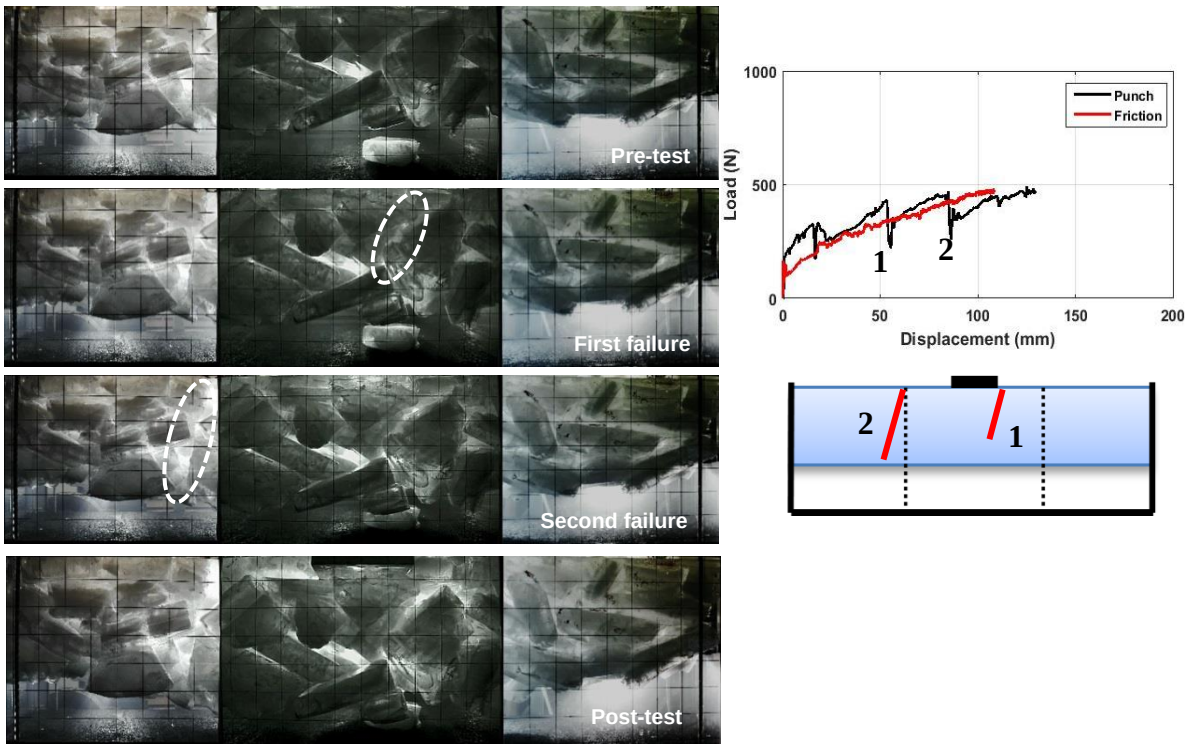

Figure 4.1. Analysis of video and load data from the 0.2 hours consolidation test (Test 1)

By comparison, the failure behaviour observed in the test conducted after 70.5 hours of consolidation (Test 7) was noticeably different from that done at 0.2 hours, where the beam failed in bending in macroscopic scale as opposed to shearing; see Figure 4.2. The load trace measured during this punch test showed that the beam failed in a single event that occurred at 65*mm* of displacement. The failure plane was located slightly to the left of the platen, as opposed to the center which would be expected for a homogenous beam. This is not unexpected as the distribution of ice blocks in the rubble beam is random, resulting in a non-uniform stress distribution. The loads measured in the friction test for this case were significantly lower than those measured during the punch test, especially at peak load. This is because the rubble beam was heavily bonded during the punch test, which increased the strength of the beam, whereas in the friction test, the bonds along the failure plane had already been broken.

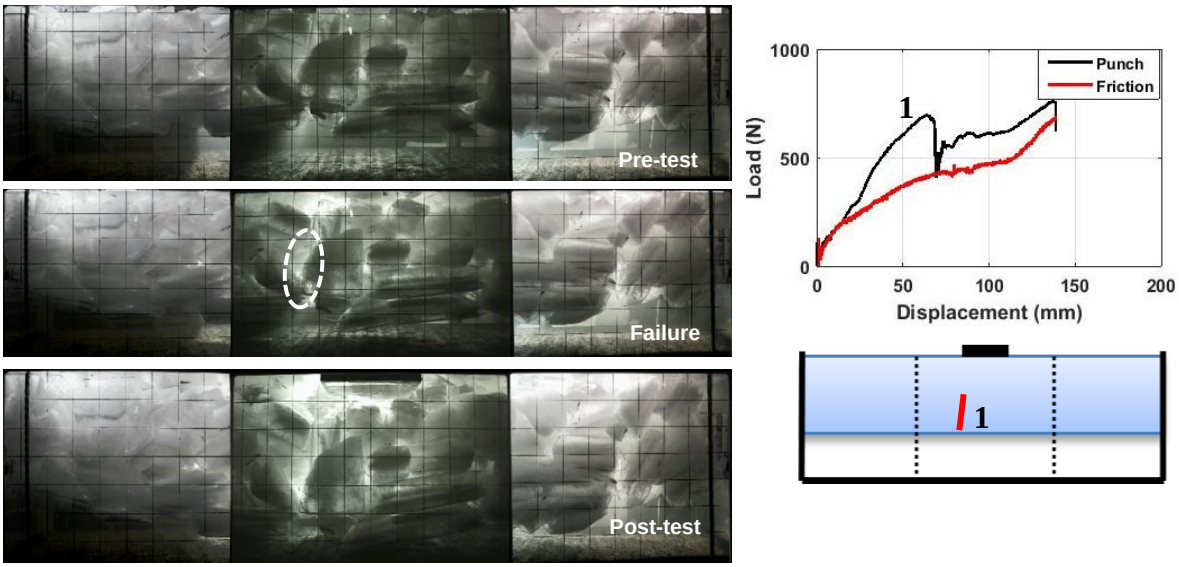

Figure 4.2. Analysis of video and load data from the 70.5 hours consolidation test (Test 7)

Figure 4.3 shows the load-displacement plots for all test cases considered in Phase I, covering the full range of consolidation times tested, as well as a schematic showing the observed macroscopic failure behaviour of the beam. Note that for Test 3 (4.2 hours) no schematic is given as one of the cameras malfunctioned and the failure area could not be determined. For consolidation times of less than 4 hours, the beam failed progressively in shear, where there were typically two large load drops observed before plug failure. For these shorter submersion times, since the bonds are expected to be weaker, a progressive sequence of block-block failures characteristic for macroscopic shear failure is more likely, which is analogous to shearing of a cohesive granular material. After 4 hours of consolidation the deformation behaviour appeared to change to bending or a combination of bending and shearing, where the non-loaded portion of the beam also was displaced and only a single load drop resulted in the failure of the beam. This behaviour may be attributed to increasing bond strength, which causes the rubble matrix to take on the behaviour of a brittle porous solid, in which higher stresses can be transmitted throughout the matrix resulting in macroscopic beam-like behaviour characterized by flexural failure. In addition, bond strengths may become more homogeneous over time, making progressive failure less likely. The peak load at failure increased with consolidation time from 460*N* in the 0.2 hours test to 1400*N* in the 4.4 hours test, after which, it reduced to 700*N* after 28.5 hours of submersion. It is interesting that the 4.2 hours test was much lower than the 4.4 hours test (Test 3 and Test 4 in Table 1), which was a repeat test. This may be possibly due to differences in setup times (where ice may have warmed up), differences in the distribution of the blocks between the two tests, or other potential

variations, such as random distributions of FB strength in the matrix relative to the point of greatest stress, which triggers the onset of failure.

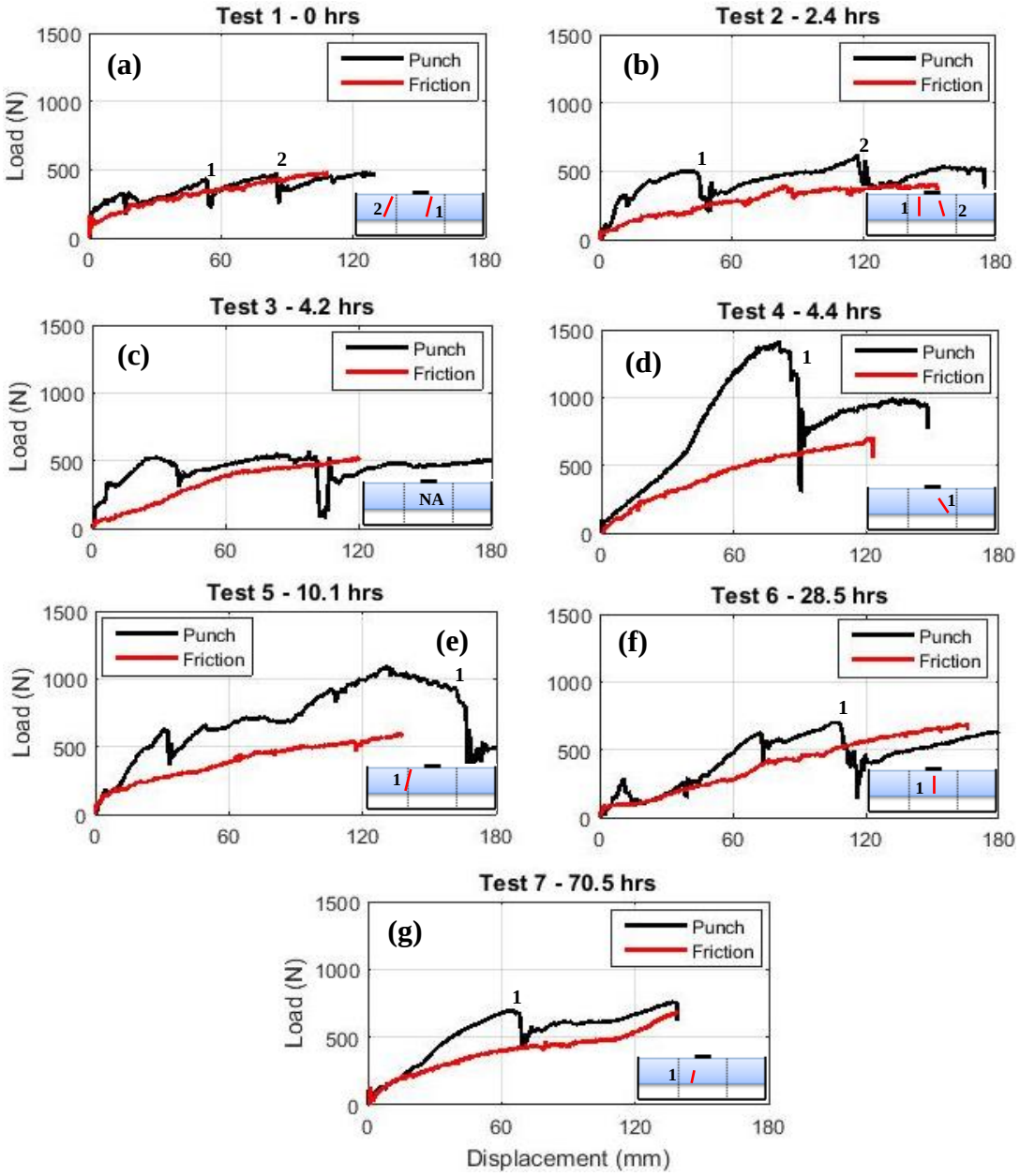

Figure 4.3. Force-displacement plots for the different consolidation times (Phase I)

4.2.2 Effects of Pressure Confinement (Phase II)

In Phase II, the effects of pressure confinement on the ice rubble beam strength and failure behavior were investigated. Seven (7) tests were done in total, three of which were repeats (see Table 4.1).

Prior to commencing with the full test program, in this series some initial shakedown tests were carried out. In the first confinement test that was attempted (shakedown Test 6 in Appendix C), the top plate was pushed down until a pressure of almost $10kPa$ was reached, after which no more load was applied for the duration of the consolidation period (4 hours). Figure 4.4a shows that the confinement pressure plotted against time, where 0 seconds is when the ice rubble beam fabrication was complete. The figure shows the load dropped off exponentially over the course of the consolidation period, reaching less than $1kPa$ after 4 hours (240 minutes). This drop in load was caused largely by rearrangement of the rubble, causing it to be more compacted, such that once displacement of the top confinement plate stopped the load dropped off quickly. It is also possible that localized crushing, creeping and pressure melting could have taken place at contact points between blocks and at the confinement plates. The load measured during this punch test peaked at $860N$ (Figure 4b), which is similar in magnitude to the load measured during the $0kPa$ punch test under the same conditions (see Figure 4.7a). On this basis it was determined that pressure applied during this short period of time had very little effect on the strength of the ice rubble beam. As a result, it was decided that for the remainder of the pressure confinement tests, the confining load was to be manually kept constant for the remainder of the tests.

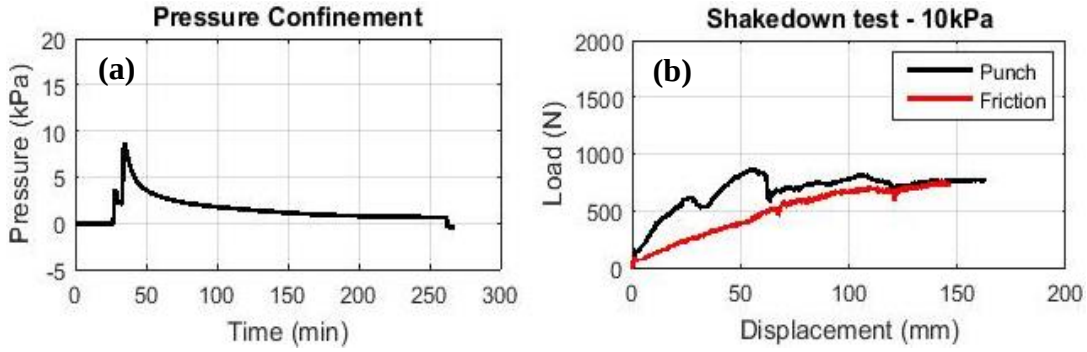

Figure 4.4. The history of (a) pressure vs. consolidation time, and (b) load-displacement for shakedown Test 6

Analysis of the video data such as that shown in Figure 4.5 from the confinement tests, indicated that the failure behaviour in Phase II tests was predominantly bending, where the non-loaded portion of the ice beam was also displaced during the test. In contrast to observations from Phase I, during the pressure confinement tests bending failure occurred as both single events and progressive failure events on the macroscopic scale. Figure 4.5 shows the ice beam failure for Test 12, where the confinement pressure was 25*kPa*. In this test, only one failure occurred, which started to the right of the platen and propagated to the bottom of the beam ending near the bracket. It is also evident when comparing the pre-test and post-test images that the bottom on the beam was opening in tension; however, this failure was not associated with any load drop (this is discussed in more detail in Chapter 6). The load-displacement plot shows that the peak load occurred at about 40*mm*. The increase in load observed after failure is due to buoyancy, which continued to increase until the majority of the beam was submerged. The load recorded during this punch test was significantly higher than the load recorded in the friction test. This is because as previously mentioned, most of the bonds would have failed during the punch test.

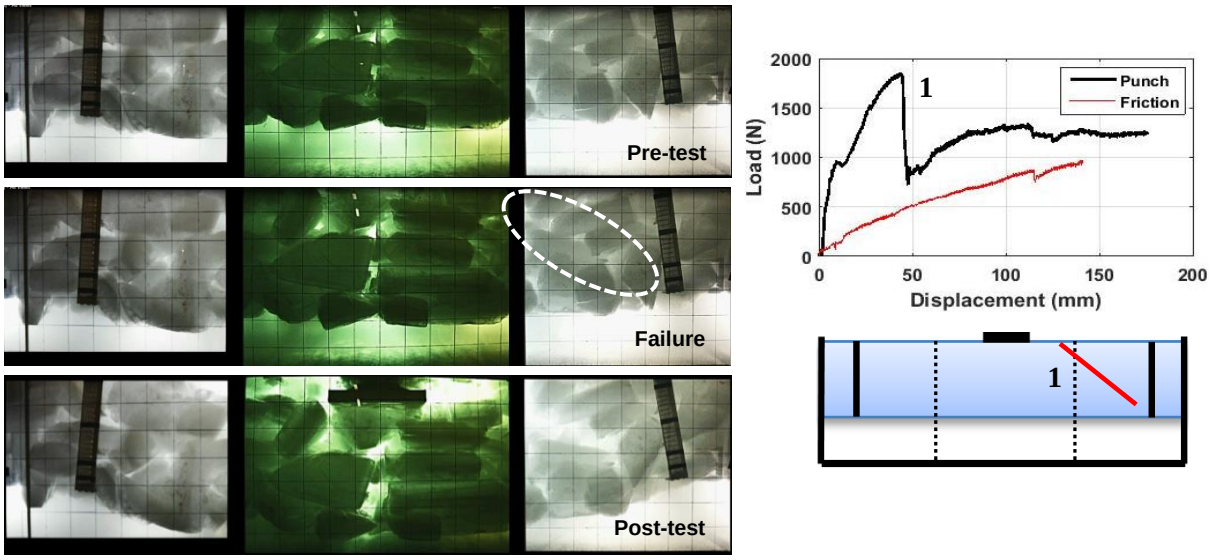

Figure 4.5. Analysis of video and load data from Test 12 with about 4hrs consolidation and 25*kPa* confinement

Figure 4.6 shows the ice beam failure behaviour and load curves for Test 13, where the confinement pressure was 40*kPa*. Similar to Test 12, the beam failed in bending where the non-loaded portion of the ice beam was also submerged. The failure behaviour was, however, progressive where the ice beam failed at 55*mm*, 80*mm* and 130*mm* at loads of 4000*N*, 3300*N* and 1600*N*, respectively. The first failure occurred at the central bottom region of the beam at 55*mm*, followed by the second failure at the left side of the beam at 80*cm* deformation. The third failure took place to slightly at the left side of the beam between the first failure and the second failure and appeared to be more like a locking failure.

Examining the plots for this test, it may be observed that there is a 600N load difference between the punch and friction test at this point, which suggests that this failure may be due to a combination of FB and locking failure.

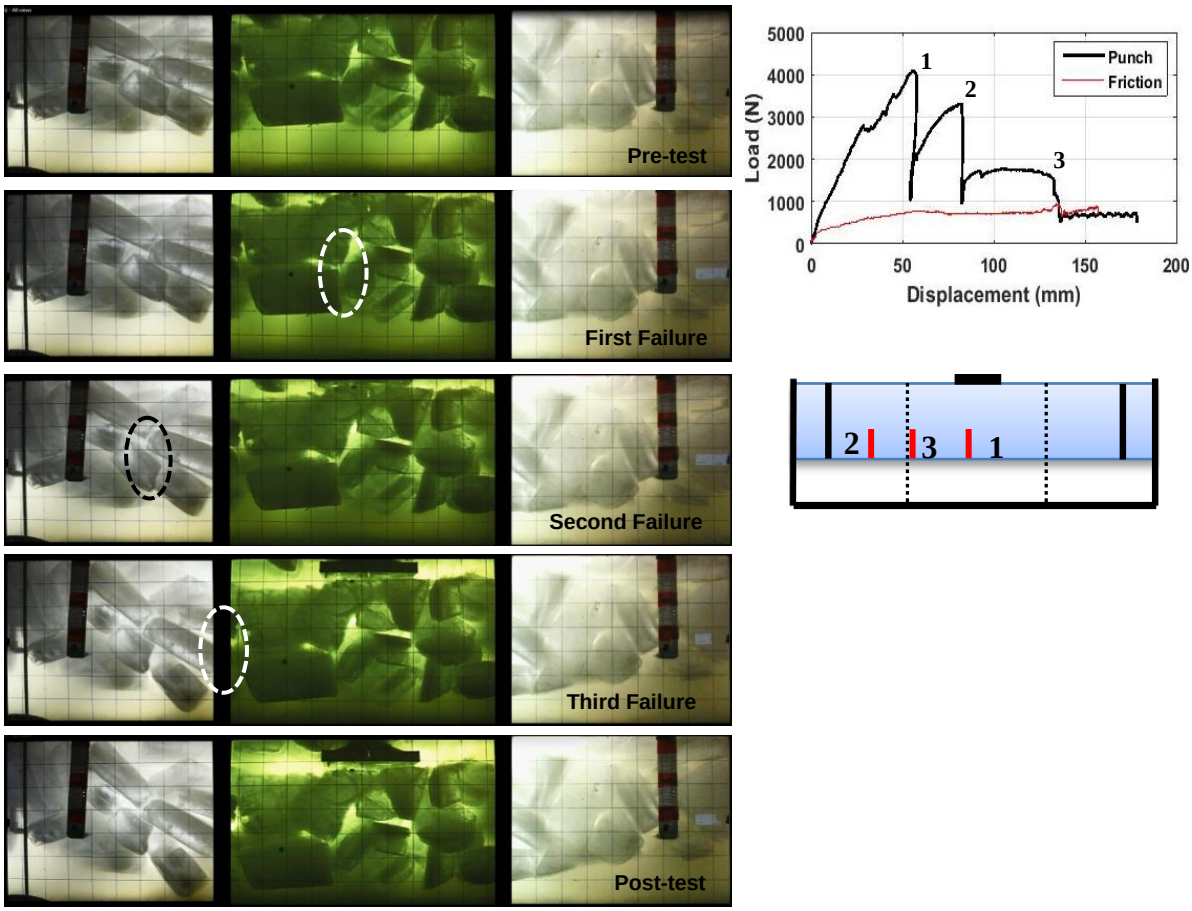

Figure 4.6. Analysis of video and load data from Test 13 with about 4 hours consolidation and 40*kPa* confinement

Figure 4.7 shows the load-displacement plots for the full range of confinement pressures tested in Phase II (0, 10, 25 and 40*kPa*), along with a schematic showing the observed macroscopic failure behaviour of the beam. Also included in this figure are the time histories of confinement pressures applied over the 4 hours consolidation period. Note that once the ice rubble beam was fabricated it took about 30 to 50 minutes to install the top confinement plate, which meant that no confinement was applied during this period (hence the zero load at the start of the plot). In Test 12 the setup took 75 minutes, which may have influenced results. The load traces from the punch tests clearly show that by

increasing the confinement from 0*kPa* to 40*kPa*, the peak loads increased considerably from 800*N* for 0*kPa* confining pressure (Test 8) to a maximum of 4000*N* for a confining pressure of 40kPa (Test 14). For repeat tests, the peak loads recorded during the punch tests with a 10*kPa* confining pressure were fairly consistent. For the 25*kPa* and 40*kPa* tests, repeat experiments produced a variance in peak strength of about 1000*N* for both pressure ranges. The variability in the 25*kPa* test may have been influenced by the 75 minute delay in the application of the surcharge load during Test 12, but given the similar level of variance in the 40*kPa* tests, this may just be due to the innate variability of each ice rubble beam.

The loads measured during the friction tests where confinement was applied (Test 9 to Test 14) increased almost linearly with displacement, reaching a maximum of about 1000*N* at full ram stroke. By comparison when tested at zero confinement under the same conditions (Test 8) the load only reached 550*N*. This increase in frictional load with confinement is likely caused by a greater ice-ice contact as the beam was more compacted. This is discussed in further detail in Chapter 6.

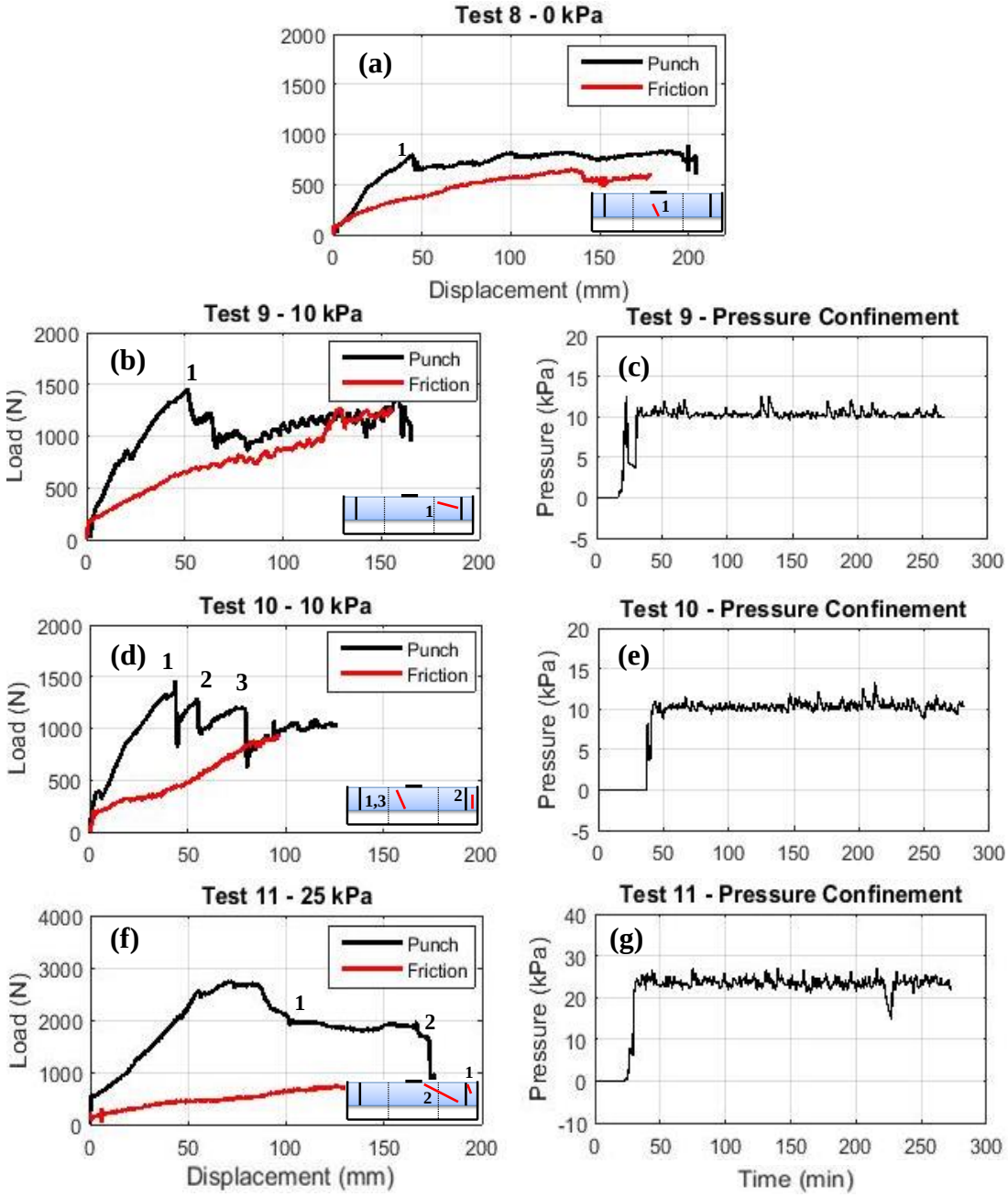

[Continued on page 80]

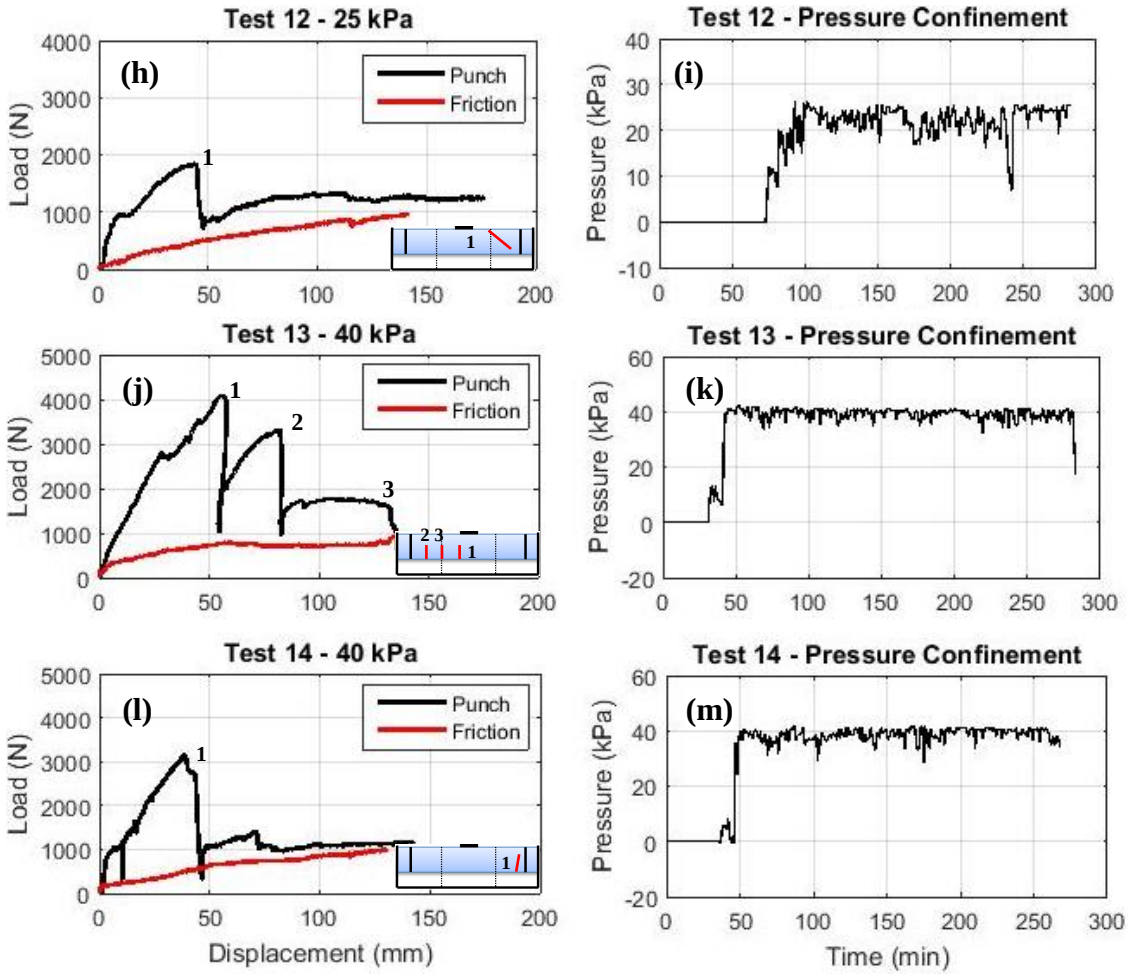

Figure 4.7. load-displacement and the history of consolidation time (Phase II)

4.2.3 Effects of Sintering (Phase III)

In Phase III, four (4) tests were carried out to investigate the effects of sintering on the strength and failure behavior of an ice beam. As sintering is thought to be a relatively slow process (especially in the absence of an external pressure) the consolidation time was varied from 0.3 hours to 139.7 hours (6 days). The 0.3 hours (20 minutes) sintering test was carried out so that comparisons could be made between the '0 hours' test completed during the consolidation (Phase I) tests, where the initial temperature of the ice was -18°*C*.

Analysis of the video data from the sintering tests showed that the dominant mode of failure during the Phase III tests was shearing, where the non-loaded portion of the ice beam remained in place while a plug was pushed out the bottom of the beam. Figure 4.8 shows the beam deformation for Test 18 where the consolidation time was 139.7 hours. A small drop in load was observed at 75*mm* of displacement, in which a trapezoidal shaped plug of rubble was progressively pushed out the bottom of the beam, concurrent with shear failure.

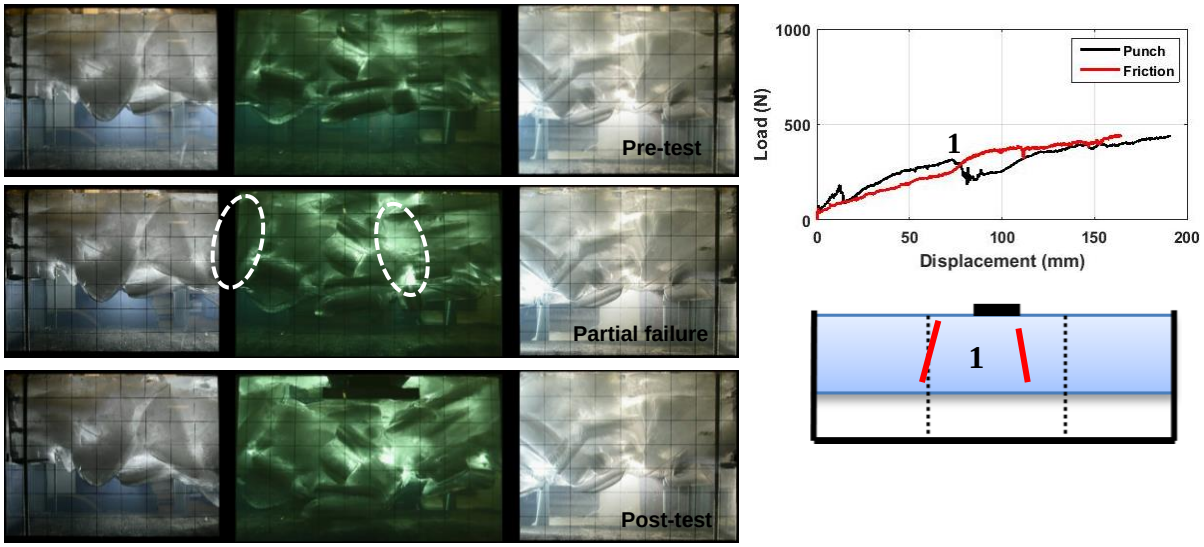

Figure 4.8. Analysis of video and load data from Test 18 with about 6 days (139.7 hours) consolidation time with 0℃ initial ice blocks temperature

Figure 4.9 illustrates the punch and friction load-displacement curves for the sintering tests, as well the observed macroscopic failure behaviour of the beam. In the 0.3 hours sintering test (Test 15), no load drops were observed in the punch test signifying that no bonds had formed between the ice blocks or the bonds had minimal strength and there was minimal interlocking between blocks. Moreover, the load measured during this

punch test was actually lower than that measured in the friction test. The reduced load in the punch test occurred because the displaced plug did not returned fully to its original position meaning that the hydraulic ram has to start at a lower position in the water which could have increased the buoyancy force and in turn the frictional load (as was observed in the video).

For the higher consolidation times, the punch and friction loads were either the same (Test 18) or the punch load was slightly higher than the friction load (Test 16 and Test 17). The reason the punch loads were slightly higher in Test 16 and Test 17 was because the cold room temperature was set to -1°*C* (rather than 0°*C* as was done in consolidation time tests, Phase I). This resulted in the formation of a thin, 0.5*mm* to 1*mm*, consolidated layer, which was cut through prior to testing. The reason the temperature was reduced to -1°*C* was because in Test 18 inspection of the rubble after the test revealed that localized melting had taken place at the outer surfaces of the blocks (see Figure 4.10a). Despite the observed melting at the outer surfaces, bonding was observed at the contact points between selected ice blocks (see Figure 4.10b). It is noted that the large drop in load at 100*mm* displacement during Test 17 was caused by human error, when the hydraulic displacement was temporarily stopped.

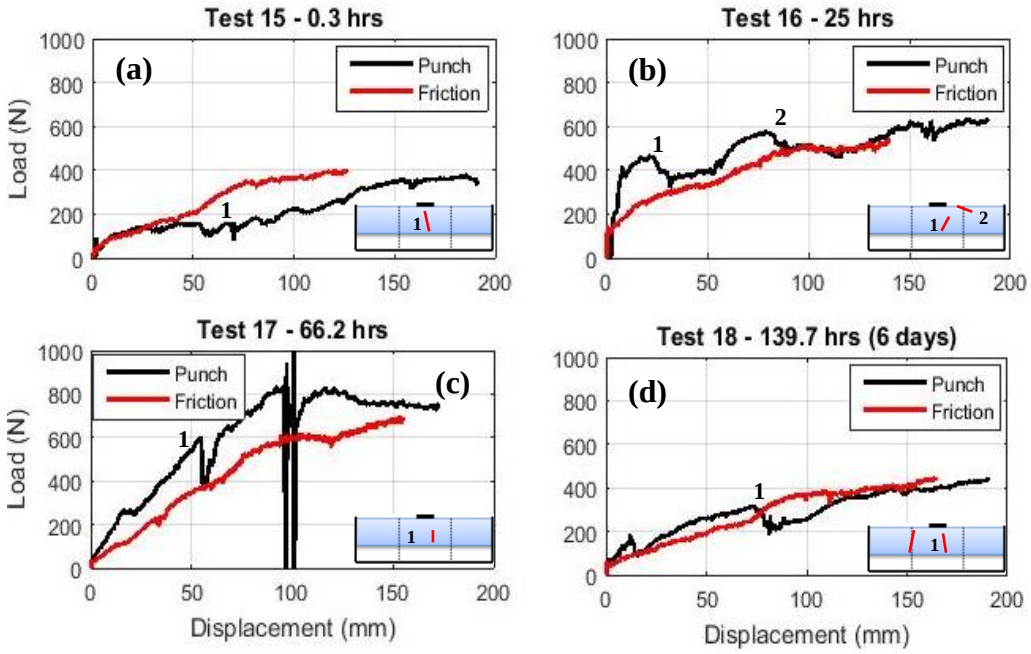

Figure 4.9. Punch and friction load for sintering tests

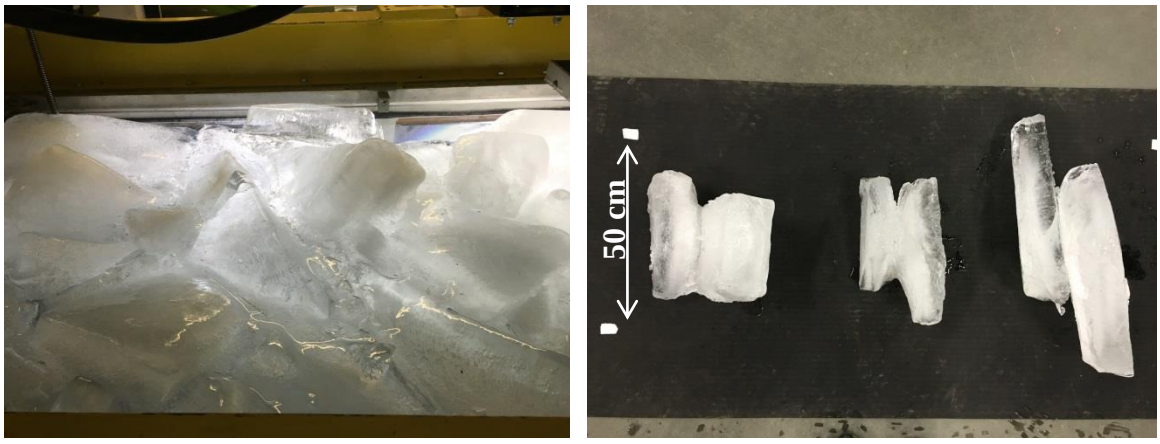

(a) **(b)**

Figure 4.10. Photographs of: (a) Melting ice blocks at the outer surface and; (b) FB formation in Test 18

4.2.4 Effects of ice blocks dimensions (Phase IV)

In Phase IV, the effects ice block dimensions on the strength and failure behavior of an ice rubble beam was investigated. For this one test (Test 19) was carried out with smaller

ice blocks that were of length 20*cm* to 30*cm* and width 10*cm* to 20*cm* (compared with length 30*cm* to 40*cm* and width 20*cm* to 30*cm* which was used for rest of the tests – see Section 3.2.1 for more details on block dimensions). In this test the thickness of the beam and consolidation time were kept constant at 50*cm* and 4.2 hours so that comparisons could be made with previous tests. The mass of ice that was needed to make the 50*cm* thick beam was 1136*kg* (compared with 750*kg* in previous tests) resulting in a lower porosity beam.

Analysis of the video and load data from the small block test (see Figure 4.11), showed that the beam failed in a combination of shearing and bending. One failure occurred at the right hand side of the platen at 130*mm* of displacement, which caused the non-loaded portion on the right of the beam to remain in place, indicative of shear type failure. Conversely, on the left hand side of the beam, both the loaded and non-loaded portion was submerged, indicative of bending failure. It is possible that with increased displacement, a second shear plane to the left might have developed as was observed during the Phase I (consolidation time tests). However, unfortunately there was not enough room in the box or stroke on the ram to push further. It is interesting to note that the total ram displacement was 230*mm*, which was greater than all other tests perhaps because as the beam failed the displaced blocks compacted more readily than the big blocks or/and the initial beam geometry was more consistent.

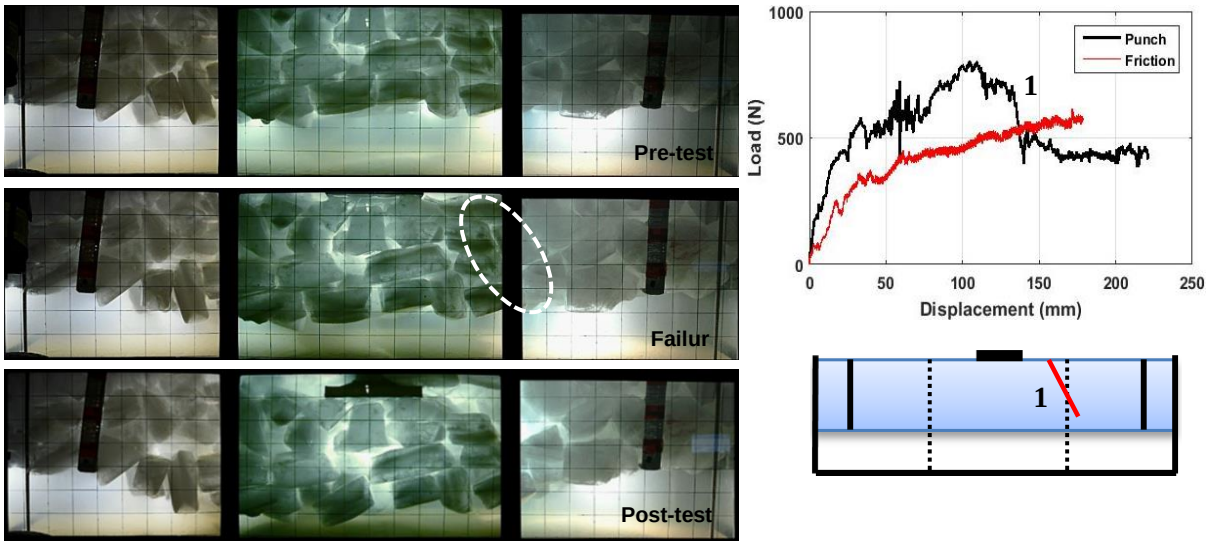

Figure 4.11. Analysis of video and load data from Test 19 with small ice blocks

4.3 Temperature Data

In this section, the temperatures measured in the water, air and ice blocks are presented. The section is subdivided by test phase (Phase I to IV), since each phase had different setups which may have influenced the temperature histories. In each section, data from a selected test is presented which show the nominal behaviour observed in that phase. Temperature data for each individual test is given in Appendix D.

4.3.1 Temperature data for consolidation time tests (Phase I)

For the Phase I temperature analysis, Test 9 has been taken as the representative case (see Table 4.1 for details). Figure 4.12 shows the positions and dimensions of the ice blocks containing Micro-Ts for Test 6, as well as the positions of RTDs. In general one ‘large’ and one ‘small’ ice block was positioned at each depth in the beam as it was expected that the ice block size as well as its position will influence the rate of heat transfer. The annotation for the blocks was as follows: the numbers denote the depth, where 1, 2 and 3

are the top, middle and bottom of the beam, respectively, and the letters denote the location at each depth where A was in the centre and B at the edge of the beam. The volume of the ice blocks in this test varied from 7103cm^3 to 20262cm^3.

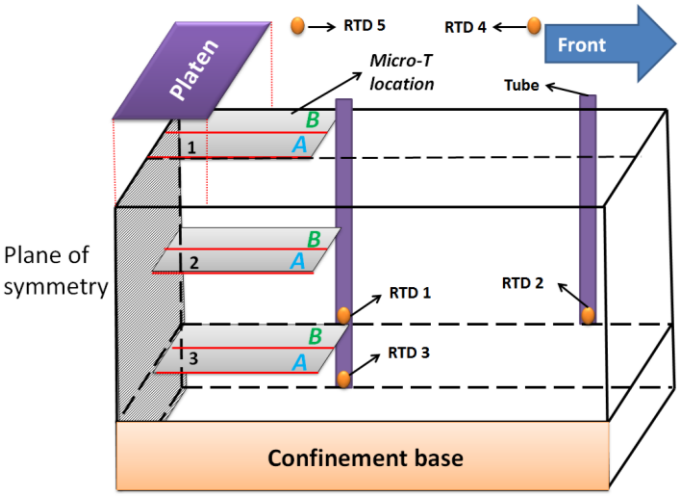

Location	Maximum length (cm)	Volume (cm^3)
1A	33	7103
1B	36	9304
2A	40	11833
2B	38	10379
3A	40	7206
3B	58	20262

Figure 4.12. Position and dimensions of the ice blocks containing Micro-Ts for Test 6

The Micro-T temperature data presented in Figure 4.13 shows the temperature history of the ice blocks from Test 6. The letters *A*, *B*, *C* and *D* on top of the graph denote, respectively, the time at which the ice blocks left the container (*A*), the time the Micro-T ice blocks were positioned in the punch box (*B*), the time the confinement plate was lowered (*C*) and the time the ice blocks reached thermal equilibrium (*D*)[3]. Figure 4.13 illustrates that from (*A*) to (*B*), the ice warmed by one degree from -18.4°*C* to -17.4°*C*. As expected, these results reveal that warming up occurred earlier for ice blocks 3A and 3B, as they were positioned first. This is because when building the beam there was approximately 10*cm* of water directly above the confinement plate and consequently

[3] In this section the time to reach equilibrium temperature is only a rough estimation, this parameter for each ice block is measured accurately in Section 5.4.

these blocks were submerged in water. As heat conductivity in water is higher than that in the air, it is not surprising that blocks 3A and 3B warmed up at a higher rate. In contrast, blocks 1A, 1B, 2A and 2B were not submerged until the confinement plate was dropped (step *C*), after which the temperature increased at a higher rate. Ice block 3A was the first block to reach thermal equilibrium with the surrounding water because it was a 'small' ice block and it was one of the first to be inserted into the water. Overall, it took approximately 100 minutes from the time of submergence (*C*) for the remaining ice blocks to reach equilibrium with the water temperature. After that, the temperature of the ice blocks remained constant, as did the water temperature (see Figure 4.14).

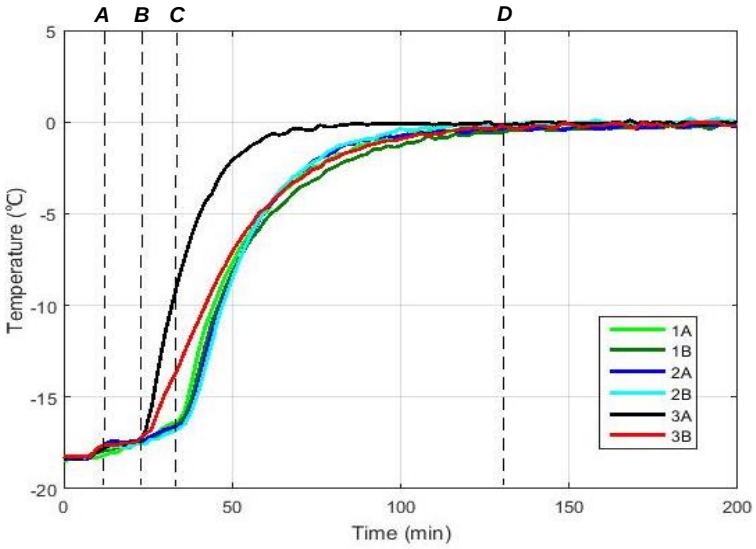

Figure 4.13. The internal temperature of six ice blocks measured by Micro-T sensors for Test 6

Figure 4.14 shows the water and air temperature measured by the RTDs during Test 6. Figure 4.14a illustrates the temperatures measured over the full consolidation period (1713 minutes), while Figure 4.14b illustrates a zoom in of the first 200 minutes so that

comparisons can be made with the Micro-T data. Over the course of the consolidation period, the air temperature nominally fluctuated between 2°*C* and -0.6°*C*. There was, however, occasioned spikes where the air temperature increased above this range because of the cold room defrosting cycle. With the exception of the first 150 minutes, the water temperature remained constant during the entire consolidation period. The temperature measured by RTD 3 (located towards the bottom of the punch box - see Figure 4.12) was 0.8°*C* warmer than that reported by RTD 1 (located just under the rubble beam), indicating that the water was stratified. RTD 2 was marginally colder (0.26°*C*) than RTD 1, as it was located towards the edge of the box. In the first 120 minutes, there were some fluctuations in the water temperature caused by mixing of the stratified water column, as the bottom confinement plate was lifted and dropped when fabricating the ice rubble beam.

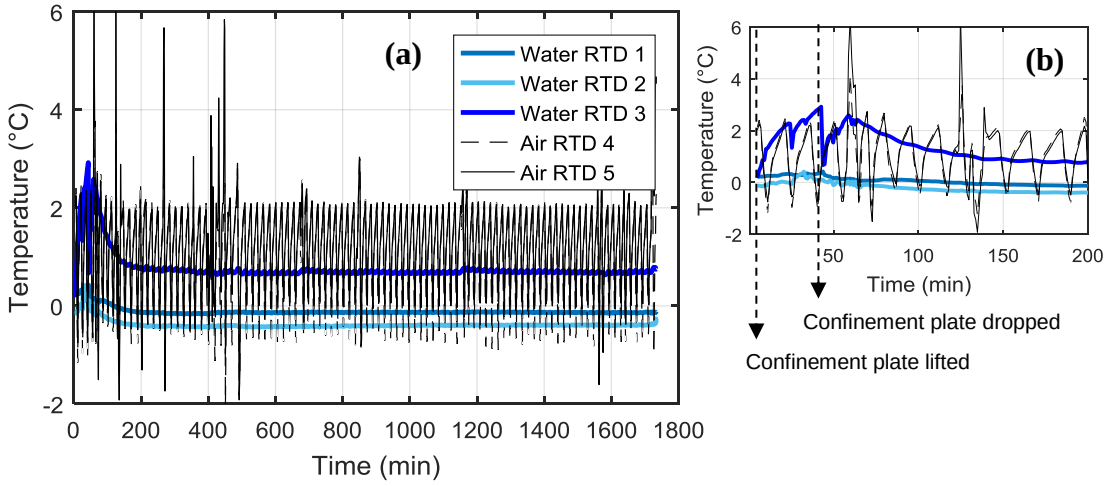

Figure 4.14. Water and air temperatures measured by the RTDs for Test 6 showing (a) entire test; (b) first 200 minutes

4.3.2 Temperature data for pressure confinement tests (Phase II)

For the Phase II temperature analysis, Test 9 has been taken as the representative case (see Table 4.1 for details). Figure 4.15 shows the RTDs and ice blocks' positions for this test, as well as the ice block dimensions. The volume of the ice blocks in this test varied from 4459cm^3 to 16186cm^3.

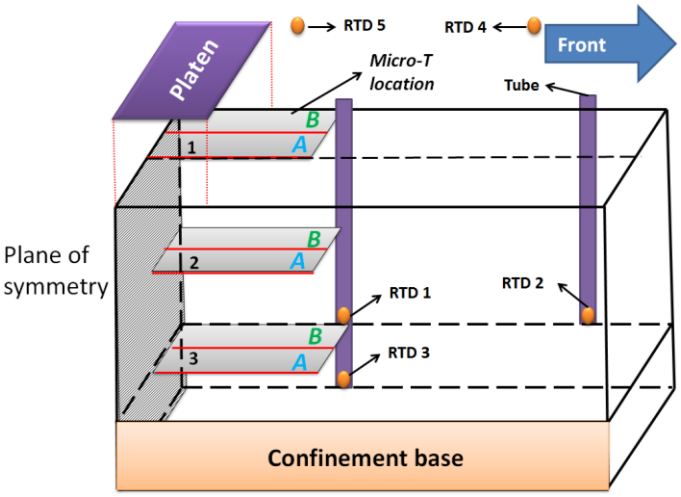

Location	Maximum length (cm)	Volume (cm^3)
1A	37	8802
1B	43	11123
2A	52	12621
2B	34	4459
3A	55	16186
3B	40	4646

Figure 4.15. Position and dimensions of the ice blocks containing Micro-Ts and RTDs for Test 13

Figure 4.16a illustrates the ice block temperatures during Test 13. Similar to Figure 4.13, the letters *A*, *B*, *D* denote, respectively, the time at which the ice blocks left the container (*A*), the time Micro-T ice blocks were positioned in the box (*B*), and the time the ice blocks approximately reached thermal equilibrium (*D*). As described in Section 3.3, for the confinement tests the bottom plate was not lifted to fill the box, as such the time when beam fabrication commenced and was completed are denoted by (e_1) and (e_2), respectively. (*F*) denotes the time at which beam confinement was initiated (i.e. the beam was sandwiched between the bottom and top confinement plates).

From Figure 4.16 it is observed that temperature in the container was -18.3℃. In contrast to Test 6, all ice blocks started to increase in temperature at approximately the same time at (*B*). This is because the bottom confinement plate was not lifted and the rubble beam was submerged. Therefore, all Micro-T blocks had similar ambient conditions. It is also observed that the warming up process in block 2B is faster than other blocks, as the volume of block 2B is smallest (see Figure 4.15). Overall, it took approximately 100 minutes from the time of consolidation (*B*) for the remaining ice blocks to equilibrate to the water temperature.

It is interesting that at the time of beam confinement, the temperature of block 2A dramatically increased and reached the equilibrium temperature. A similar phenomenon was observed in block 3A in Test 10. This is highly likely because of water penetration into the block and reaching the Micro-Ts, as during confinement some ice blocks cracked or were broken into smaller pieces. Therefore, cracking or breaking blocks into smaller pieces causes the area of ice blocks surrounded by water to increase, resulting in higher heat convection. It may be concluded that ice block fragmentation is more probable at the top layer of the ridge due to higher confinement. Therefore, for the case that water temperature is almost constant through the ridge height, the blocks at the top layer may reach the equilibrium temperature faster. In Section 6.3.1, the fragmentation process of an ice rubble beam is described in more detail.

It is noteworthy that for this test, at the time of confinement, the ice block temperatures were between -2.5℃ and -5℃. This means that it is highly likely that the blocks are

bonded before confinement, and at the initiation of confinement they have less cold reservoirs to form FBs. However, as shown in Figure 4.7, the confinement tests had different test setup time, which means that the average initial time of ice blocks may be different in the confinement tests.

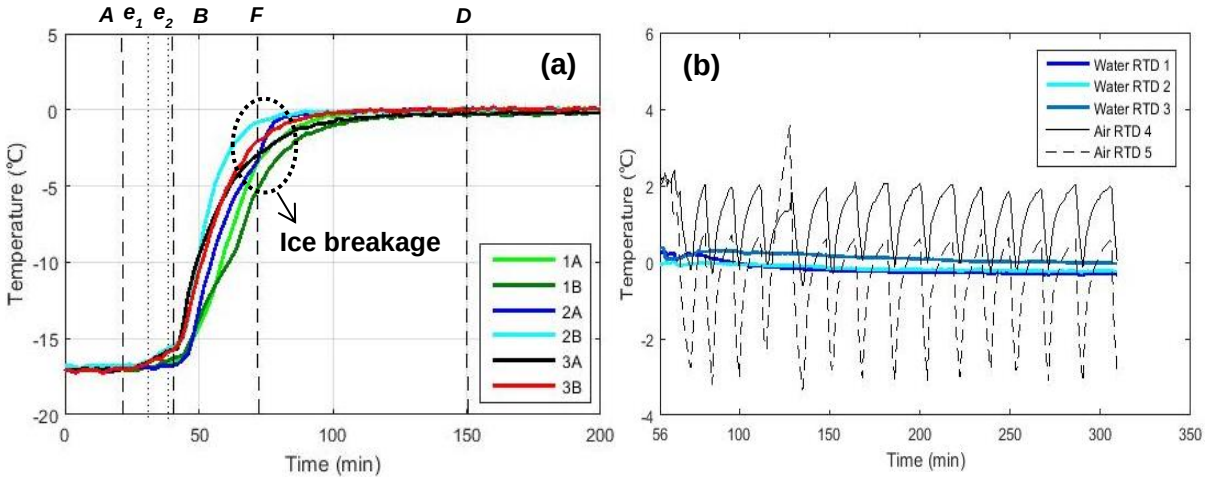

Figure 4.16. Plots showing (a) the internal ice block temperature measured by the Micro-T sensors and (b) the water and air temperatures measured by the RTDs Test 13

Figure 4.16b illustrates the data for air and water temperature in Test 9. Slight changes are observed in the temperature data of RTD 1, 2 and 3 in the first 100 minutes. This is highly likely because of mixing of warm water at the bottom with colder water at the top due to confinement plate movement. The RTD 5 data shows that the Cold Room air temperature fluctuated between 0.6℃ and -3℃. The temperature is lower in this test in comparison to Test 6 because the setting for the Cold Room temperature was set to -1℃ for Test 9. In contrast to RTD 5, the results of RTD 4 show that the Cold Room air temperatures varied between 0℃ and 2℃. This difference is likely due to RTD 4 being positioned near the main door. Since the door was slightly open to accommodate

hydraulic hoses for the confinement apparatus for the beam, the air temperature was higher near the door.

4.3.3 Temperature data for sintering tests (Phase III)

For the Phase III temperature analysis, Test 9 has been taken as the representative case (see Table 4.1 for details). Figure 4.17 shows the RTD and ice block positions, as well as the dimensions of the ice blocks containing Micro-Ts for Test 17. Note that only five Micro-Ts (location 1A was left empty) and four RTDs (RTD 1 malfunctioned) were used in this test. RTD 4 was also positioned at the air-water interface, as opposed to in the air for comparison. The Micro-T ice block maximum length was 33cm to 41cm and the volume was 8567cm^3 to 11700cm^3.

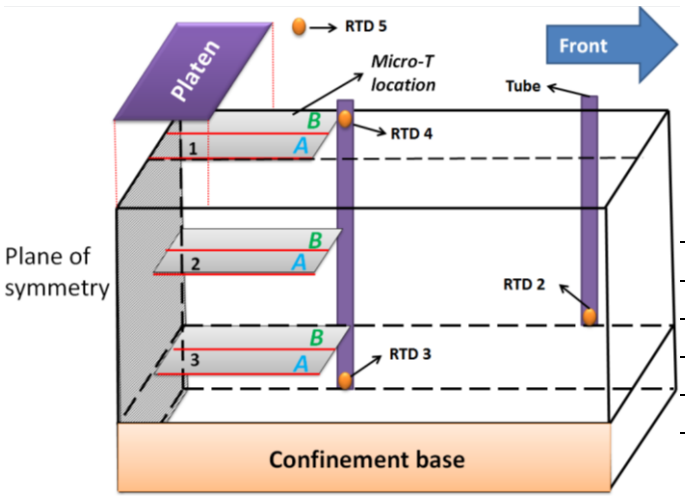

Location	Maximum length (cm)	Volume (cm^3)
1A	-	-
1B	33	8656
2A	41	11700
2B	35	8567
3A	36	9247
3B	36	9166

Figure 4.17. Position and dimensions of the ice blocks containing Micro-Ts and RTDs for Test 17

Figure 4.18a shows the ice block temperature data for Test 17. In comparison to previous tests, a somewhat different trend is observed in the ice block temperatures, since the objective of the test was to illuminate heat transfer processes so that sintering could be

investigated. To do this the container temperature was set to -5℃ and the ice blocks were left to acclimatise for 2 hours (interval between *A* and *B*) at room temperature till they reached a nominal temperature of 0℃. Analysis of the results revealed that while best efforts were made to have zero residual cold reserves the temperature of the ice blocks varied between -0.5℃ and -2.5℃. These differences may be due to the ice block positions in the bags, e.g. block 2A and 2B may have been on top of other blocks, resulting in greater heat transfer from the surrounding air, whereas the other blocks may have been inside the bag. It was observed that after dropping the bottom confinement plate (*C*), the warming up process in blocks 1B, 3A and 3B were faster because of the lower initial temperatures in these blocks. The blocks 2A and 2B did not significantly warm as their temperature at (*C*) was already near the equilibrium temperature.

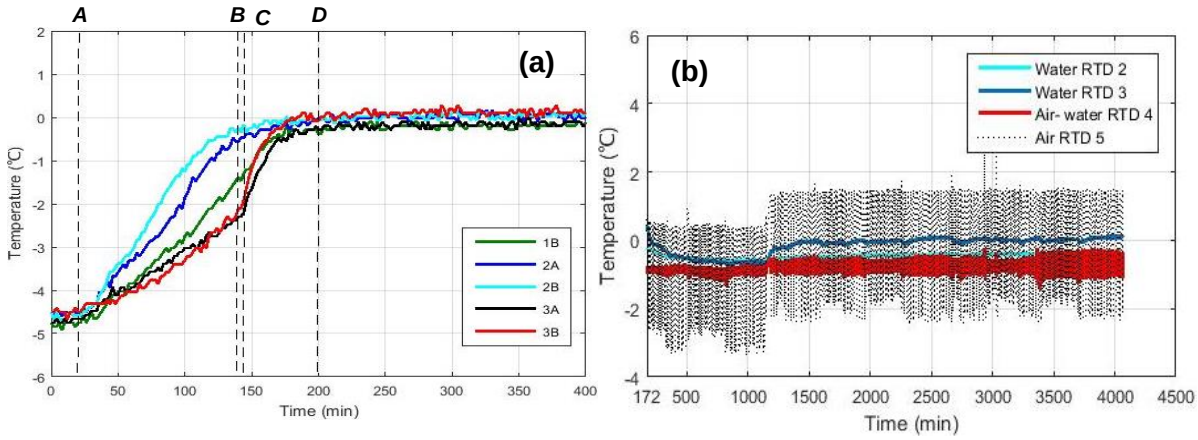

Figure 4.18. Plots showing (a) the internal ice block temperature measured by the Micro-T sensors and (b) the water and air temperatures measured by the RTDs for Test 17

Figure 4.18b shows the data for air and water temperature from Test 17. On the first day of consolidation (0 to 1200 minutes), the cold room temperature was set to -1℃, which

resulted in temperature that varied between 0.5℃ and -3℃. Since a thin consolidated layer formed at the top of the beam, the cold room temperature was adjusted to 0℃ from 1200 minutes onwards. As a consequence, the air temperature range varied between 1.5℃ and -2℃ for the remainder of this test. The change in air temperature at 1200 minutes, had a small effect on RTDs 3 and 4 and no effect on RTD 2, which was attributed to positioning. The temperature fluctuations observed in RTD 4, located at the air-water interface are lower than in the air as the probe got frozen into the consolidated layer.

4.3.4 Temperature data for small ice block tests (Phase IV)

For the Phase IV temperature analysis, Test 19 has been taken as the representative case (see Table 4.1 for details). Figure 4.19 shows the positions and dimensions of ice blocks containing Micro-T, as well as the position of the RTDs. In this test, RTD 4 was also positioned near the top of the rubble beam in the water. As small blocks were used in Test 19, the volume of the ice blocks varied from 3735 to 6926cm^3.

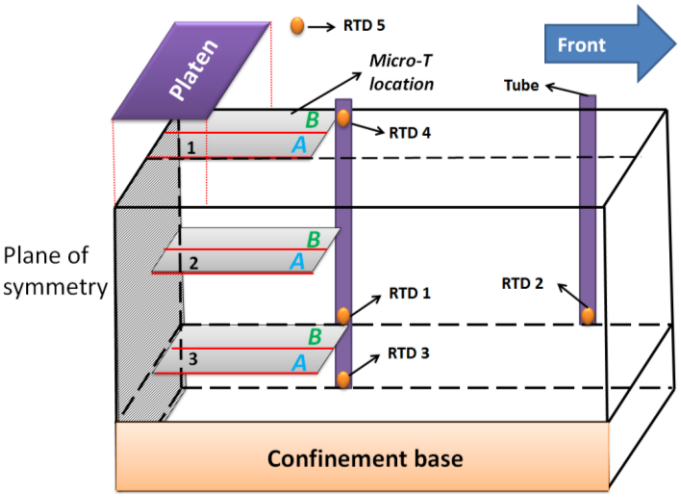

Location	Maximum length (cm)	Volume (cm^3)
1A	24	3998
1B	25	3735
2A	30	4753
2B	27	5658
3A	30	7681
3B	34	6926

Figure 4.19. Position and dimensions of the ice blocks containing Micro-Ts and RTDs for Test 19

Figure 4.20a illustrates the results of the Micro-T ice blocks in Test 19. The ice block temperatures at the time of removal from the container (*A*) was approximately -18℃. At the time of positioning Micro-T ice blocks (*B*), the temperature varied between -16℃ and -17.3℃. It is noteworthy that the process of filling the box in this test was finished in 58 minutes (e_2). As a consequence, some ice blocks, which did not contain Micro-T, may have reached the equilibrium temperature after about 125 minutes (*D*). As the ice blocks are almost of the same dimensions, no significant changes were observed in the rate of the warming.

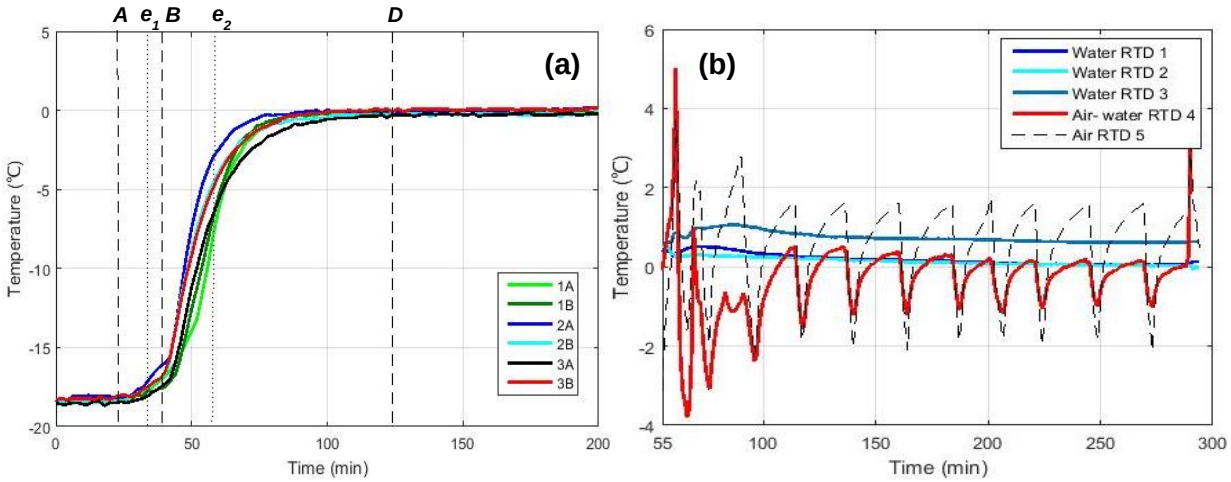

Figure 4.20. Plots showing (a) the internal ice block temperature measured by the Micro-T sensors and (b) the water and air temperatures measured by the RTDs for Test 19

Figure 4.20b shows the air and water temperatures for Test 19. Temperature was only measured once beam preparation was complete (e_2) as such the x-axis initiates at 55 minutes. During this period the air temperature (RTD 5) changed between 1.5℃ and -2℃ and the air-water temperature (RTD 4) between 0.5℃ and -1℃. The high heat capacity of

water resulted in smaller temperature variation at the top of the beam as compared to the measured variation in the air temperature.

The effects of ice block dimensions and positions, as well as the effects of consolidation time, pressure confinement, sintering and smaller ice blocks on the peak load and macroscopic and microscopic failure behavior of ice rubble beam are discussed in more detail in the next chapters.

5 Data Analysis

In this chapter the results from the previous chapter are analyzed to estimate the porosity of ice rubble beam (Section 5.1), the buoyancy force at the time of ice rubble beam failure (Section 5.2), which were in turn used to estimate the strength of the ice rubble beam (Section 5.3). The ice block temperature analysis is then presented in Section 5.4.

5.1 Porosity estimation

Estimating ice rubble and sea ice ridge porosity is important as provides information about the degree of consolidation and compaction between ice blocks. It is also needed to estimate buoyancy, which will be discussed in the following chapter. In this study, porosity refers to the macroscopic porosity of the rubble, which considers the volume of the cavities between ice blocks divided by the ice rubble beam volume.

Two methods were used to estimate ice rubble beam porosity (see Appendix E). In the first method, the change in water level (Δh) and the thickness of the submerged ice beam (H_s) was used to derive porosity (η),

$$\eta = 1 - \frac{h_2 - h_1}{H_s} \tag{5.1}$$

where Δh was determined by measuring the water level before (h_1) and after (h_2) filling the box (see Figure 5.1). This method therefore determines η before the consolidation period.

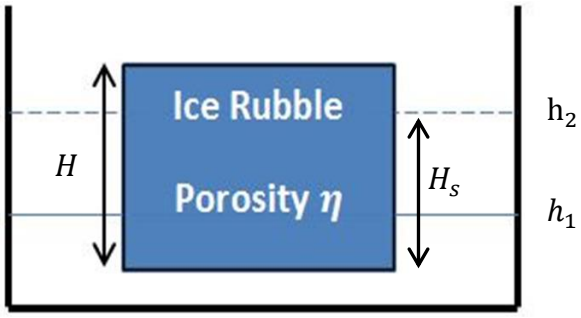

Figure 5.1. The changes of water level from h_1 to h_2 after filling the box by ice rubble

The second method used the total mass (m_{ice}) of the ice rubble beam and its submerged volume (V_s) to derive porosity,

$$\eta = 1 - \frac{m_{ice}}{\rho_w V_s} \tag{5.2}$$

where ρ_w is the density of the water. As mentioned previously in Section 3.3, m_{ice} was 750kg for each test, with the exception of Test 19, where 1136kg of ice was needed to produce the 50cm thick rubble beam using smaller ice block dimensions. V_s was estimated from the video data by measuring the distance from the water level to the bottom of the beam. Since the videos were only setup immediately prior to deforming the beam, Method II therefore gives the porosity after consolidation.

In Table 5.1 the porosity estimated by using Method I and II are given for each test. The results show that the average porosity for the rubble beam prior to consolidation (Method I) was higher than that for after consolidation (Method II) (except in Tests 6 and 7). This is because of FBs' formation during consolidation, which fills the voids between the blocks. In future work it is recommended that the porosity for both methods, before

and after consolidation, would be calculated to find the effects of freeze bonding more precisely.

Table 5.1. Estimated porosity based on Method I and Method II

	Test No.	Porosity (Method I)	Porosity (Method II)
Phase I	T1	-	0.39
	T2	0.37	0.37
	T3	-	-
	T4	0.44	0.39
	T5	0.45	0.44
	T6	0.41	0.42
	T7	0.37	0.38
Phase II	T8	0.42	-
	T9	0.41	0.39
	T10	-	0.4
	T11	-	0.44
	T12	0.43	0.39
	T13	0.48	0.46
	T14	0.48	0.47
Phase III	T15	-	0.4
	T16	-	0.38
	T17	-	0.38
	T18	0.41	0.36
Phase IV	T19	0.39	0.1

For brackish ice conditions, such as the Baltic Sea, Strub-Klein and Sudom (2012) reported keel porosity values on the order of 0.3. The values shown above obtained in this test program (see Table 5.1) are somewhat higher because of removal of small fragments and crushed ice, which resulted in a higher portion of voids between the blocks. As discussed previously, this brash was intentionally removed to allow clearer observation of bonding between individual blocks and their subsequent failure during testing. Inclusion

of brash ice to study its effect on ice rubble strength and failure processes is recommended for future work, but was beyond the scope of this study.

Considering results from both Methods I and II, the porosity of Test 19 was found to yield the lowest porosity. This is because in Test 19, smaller blocks were used, therefore, a higher volume of rubble beam was filled with ice blocks. It was expected that the porosity after consolidation in pressure confinement tests would be less than other tests, since confining the beam reduces the volume of cavities between the blocks.

5.2 Buoyancy force estimation

Estimating the buoyancy force at the time of beam failure is required to find the shear and flexural strength of ice rubble. It should be noted that the platen submersion contributes to the increase of total buoyancy force, which is estimated in this section. It was found that the buoyancy of platen reached approximately $120N$ for full submersion (see Appendix F).

Two methods were employed to estimate the total buoyancy force at the time of beam failure. In the first method, the rise in water level (δ) was used to estimate the buoyancy force (F_B),

$$F_B = \delta w l \rho_w g \ [N] \tag{5.3}$$

where g is gravity and w and l are the width and length of the box, respectively. δ was estimated from the height of the water level before the test (y_0) and at the time of beam failure (y) i.e. $\delta = y - y_0$. In the earlier tests (Phase I, Phase III and Test 10, with the

exception of Test 6), δ was estimated from the pixels in the video data (see Figure 5.2a). In later tests (Phase II and Phase IV), a more refined technique was used to measure the change in water level which involved positioning a ruler in the water and fixing it to the box (see Figure 5.2b). The change in water level was filmed using a camera, which was then synchronized with the load-displacement data through the noise trigger as was the case for the other video data recorded.

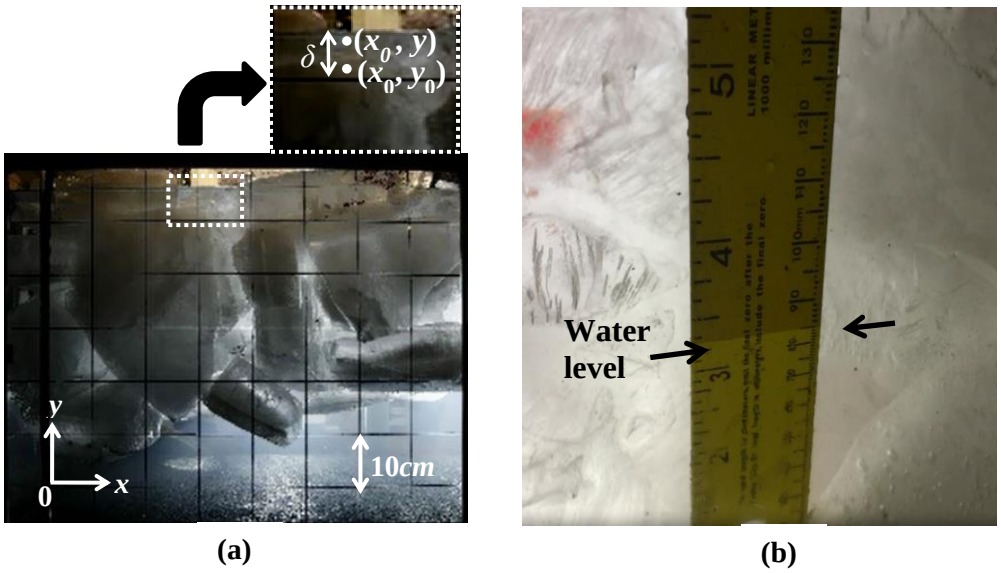

Figure 5.2. Snap shots of the video data showing how the water level displacement (δ) was estimated for the buoyancy force calculations used in Method I, from the pixel in video data (a), by a mounted ruler (b)

In Test 6, the water level was above the viewing panel at the time of beam failure, hence, a second method was employed. As illustrated in Figure 5.3b, in Method II the displacement observed at the underside of the beam was used to estimate the buoyancy force at beam failure. Therefore, the buoyancy force can be derived by Equation (5.4),

$$F_B = (1-\eta)\rho_w g V_b [N] \tag{5.4}$$

where V_b is the nominal volume of the displaced ice beam. V_b was determined from video data, where the position of the underside of the beam pre- and post- failures are shown in solid and dotted lines, respectively (see Figure 5.3). V_b is the product of the area under the length-displacement plot (S in Figure 5.3) and the box width. Note that, this method assumes that the displaced volume at the underside of the beam is equal to the submerged volume at the top of the beam (i.e. no compaction or expansion took place).

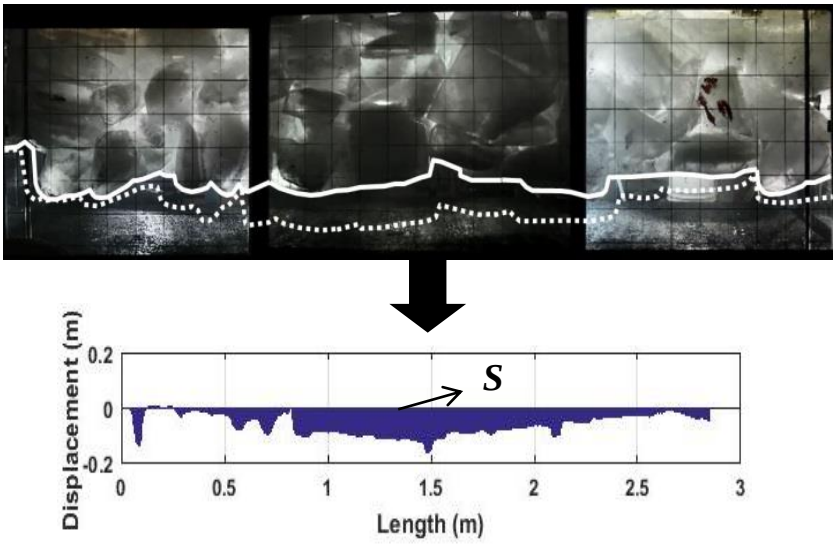

Figure 5.3. Snap shots of the video data showing how the displaced beam volume (V_b) was estimated for the buoyancy force calculations used in Method II

In Table 5.2, the estimated buoyancy force at rubble beam failure is given for each test. In general, the results show that by increasing hydraulic ram displacement the buoyancy force increased. This is because by increasing the rubble beam deformation, larger portions of the beam were submerged in the water, resulting in a buoyancy force increase. However, variation in the buoyancy force-displacement is highly likely due to the blocks'

positioning and beam failure mode, as for example, in beam bending failure, a higher portion of the rubble beam was submerged in water, which consequently increased the buoyancy force.

5.3 Ice rubble beam strength estimation

Due to the different failure modes observed, the data were analyzed both in terms of a shear and bending strength. The shear strength (τ_{shear}) of the rubble beam was estimated using the following equation,

$$\tau_{shear} = \frac{F_{max}}{A} = \frac{F_{peak} - F_B}{A} \; [kPa] \tag{5.5}$$

where A is the failure area and F_{Max} is the maximum net force ($F_{net} = F_H - F_B$) calculated by taking the peak force at failure (F_{peak}) minus the buoyancy force (F_H is the load measured by load cell). For all tests (with the exception of Test 3), A was estimated from the video data by taking the observed failure plane at peak load and extending it over the full thickness and width of the beam (as illustrated in Figures 4.3, 4.7, 4.9 and 4.11). As no video data was recorded in Test 3 a nominal area of $0.47m^2$ was used based on the width and thickness of the beam.

The flexural strength of the beam was estimated using the four-point beam bending equation, as it was observed that at higher beam deflection the load was transmitted to the edges of the platen rather than point loaded in the centre. The flexural strength and effective Young's modulus were derived after Schwarz *et al.* (1981) from the following equations,

$$\sigma_{flexural} = \frac{3F_{max}e}{WH^2}\,[kPa] \tag{5.6}$$

$$E_{eff} = \frac{3}{2W}\left(\frac{1-2e}{H}\right)^3 \frac{e}{1-2e}\frac{(F_{max})}{d}\,[MPa] \tag{5.7}$$

in which, *W* and *H* are the width and thickness of the ice beam, respectively, $e = 1.325$m is the distance from the edge of the platen to the support/friction bracket, and *d* is the corresponding beam deflection.

In Table 5.2 the estimated shear and flexural strength as well as the effective modulus of the ice rubble beam are given for all tests. A discussion of this data analysis will follow in Chapter 6.

Table 5.2. Estimating buoyancy force and shear/flexural strength at the maximum pure load

	Test No.			F_{peak} (N)	F_B (N)	F_{max} (N)	d (mm)	A (mm^2)	τ_{shear} (kPa)	$\sigma_{flexural}$ (kPa)	E_{eff} (MPa)
Phase I	1	Consolidation time (hrs)	0.2	431	290	141	53	0.46	0.31	2.39	0.12
	2		2.4	501	408	93	41	0.43	0.21	1.57	0.1
	3		4.2	522	439	83	29	0.47	0.18 [a]	1.4	0.13
	4		4.4	1414	682	732	81	0.53	1.39	12.4	0.42
	5		10.1	1093	695	398	132	0.51	0.78	6.73	0.14
	6		28.5	704	449[b]	255	106	0.48	0.54	4.31	0.11
	7		70.5	696	504	192	64	0.35	0.55	3.25	0.14
Phase II	8	Pressure Confinement (kPa)	0	799	351	448	44	0.48	0.94	7.57	0.47
	9		10	1457	660	797	51	0.64	1.24	13.5	0.71
	10		10	1460	456	1004	44	0.52	1.95	17	1.06
	11		25	2738	393	2345	74	0.82	2.85[c]	39.7	1.46
	12		25	1856	562	1294	43	0.66	1.97	21.9	1.37
	13		40	4104	140	3964	56	0.45	8.74	67.1	3.28
	14		40	3168	183	2985	38	0.49	6.07	50.5	3.57
Phase III	15	Consolidation time (hrs)	0.3	154	163	0 [d]	53	0.42	-	-	-
	16		25	464	346	118	22	0.47	0.25	2	0.24
	17		66.2	603	357	246	55	0.44	0.56	4.16	0.21
	18		139.7	180	140	40	13	0.42	0.1	0.68	0.15
Phase IV	19		4.2	897	702	195	133	0.52	0.38	3.3	0.07

a) The nominal failure area was used
b) The second method was used to estimate buoyancy force
c) The maximum peak load was selected to be conservative
d) Due to an error in estimating buoyancy force, the net force was negative; since this is non-physical, a value of zero is assumed.

5.4 Ice block temperature analysis

In this section, the temperature data are analyzed to determine the equilibrium time for each individual ice block. This is then used to infer how the positioning of the ice blocks and their volume influences its thermal properties.

Equilibrium time refers to the time it takes for an ice block to reach equilibrium temperature from the time at which it was submerged in the water. In order to estimate

the equilibrium time, the equilibrium temperature should first be defined. It was assumed that an ice block reaches equilibrium temperature when it satisfies the following,

$$\frac{T_0 - T_{eq}}{T_0 - T_a} \geq 0.99 \tag{5.8}$$

in which, T_0 is the initial ice block temperature at the time submersion, T_a is the ambient air temperature which in this study is 0℃, and T_{eq} is the equilibrium temperature. Since the ice blocks did not all have the same T_0 at submersion, there is variance in the equilibrium temperature for each ice block. After estimating the ice blocks' equilibrium temperature, an exponential curve was fit to the temperature data and used to find the equilibrium time.

In Figure 5.4 the equilibrium times are plotted as a function of ice block volume, where Figure 5.4a, b and c show the ice blocks that were positioned at the top, middle and bottom of the beam, respectively. Also, the initial temperatures of ice blocks are given in the legend. Figure 5.4 shows that the volume of the ice blocks varied from 0.3×10^{-4} to $2\times 10^{-4} cm^3$ and the equilibrium time from 50 to 200 minutes, with an average equilibrium time of 95 minutes. Overall data shows that the equilibrium time increases with ice volume, which is as expected as the greater the volume of the ice block the greater the store of negative sensible heat.

The best fit lines show that the slopes were approximately equal for the ice blocks positioned in the middle and bottom of the beam (Figure 5.4b and c), suggesting that the ambient conditions were similar. This suggests that the water stratification observed by

the RTDs located in the water (see Section 4.3), had negligible impact on the heat transfer processes in the rubble. The shallower slope of the best fit line observed for the ice blocks located at the top of the beam (Figure 5.4a) may be because heat transfer processes are slower in air, and since the top side of the blocks would have been exposed to the air this would have increased the equilibrium time.

No relationship was found between the initial temperature of the ice blocks and equilibrium time. This suggests that the difference in initial ice block temperatures was not significant enough to influence heat transfer processes.

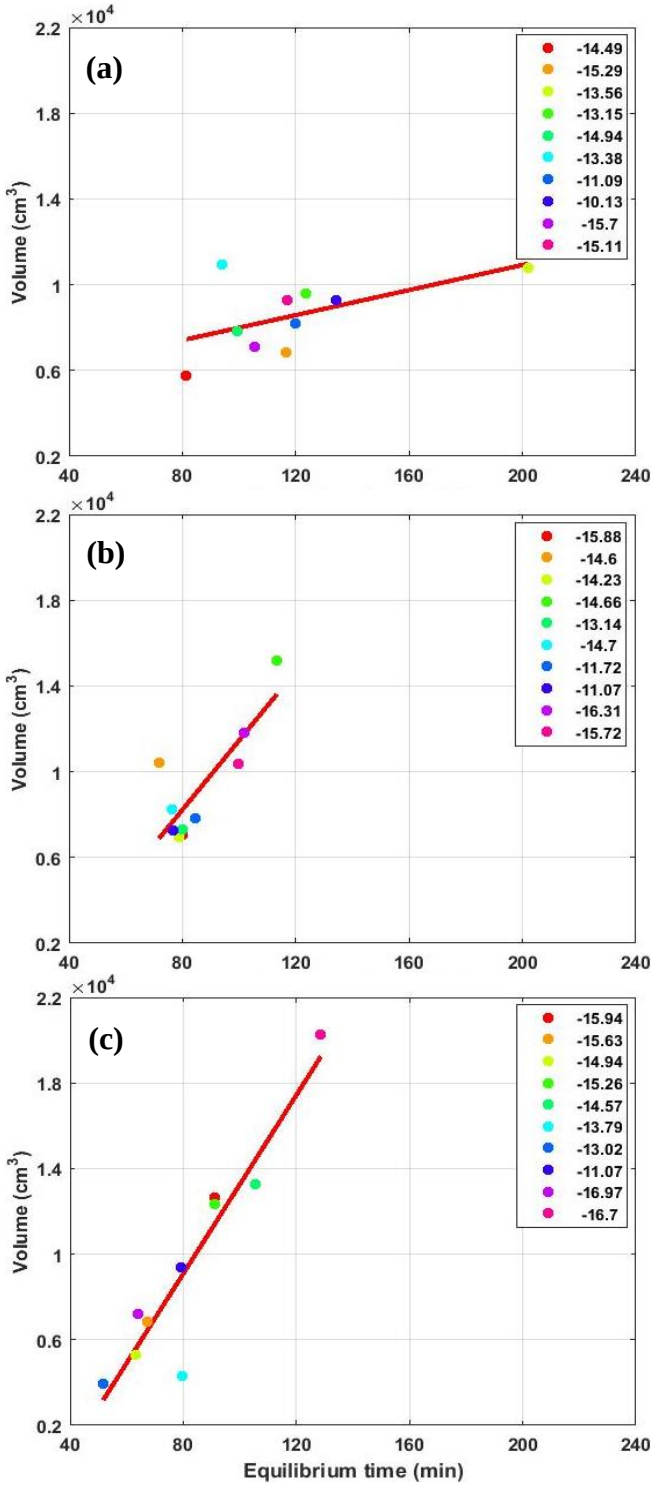

Figure 5.4. Equilibrium time versus volume for ice blocks located at the (a) top, (b) middle, and (c) bottom of the ice rubble beam

6 Discussion

In this chapter, the maximum net force and the strength of rubble beam in the punch and friction tests are compared and analyzed in more detail. In Section 6.1 the results from the punch tests are discussed, once again broken down by test phase. In Section 6.2 the influence of these parameters on forces measured in friction tests are compared. The FB failure behavior of the ice rubble beam is then discussed in more detail in Section 6.3. The effects of sintering and freeze bonding on the strength of the ice rubble beam are discussed in Section 6.4. Finally, the shear and flexural strength as well as the effective Young's modulus of the beam are compared and discussed in Section 6.5.

6.1 Punch tests

6.1.1 Consolidation time tests (Phase I)

Figure 6.1 illustrates the maximum net force ($F_{net} = F_H - F_B$) at the time of beam failure vs. consolidation time for the Phase I rubble tests. The net force gradually decreased from 141N at 0.2 hours consolidation to 83N after 4.2 hours consolidation, after which it jumped to 732N in 4.4 hours. It is observed that after 4.4 hours consolidation, the peak load gradually decreased from 398N to 192N as the consolidation time increased from 10.1 hours to 70.5 hours. It is interesting that the peak load in the 4.2 hour long test was much lower than the 4.4 hours test (Test 3 and Test 4 in Table 5.2), which was essentially a repeat test. This is possibly due to differences in setup times (where ice may have warmed up), differences in the block packing between the tests, or other sources of variability. Additional repeat tests are needed to further explore the source of this discrepancy.

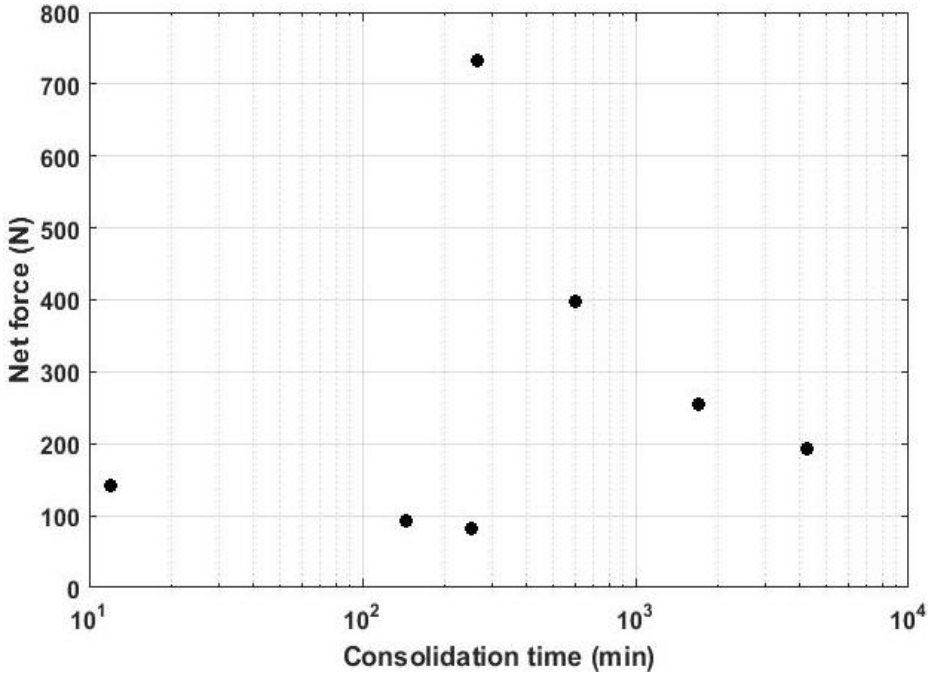

Figure 6.1. Net force vs. consolidation time for consolidation time tests (Phase I)

6.1.2 Pressure Confinement tests (Phase II)

In Figure 6.2a, the net forces measured for Phase II tests are plotted as a function of the confinement pressure, which was applied for a period of 4 hours during consolidation. A linear relationship is evident where the net force increased from 448N to 3964N as the confinement was increased from 0kPa to 40kPa. The repeatability of the results was consistent for 10kPa confinement test, where only a 200N difference is observed in the peak loads. Conversely in the 25kPa and 40kPa tests a difference of approximately 1000N was observed between repeat tests. These differences are likely due to differences in setup time, ice blocks' random positioning, as well as the failure modes of the rubble beam.

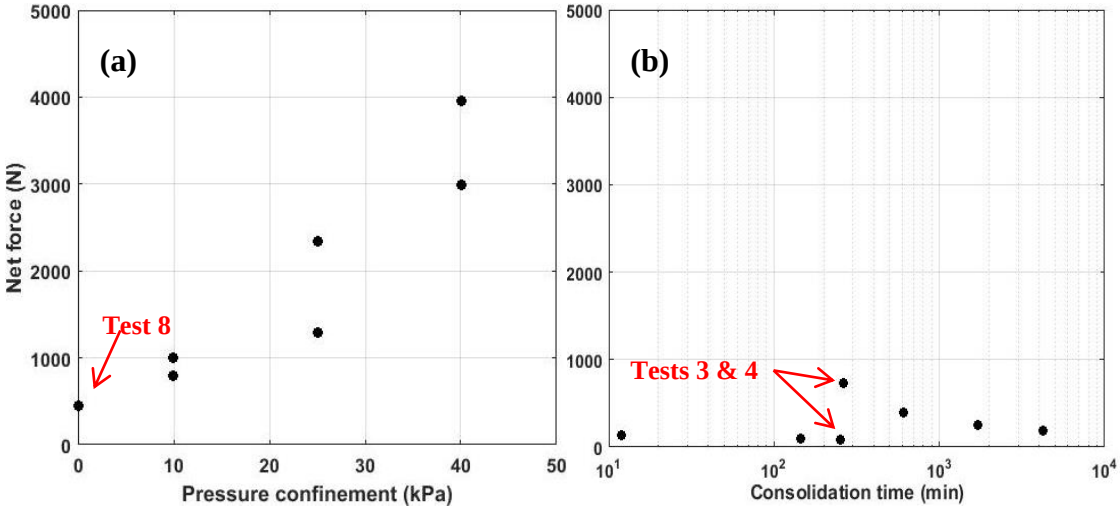

Figure 6.2. (a) Net peak force vs. confinement for pressure confinement tests (Phase II), (b) Net force vs. consolidation time for consolidation time tests (Phase I) where no confinement was applied

The 0*kPa* confinement test (Test 8 in Figure 6.2a) can be compared with the 4 hours consolidation tests (Tests 3 and 4 in Figure 6.2b) that was conducted under Phase I. The only difference being that in Test 8, four more brackets were used to increase the frictional resistance at the end-walls (see Section 3.1.1 for more details). Despite this difference in test setup, the net force for Test 8 was in the same range as Tests 3 and 4, perhaps suggesting that Test 4 is not so much of an outlier.

By comparing Figure 6.2a and b, it can be concluded that, for the range of variables tested, pressure confinement has a greater influence on beam strength than consolidation time. Similarly, the results of FB strength at block-block contact level show that confinement significantly increases the FBs strength (Ettema and Schaefer, 1986; Boroojerdi *et al.*, 2016). The results of pressure confinement tests also support the idea that a strength gradient exists in ice ridges (Timco *et al.*, 2000), as they are more confined

near the water level, and consequently have higher strength at the top. Therefore, one may conclude that during keel-structure interactions, gouging or stamukha formation, the strength of the keel would be expected to significantly increase due to confinement.

The results of pressure confinement tests indicate that other phenomena (such as sintering) contribute in FBs formation. This is because, as shown in Section 4.3.2, in pressure confinement tests, the ice blocks reach an approximate thermal equilibrium at the time of confinement. Consequently, some FBs which formed during confinement setup preparation may fail and then form new bonds (see Section 4.3.2). The strength of the ice rubble beams in the pressure confinement tests demonstrates that sintering with applied pressure has a more significant effect than heat transfer alone. As observed, the ice blocks (which have no cold reserves) form stronger bonds in higher pressure confinement tests. The sintering process is described in more detail in Section 6.4.

6.1.3 Sintering tests (Phase III)

Figure 6.3 illustrates net force against consolidation time for sintering tests (Phase III) where the initial temperature of the blocks was $0°C$. It can be seen that the net force at 0.3 hours consolidation time was approximately $0kPa$. By increasing the consolidation time from 25 hours to 66.2 hours, the peak load reached $118N$ and $246N$, respectively, and then decreased to $40N$ for the test at 139.7 hours of consolidation. As discussed in Section 4.2.3, the higher peak loads in Test 16 and Test 17 are likely caused by the low air temperature (-1℃) which caused a thin consolidated layer to form. If we neglect these tests and only consider the 0.3 hours and 139.7 hours result (Tests 15 and 18), an increase in beam strength is still evident suggesting that some degree of sintering likely took

place. Further evidence of this was observed from bonded ice blocks that were found at the end of the test (see Figure 4.10). From the work of Boroojerdi *et al.* (in prep, 2017) we know sintering is a relatively slow process, which at the FB level can take on the order of several days to weeks to see significant strength develop. Sintering processes could, however, be accelerated by the presence of an external pressure, and would be expected to a dominant physical mechanism by which the rubble beam strength increases with confinement. Further work is ongoing by Boroojerdi *et al.* (in prep, 2017) to investigate the role of pressure on sintering process.

It is of interest to compare net forces from Test 1 in Phase I, where the initial temperature of the ice was -18°*C*, with Test 15, where the initial temperature was 0°*C* (see Table 4.1. Test matrix). Results show net force was 141*N* higher in Test 1, suggesting that the majority of bond formation takes place in the first 30 minutes, when the temperature difference between the blocks (-18°*C*) and water is at its highest. This is consistent with the Micro-T temperature data which showed that the temperature gradient is at its greatest in the first 20-30 minutes (see Section 4.3), indicating that bonds strength development in this case is driven primarily by thermal processes.

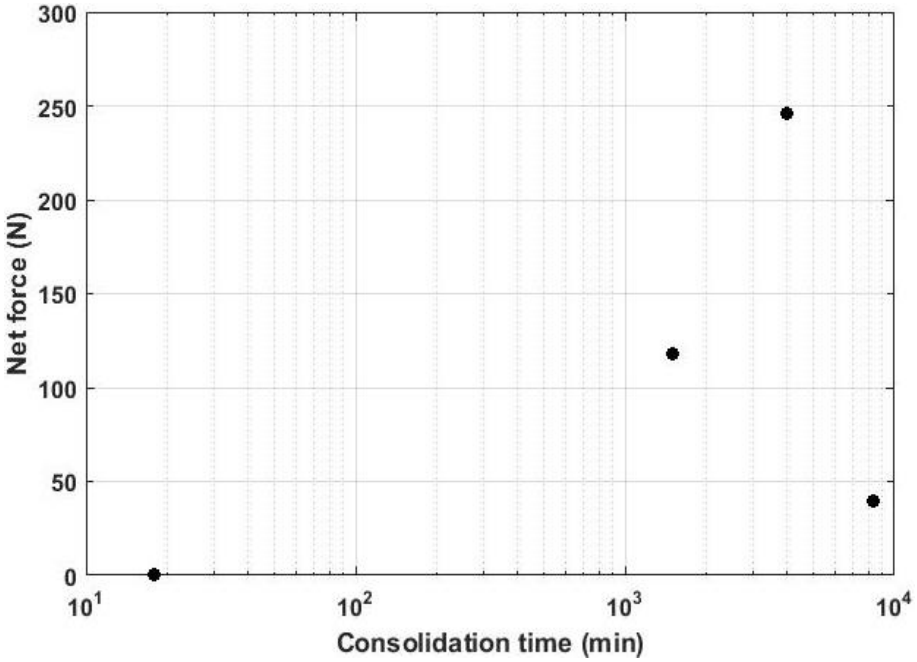

Figure 6.3. Maximum net force vs. consolidation time for sintering tests (Phase III)

6.1.4 Small blocks test (Phase IV)

Test 19 was conducted to investigate the influence of using smaller ice blocks on the strength and failure behavior of the ice rubble beam. The result of Test 19 can be compared with Test 3, 4 and 8, which are shown in Table 5.2**.** If we take the average of Tests 3, 4 and 8 (421*N*), we find the net force is approximately half that value for the small block tests (195*N*). The reduction in force may be due to the fact that smaller ice blocks have less cold reserves causing a reduction in the strength of FBs that form between ice blocks. This is interesting, since it suggests that it is not just the number of FBs that controls the strength of the rubble beams, but rather the degree of bonding between the blocks also plays a highly important role. Additionally, the failure mode, which was a single shear failure (see Section 4.2.4), may have resulted in a load reduction which is associated with lower loads and weaker bonds.

As Urroz and Ettema (1987) argued, in ice rubble and ridges studies, using large blocks would increase the effects of buoyancy force in comparison to FB's strength, as buoyancy is a function of ice blocks' volume and FB strength is a function of both blocks contacted area and volume.

6.2 Friction tests

Figure 6.4 compares the force-displacements from the friction tests for Phase I, II and III to determine if a relationship is evident for the different consolidation times, pressure confinement and sintering. In general, an almost linear relationship is observed between the friction force and beam deformation in all tests. It is suggested that the buoyancy force causes the observed linear increase in the friction forces, since by pushing the beam further, more ice blocks are submerged. The partial load drops that have been recorded in some tests are likely due to either interlocking between the blocks or breaking of some residual FBs.

Figure 6.4a shows that there is no obvious relationship between the friction force and consolidation time. In fact, the slopes of friction force-displacement curves are very similar with the exception of Tests 2 and 4. The higher friction force in Test 4 is likely due to the block positioning, as similarly, higher net force was observed in that test.

Compared to the consolidation time tests, higher friction forces are measured in the pressure confinement tests on average (see Figure 6.4b). Moreover, the figure shows an almost direct relationship between the applied confinement and the rate of friction force, as the minimum and maximum loads are observed in Test 8 and Test 13, $0kPa$ and

40*kPa*, respectively. This is what was expected, as by increasing confinement the ice blocks are more compacted, resulting in an increase in the friction force between the blocks. On a microscopic scale, greater confinement causes increased normal force at the contacts between blocks and facilitates interlocking. Thus, the stress was transmitted further through the beam. This resulted in a higher portion of the beam submerged, causing the increase in the buoyancy force.

It is noteworthy that some tests in Phase II did not follow the direct relationship between the pressure confinement and friction force. This is likely occurred due to the following reasons: 1) Employing larger ice blocks resulted in a less homogeneous beam, therefore the buoyancy effects in each test were unique and not negligible; 2) The failure location in a preceding punch test could affect the friction force, since the volume of the plug failure in the punch test would influence the buoyancy force in the friction test variations.

Similar load traces are observed between the sintering and consolidation time tests (Figure 6.4a and c). This is because no confinement was applied in Phase I and III. There is, however, less variation in the load curves for Phase III. This is due to the fact that the beams failed consistently in shear in these tests because the beams were weakly bonded. Conversely, in the Phase I tests a range of failure modes were observed.

It was observed in some tests (Test 2, Test 8, Test 11, Test 15, Test 17 and Test 18) that at a higher indenter displacement, the load almost reach a constant value. These results are similar to the result of friction force-displacement for Test 19, where after 150*mm* indenter displacement the force did not significantly increased (see Figure 6.4d). This

occurred in tests where shear plug failure took place in the corresponding punch test. Therefore, when the plug was completely submerged in the friction test, the load reached a constant value. This was not the case in the beam bending tests as the non-loaded portion of the beam would also have been progressively submerged as displacement increased. It was expected that Test 1 would demonstrate similar behavior if the indenter was pushed higher in the ice beam.

As discussed by Liferov and Bonnemaire (2005), the higher number of contacts in smaller blocks may increase friction force between the blocks. However, this effect was not observed in the friction force-displacement within Test 19. Additional small blocks tests are required to investigate the effects of blocks dimensions on friction forces in more detail.

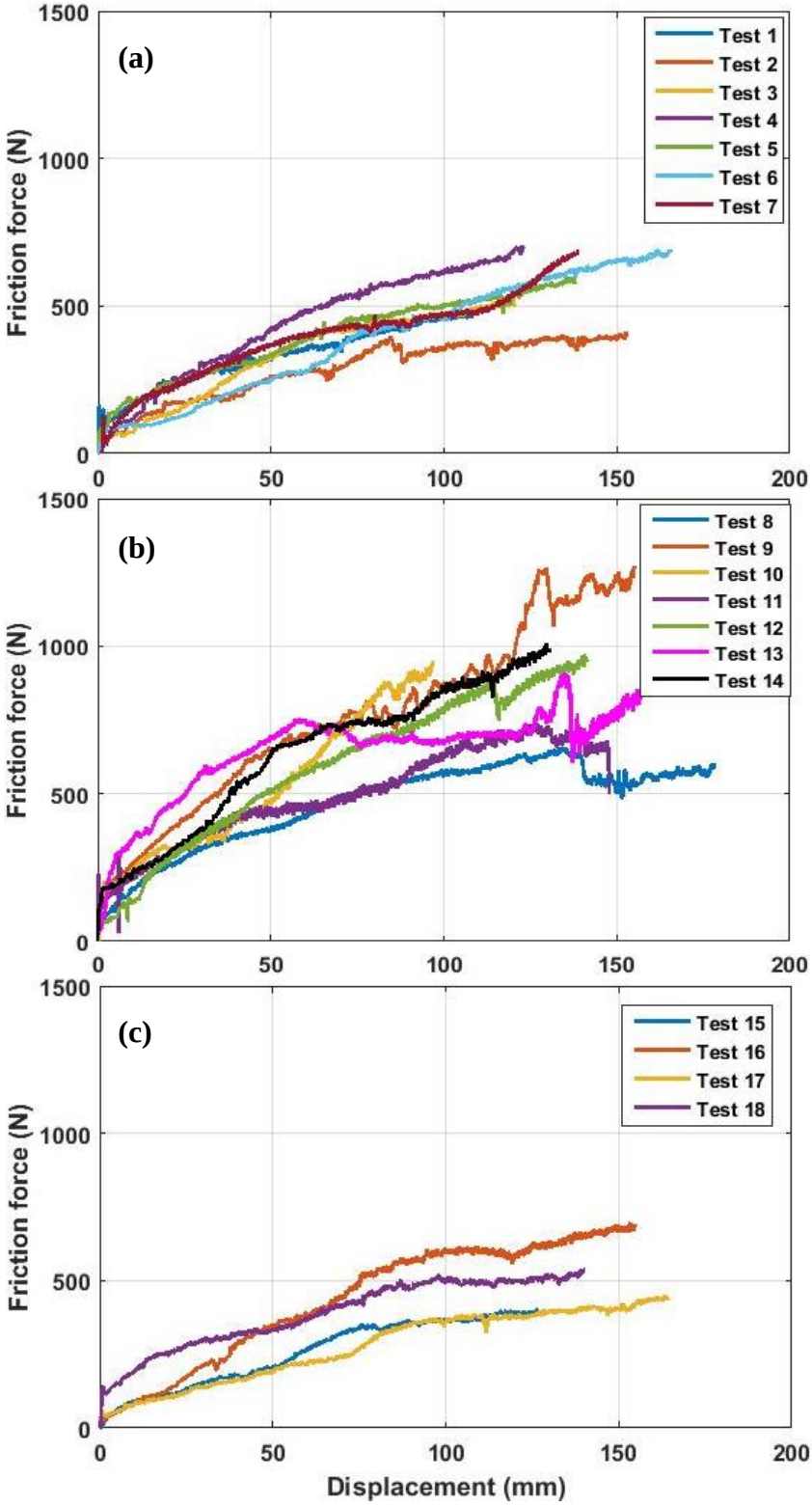

[Continued on page 119]

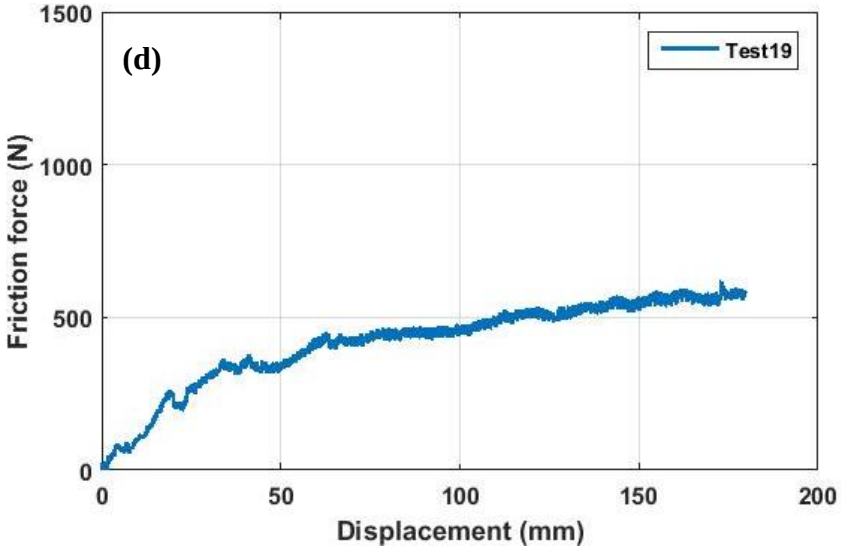

Figure 6.4. Friction force-displacement for (a) consolidation time tests (Phase I), (b) pressure confinement tests (Phase II), (c) sintering tests (Phase III), (d) small ice blocks test (Phase IV).

6.3 Microscopic failure behavior

In Section 4.2, the failure behavior of an ice rubble beam was analyzed on a macroscopic scale, in which the failure modes of the beam were characterized by the degree of the whole beam deformation. In this section, special attention is given to observation of the beam deformation more precisely at block-block contact level (microscopic scale). For this, first, the small fragmentation during pressure confinement is discussed in Section 6.3.1. Following, the microscopic failure behavior of the ice rubble beam in localized tensile and shear are discussed in Sections 6.3.2 and 6.3.3. Then the effects of ice-platen interactions on the failure behavior of the rubble beam are discussed in Section 6.3.4.

6.3.1 Fragmentation

In the pressure confinement tests (Phase II), fragmentation of the ice blocks was observed, in particular, for the ice blocks that were in contact with the top and bottom

confinement platens. Figure 6.5 shows the top of the ice rubble beam after confinement of 0*kPa*, 10*kPa*, 25*kPa* and 40*kPa* here applied to the beam for a period of 4 hours. It can be seen that with greater confinements the top of the beam became increasingly fragmented. The fragmentation was limited to the top and bottom of the beam where the ice blocks contacted the confinement platens. This is because the small contact areas between blocks and platen (shown in Figure 6.6) would be zones of high stress concentration causing local ice block failure.

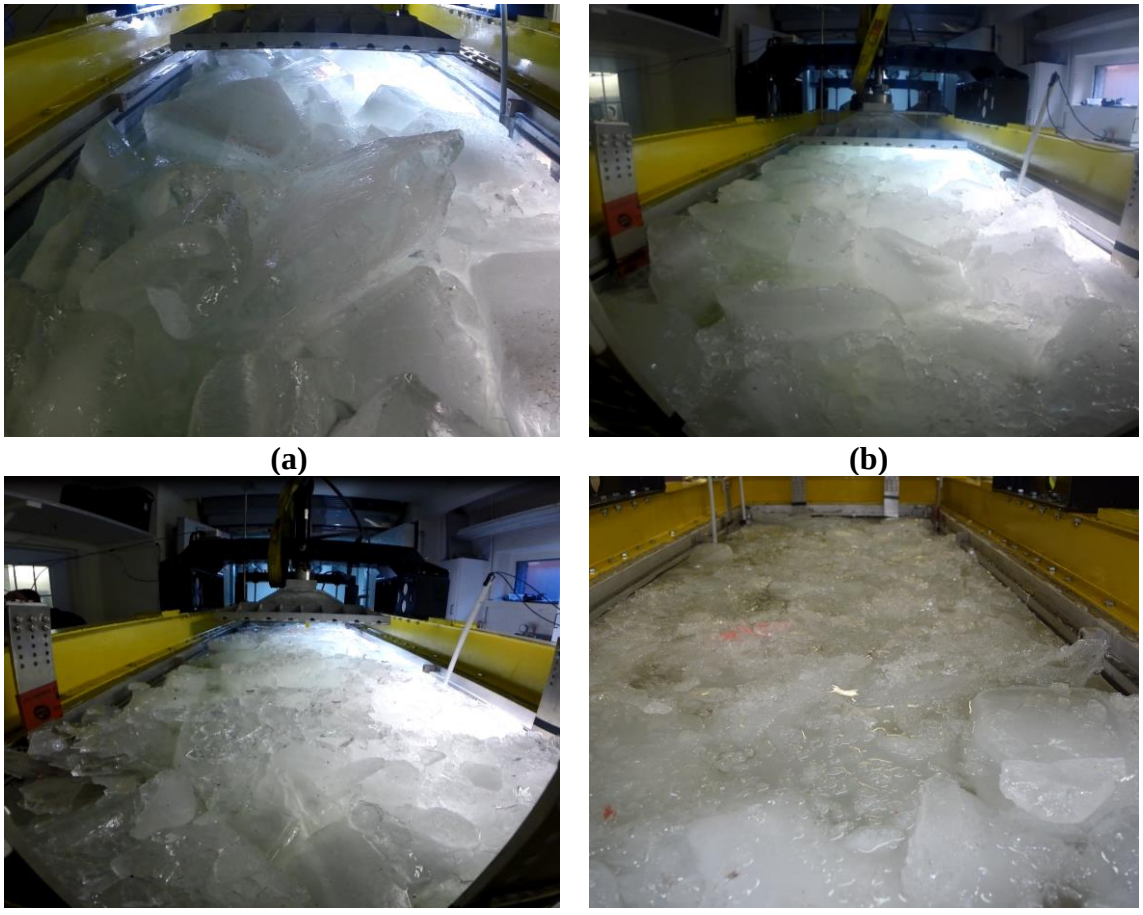

Figure 6.5. The ice rubble beam from the top after 4 hours of confinement under (a) 0*kPa* in Test 3, (b) 10*kPa* in Test 9, (c) 25*kPa* in Test 11, and (d) 40*kPa* in Test 14.

The ice blocks at the top surface of the beam in the 10*kPa* test (Figure 6.5b) were also visibly smoothed, suggesting that some melting may have taken place when confinement was applied. Melting would have been caused by heat transfer through the platen or through pressure melting. Pressure melting is possible close to its melting point (above -1℃) as the pressures required to melt the ice are lower than the mechanical strength of the ice (Szabo and Schneebeli, 2007; Wagener *et al.*, 1994; Colbeck, 1995). Therefore, one could conclude that it is possible that ice blocks at the higher level of the ridge keel break into smaller pieces or fragments when subjected to high confining pressures.

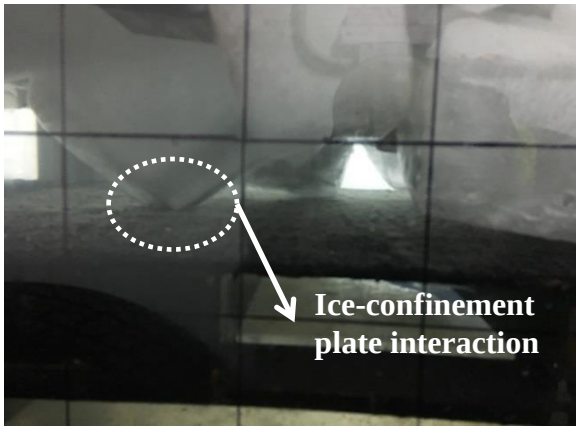

Figure 6.6. Ice-confinement plate interaction.

6.3.2 Localized tensile failure

It was observed in the majority of punch tests that the ice blocks are separated at the central bottom part of the beam. This separation is first observed at the end of the tests, when the platen was at the maximum displacement. By conducting a detailed analysis of the High Speed Video camera (HSV) data, it was observed that the time this failure took place in some tests. In this study, this type of behavior has been referred to as “localized

tensile failure". For example, in Test 12 at 10*cm* of beam deformation, a very slight load drop was observed in the load-displacement curve where a partial failure caused the ice blocks to separate in tension in the central part of the beam.

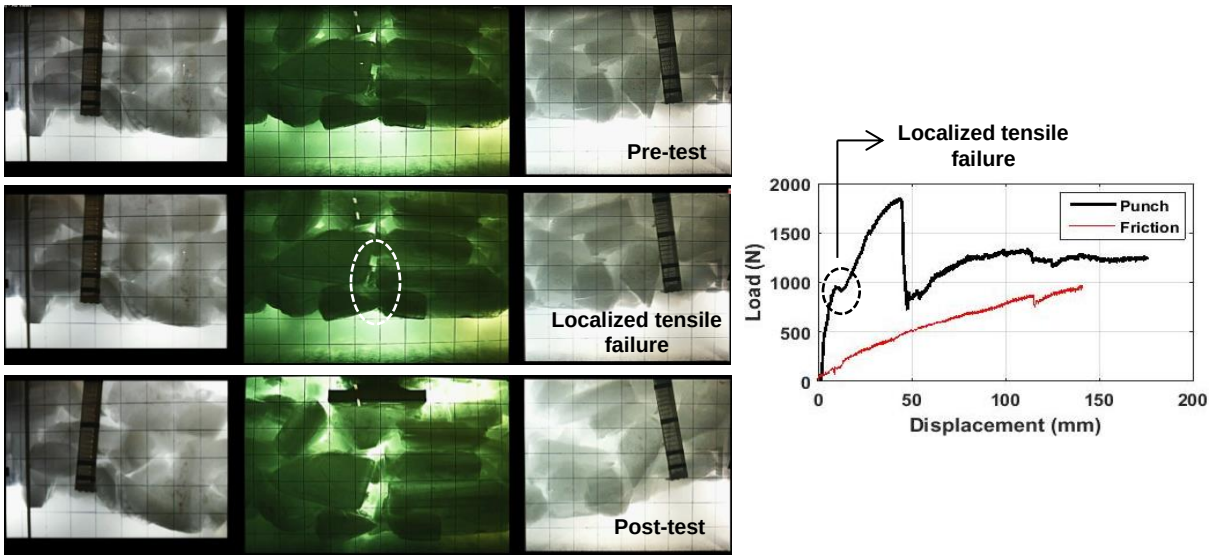

Figure 6.7. Localized tensile failure from Test 12 with 4 hours consolidation and 25*kPa* confinement.

Such localized tensile failures were predominant in tests where the beam failed in bending. Due to the displacement in the centre of the beam being greater than the edges, the blocks at the base of the beam are subject to tension and start to separate. It is also possible that in the confined tests this phenomenon is somewhat enhanced. As the ice blocks in the vertical direction may become more heavily bonded than those in the horizontal direction, this would also promote localized tensile failure.

6.3.3 Localized shear failure

Figure 6.8 shows ice rubble beam failure on block-block contact level for Test 14 on a microscopic scale. As illustrated in Figure 4.7, the rubble failure on the macroscopic

scale was shearing through the whole beam thickness. However, by observing the rubble beam failure on block-block contact level, only one contact failed at the right side of the beam, resulting in a whole beam shear failure at the macroscopic failure. It should be noted that the beam deformation has been assumed planar in this study, as the platen spans the whole width of the beam/box. However, the rubble beam naturally fails in 3D, because the blocks were surrounded by and bonded with other blocks. Therefore, estimating the strength of the ice rubble beam based on observed failure area is not accurate. On the other hand, this also may contribute to the differences between the shear strength on a microscopic scale (freeze-bond tests) and macroscopic scale (ice rubble tests), as shear strength in this study varied between $0.1kPa$ and $8.73kPa$ with an average of $1.6kPa$. However, in the study conducted by Boroojerdi *et al.* (2016) FB strength varied between $50kPa$ to $250kPa$. FBs' strength variation is another possibility that can influence the differences in the results of microscopic and macroscopic scale tests. For example, FBs confined in the vertical direction may have more strength than FBs contacted in a horizontal direction. This variation may be higher in pressure confinement tests. For example, for $25kPa$ pressure confinement, by assuming that only 20% of the blocks are in contact, the pressure at block-block contact may reach $125kPa$. This value may change for each contact pair, based on the associated contact area and direction.

It should be noted that the friction force as well as interlocking may contribute to the shear strength of the ice rubble. Therefore, estimating the number of contacts between the blocks and the exact failure area in the ice rubble and ridges based on the average blocks

size distribution is valuable to estimate the strength of ice rubble. For this, considering the effects of variation further in the strength of FBs is valuable.

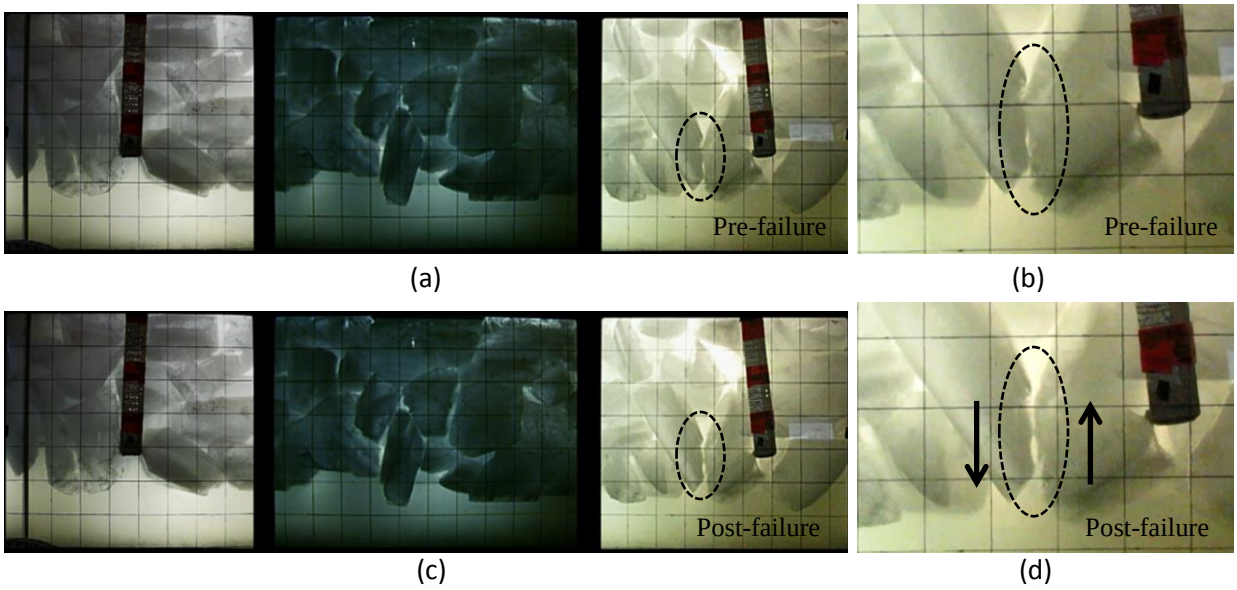

Figure 6.8. Ice rubble beam (a & b) before, (c & d) after shear failure on microscopic scale in Test 14

6.3.4 Ice-platen interaction

Depending on the test phase the contacts between the ice blocks and platen vary. In Phase I and III the ice blocks are randomly positioned which means that at the start of the test only a few ice blocks contacted the platen (see Figure 6.9).

It was observed that in most of Phase I and Phase III tests, the localized tensile failure could be found under the block that was directly under the platen. This is likely due to a high strain (beam deformation) under the highest block, resulting in the first initial failure almost under it. At larger displacements, more ice blocks interacted with the platen. It is noteworthy that in the majority of the tests in both Phase I and Phase III, whether the beam failed progressively (e.g. Test 1) or only one failure occurred (e.g. Test 5), the

major beam failure was located above the localized tensile failure at the bottom of the beam. This is probably caused by a high stress existing in the partial failure zone, or a weakening in that location after the first partial failure.

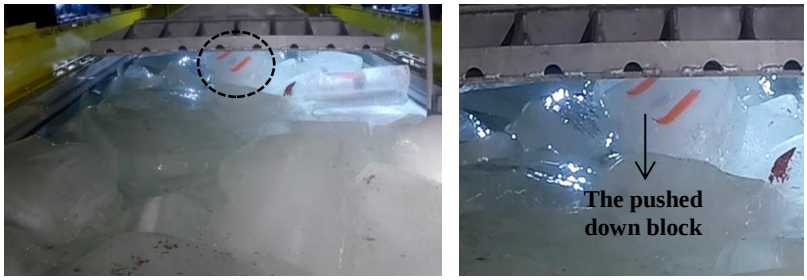

Figure 6.9. Pushing down the highest block under the platen (Test 7)

Different failure behavior was observed in Phase II, as the majority of the failures occurred in the non-loaded portion of the beam. This may be because the load was applied more uniformly to the beam, since the ice rubble beam was confined from both the top and bottom. As a consequence, a larger number of ice blocks interacted area with the platen allowing the stress to be distributed further through the beam, which prevented the main failure to occur above the localized tensile failure. In addition, the confinement process flattens any local ice contact points resulting in more uniform contact conditions.

In Phase IV one camera malfunctioned, therefore, we were not able to observe the ice beam-platen interaction during that test. However, it is expected that in Test 19 more blocks contacted the platen during the test.

6.4 Effects of freezing vs. sintering

As soon as the ice blocks are placed in contact, bonds will form between contacting ice blocks. These are typically referred to as FBs. This term can be a bit misleading as it

implies the bonds are only formed due to thermal freezing processes. However, as has been mentioned, sintering is likely to play a role in freeze bonding. Sintering is a slow process that includes surface diffusion, volume diffusion, surface flow, vapor diffusion, plastic flow and grain boundary diffusion, and significant times would be required for bond formation due to the conditions (Kingery, 1960; Kuriowa, 1962; Hobbs and Mason, 1964; and Maeno and Eniuma, 1983).

Analysis of the Micro-T data (Sections 4.3.1 and 4.3.2) revealed that the temperature of ice rubble in Phase I and Phase II reached 0℃ in approximately two hours of consolidation. Therefore, it can be concluded that there would no longer be any cold reserves (sensible heat) in ice blocks to form additional bonds at higher consolidation times. However, the results of consolidation time tests (Phase I) show that the strength of the ice rubble beam increased after two hours of consolidation. It was also observed that at higher consolidation times, the beam failed in bending, which is indicative of stronger FBs. Furthermore, the results from the sintering tests (Phase III) revealed that when the ice had no or very little cold reserved, the strength gradually increased at higher consolidation times. This increase in the strength has also been attributed to sintering.

Szabo and Schneebeli (2007) argued that the sintering process reaches the maximum rate at melting point. Therefore, it may be concluded that in Phase I the FB formation at the beginning of consolidation was most likely due to freezing, as the ice temperature was much lower than the melting point. At higher consolidation times, when the rubble equilibrated to the melting point, the bond area may have continued to increase due to a

combination of creep and sintering. Interestingly, the ice rubble beam strength did not significantly increase during the first 2 hours of consolidation. A possible explanation for this observation is the large difference between the latent heat and heat capacity of ice.

During Phase II (Section 4.3.2), the ice block temperature data shows that the ice blocks had already (or were close to) thermal equilibrium with the surrounding water temperature when confinement was applied. This suggests that all of the bonds which would have formed through thermal processes would have been formed before confinement was applied. The process of applying confinement would be expected to have broken many of those FBs. Despite this, the strength was observed to increase with confinement suggesting new bonds were also formed. As noted by Szabo and Schneebeli (2007), sintering is known to be accelerated through application of an external pressure. In addition, confinement increases compaction of the matrix, reducing porosity and increasing total contact area.

In summary it may be concluded that the results suggest that sintering is a dominant mechanism in long term strength formation. Understanding this process in more detail is key, especially considering that many ridge keels are likely to be at or close to melting point. It is suggested that additional tests are required where the rubble temperature is at zero and a confinement is applied in order to explore this process in more detail. Work is currently underway by Boroojerdi *et al.* (in prep, 2017) to understand these processes at the FB level.

6.5 The strength of the ice rubble beams

In this section, the shear and flexural strength as well as effective modulus values calculated in Chapter 5 are discussed. Since the majority of ice rubble tests reported in previous studies were set up to measure the shear strength, our results can be compared to previous tests. However, as of yet no research has focused on understanding the flexural properties of rubble, therefore understanding this mechanical characteristic of ice rubble may be particularly important when considering rubble and ridges interactions with sloping structures or vessels. In the new model proposed by Croasdale (2012) the load applied from a First-Year (FY) sea ice ridge interaction with a sloping structure is determined using composite beam theory. For this, information about the flexural strength and effective Young's modulus of rubble and ice ridges are needed. A discussion of shear strength, flexural strength and effective modulus are given below.

6.5.1 Shear strength

Analysis of the results showed that at low consolidation times (0.2 to 4.2 hours) the shear strength was 0.23*kPa* on average. These are similar to the values reported by Azarnejad and Brown (2001), which is surprising considering the different test setup, block size dimensions, initial ice temperature, and ram speed. At higher consolidation times (4.4 to 70.5 hours), the shear strength varied between 1.39*kPa* to 0.54*kPa* with an average of 0.81*kPa*, which indicates that the ice rubble beam is generally stronger and more heavily bonded after longer consolidation times.

It is noteworthy that the bell-shaped curve observed in the shear strength-consolidation time curve for freeze-bond tests (Shafrova and Høyland, 2008; Repetto-Llamazares *et al.*,

2011; Møllegard, 2012; Boroojerdi *et al.*, 2016) was not found in this study (see Figure 2.3). This may be due to the contributions of a number of parameters as discussed below:

1) Boroojerdi *et al.* (2016) found in freeze-bond tests that small ice blocks reach thermal equilibrium after 30 minutes of consolidation time, which the FBs reaching maximum strength during the first 2-5 minutes. Therefore, by assuming a linear relationship between the time the ice blocks reach equilibrium temperature and the size of the ice blocks' dimensions, we would expect the peak load would occur in the first 20-30 minutes of consolidation. This was not observed in this study. Additional tests are suggested to investigate the strength and failure behavior of ice rubble after 30 minutes of consolidation. Differences for boundary conditions of an ice block inside a rubble mass versus those for an isolated pair of blocks are important to consider further.

2) Although it is expected that the maximum strength occurs within the first 20-30 minutes, our results showed that the maximum and minimum shear strength occurred at 4.4 and 4.2 hours consolidations. This is likely due to the effect of ice block positioning, the sintering process, additional block warming, as well as possible melting in some tests due to differences in setup times, or using larger ice block dimensions. These factors may act to delay the peak in the bell-shaped curve. Additional tests are needed to find the maximum strength at each consolidation time.

3) As projected failure area does not account for porosity and the ice rubble beam naturally fails in 3-dimensions (see Section 4.2), increasing the estimated failure area can

lead to the differences in shear strength against consolidation time curves. Therefore, estimating shear strength based on actual ice block-block contact would be required to compare the results with freeze-bond tests.

4) As shown in previous sections, the FBs may fail in tension as well as shear during ice rubble beam failure. The bell-shaped curve is only associated with FB's shear strength, and it is unknown if tensile strength follows a similar trend.

The results of Phase II tests show a linear relationship between pressure confinement and shear strength. Referring to Table 5.2, at 0*kP* confinement, average shear strength was 0.84*kPa* (average of Tests 3, 4 and 8) and then slightly increased to an average value of 7.4*kPa* at 40*kPa* pressure confinement. These shear strength values at high confinement are at the low end values found in *in-situ* field punch tests, but are in the same range as full-scale values.

6.5.2 Flexural strength

Since there is no data with which to compare we shall limit our discussion to tests where the beam failed in bending. The analysis of video data showed that at high consolidation times (4.4 hours to 70.5 hours) and under higher confinement (10*kPa* to 40*kPa*) the beam failed in bending. The flexural strength values varied from 12.4*kPa* to 3.25*kPa* with an average of 6.67*kPa* for longer consolidation times. Whereas, when confinement increased from 10*kPa* to 40*kPa* the flexural strength linearly increased from 15*kPa* to 59*kPa*. Interestingly, comparison of the results with the value used by Croasdale (2012) for the composite beam analysis show that the confinement tests are of same order of magnitude.

In this analysis, he assumed a 25kPa flexural strength for a 24.3m keel in thickness that was based on tensile failure measured in pull-up tests.

The flexural strength of the beam consisting of small ice blocks was 3.3kPa. This value is in the range of those measured in large block tests under similar conditions (Tests 3, 4 and 8, see Table 5.2), which show that the flexural strength did not significantly change for the smaller blocks test.

It is of interest to compare our flexural strength values to those of solid ice beams of similar dimensions. Gow *et al.* (1978) conducted cantilever tests on freshwater ice beams of 1.16m^3 to 1.38m^3, in which they found flexural strength varied between 0.52MPa and 0.74MPa. The flexural strength of freshwater ice is found to be much higher than that of the rubble beam conducted in this study. This is not surprising as ice rubble is a porous/granular material and the strength of FBs is less than that for continuous ice (Shafrova and Høyland, 2008).

6.5.3 Effective modulus

Figure 6.10 compares the effective elastic modulus in consolidation time tests (Phase I), pressure confinement tests (Phase II), and sintering tests (Phase III) (see Section 5.3). Referring to Figure 6.10a, the effective elastic modulus for consolidation time tests was in the range of 0.1MPa to 0.14MPa, except for Test 4 in which the effective modulus reached about 0.42MPa. This high difference may be due to the block positioning in Test 4. The fact that the effective Young's modulus is roughly constant for Phase I tests suggests that consolidation time does not significantly effect the stiffness of the material.

Figure 6.10b shows an almost linear relationship between the effective elastic modulus and pressure confinement. This means that by compacting the rubble beam, the stiffness of the rubble beam increases. This is similar to the arguments in Section 4.2, for more/stronger FBs, the rubble beam behaves more like a porous solid. At low consolidation and confinement, the ice rubble behaves more like a granular material.

Figure 6.10c shows the effective elastic modulus in sintering tests which varied between $0.15MPa$ and $0.24MPa$, except in Test 15 when the buoyancy force was almost equal to the total load. No significant changes in the effective modulus were found at higher consolidations, indicating that sintering is a slow process. In addition, it may be concluded that the surface melting of the outer rubble does not affect the overall stiffness. Referring to Table 2, the effective elastic modulus in Test 19 was $0.07MPa$ which was the lowest found. This may be because the beam failed at higher deflection.

It is interesting that the results of effective Young's modulus estimated in Phase I and III are in the same order suggested by Croasdale (2012). For a $24.3m$ keel, they estimated the effective Young's modulus of $0.33 \times 10^5 MPa$, while the suggested flexural strength of the same keel was similar to the results of pressure confinement tests.

In general, the results demonstrate that the beam had the highest stiffness in pressure confinement tests. It is observed that under $40kPa$ confinement, the stiffness was about 25 times higher than that in consolidation time tests. This means that an ice ridge may be stiffer near the water level, as the blocks are more confined, and at the lower parts it behaves more like a granular material due to less confinement.

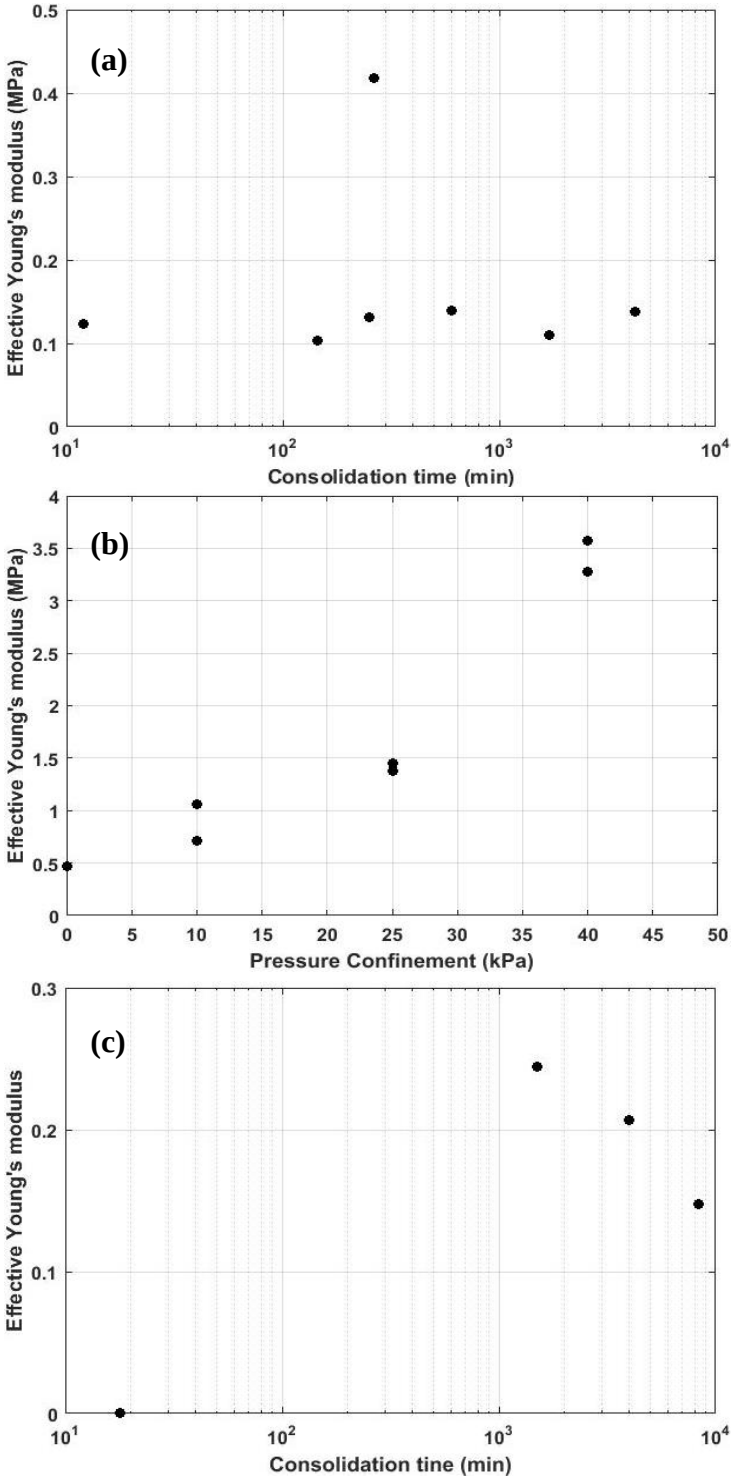

Figure 6.10. Effective Young's modulus of (a) consolidation time tests (Phase I); (b) pressure confinement tests (Phase II), and (c) sintering tests (Phase III).

7 Conclusions and Recommendations

7.1 Conclusions

The principal aim of this project was to investigate the effects of key parameters on the mechanical characteristics of ice ridge keels. As ice ridges are common features in Arctic and sub-Arctic regions, they may interact with offshore structures, subsea pipelines, and vessels and, as such, need to be considered in engineering design. Although many field and laboratory punch tests have been carried out in previous studies, the effects of some parameters on the strength and failure behavior of ice rubble and ridges are still unclear. To gain a greater understanding of these processes, nineteen (19) ice rubble beam punch tests have been conducted in C-CORE's Cold Room facility to investigate the effects of consolidation time (0 hrs-70.5 hrs), pressure confinement (0kPa-40kPa), as well as sintering and ice block dimensions.

Analysis of the results revealed that the failure behavior of an ice rubble beam is controlled by the degree of freeze bonding between the blocks. By increasing either consolidation time or pressure confinement the ice blocks became more heavily bonded, resulting in a stronger beam that required a greater force to fail. This caused the rubble beam to behave more like a solid porous material failing in bending. In contrast, for non-confined or less consolidated ice rubble, the ice blocks were less bonded, and consequently the rubble behaved more like a cohesive granular material, which deformed as a shear plug. Moreover, as the microscopic scale (block-block contact) analysis showed, FBs may fail in either shear or tension. This suggests that it may not be correct

to assume that ice ridge keels fail in pure shear, as has been assumed in most ice loading models to date but rather a combination of shearing and bending.

Comparison of the results showed that confinement has the most dominant effect on the ice rubble beam strength, where the strength increased almost linearly with confinement. The shear and flexural strengths calculated for the tests where 40kPa confining pressure was applied to the beam were of the order measured in in-situ punch tests and the value used by Croasdale (2012) for his composite beam analysis, respectively. The strength of the beams increased with confinement due to compaction, increasing the number of block-block contacts, as well as the role of confinement has on the bonding process. Also, by increasing confinement the ice blocks are more compacted, resulting in an increase in the friction force between the blocks. Further support for the role confinement has on bonding process comes from the analysis of the Micro-T temperature data, which showed that the ice block temperatures had almost reached 0°C at the initiation of confinement, indicating that the ice blocks would have minimal cold reserves to form new FBs. This suggests different mechanisms were controlling bond formation, such as sintering and/or pressure melting. Results from the sintering tests showed that sintering is a very slow process in the absence of an external pressure. Sintering may, however, be accelerated when sufficient pressure is applied through creep and plastic deformation at the contact points as was suggested by Szabo and Schneebeli (2007) and Schulson and Fortt (2013). Results from FBs have shown consistent results where the shear strength of the bond increased with confinement (Ettema and Schaefer, 1986; Repetto-Llamazares *et al.*, 2011).

The results of pressure confinement tests support the idea that a strength gradient exists in ridge keels, where the strength towards the waterline is highest directly below the consolidated layer, reaching near zero values towards the base. Timco et al. (2000) suggested that the reason for the strength gradient could be due to buoyancy forces, increasing confinement towards the top of the keel. It is also possible that because the majority of confinement is in the vertical direction that FBs will be stronger in the horizontal, which may influence the failure behaviour of ridges. For instance, shear plug failure would not be favorable under these conditions, but rather local passive failure and or bending. The increase in strength with confinement could also have important implications for gouging, pitting and stamukhi were confinement could be considerably higher.

7.2 Recommendations for future research

In order to develop deeper investigations on the mechanical characteristics of ice rubble and ridges, the following research studies are suggested:

- More repeat tests for each specified condition are required, as it is believed the blocks' random positioning and the random strength of FBs would effect the total strength of the ice rubble beam;
- Additional tests to investigate the effects of pressure confinement at different consolidations times;
- Further tests to investigate the effects of ice blocks size on ice rubble behaviour as well as its thermal properties;

- As the majority of ice ridges form in saline water, it is suggested to repeat these tests with saline ice;
- Further analysis of the data using techniques such as multi-variable regression is recommended for the future research;
- To compare different datasets and simplify the analysis, exploring application of non-dimensional analysis (e.g. Bruneau, 1996) would be of interest;
- As the scale of the blocks plays an important role in the bond strength, scale of bond strength is an important area for further consideration. Therefore, additional work is needed to understand how smaller scale results translate to full-scale;
- Additional tests are suggested which incorporate both ice rubble and a consolidated layer, in particular for application to the composite beam work proposed by Croasdale (2012) for estimating the ridge loads on sloping structure;
- As it was found confinement plays the key role on the strength of ice rubble, employing a tactile pressure sensor to measure pressure at block-block interaction during consolidation would be helpful for comparing the results with freeze-bond tests (block-block contact);
- As it was observed that FBs may fail in tension (or possibly compression), as well as shear, it is suggested that freeze-bond tests also deform bonds in tension and compression;
- Estimating the number of contacts between the blocks and the exact failure area in the ice rubble and ridges based on the average blocks size distribution would help to better estimate the strength of ice rubble;

- Using this data to develop and validate a numerical model capable simulating multiple test conditions.

While the above recommended work would help build on and extend the current experimental program, it may be concluded that this research has helped provide new insights into understanding the mechanical characteristics of ice rubble and ice ridges, which can be built upon going forward to help address this highly important aspect of ice engineering.

REFERENCES

Azarnejad, A., & Brown, T., 1998. Observations of ice rubble behaviour in punch tests. *Proceedings of the 14th International Symposium on Ice*. Newyork, US, pp. 589-596.

Azarnejad, A., & Brown, T., 2001. Ice rubble behavior in punch test. *Journal of Cold* Regions Engineering, 15(3), pp. 135-153.

Bailey, E., Bruce, J. E., Derradji, A., and Lau, M., 2014a, "An overview of the development of ice ridge keels strength testing program," *Proceedings of the 3rd Arctic Technology Conference.* Houston, Texas, 10-12 February 2014 (OTC-24553-MS)

Bailey, E., Bruce, J. E., and Taylor, R., 2014b, "The Development of Ice Ridge Keel Strengths: The influence of speed on the strength and deformation behaviour of gouging ridge keel," *Proceedings of the 22nd IAHR International Symposium on Ice*, Singapore, 11-15 August 2014.

Bailey, E., Taylor, R., & Croasdale, K., 2015. Mechanics of Ice Rubble Over Multiple Scales. *Proceesings of the ASME 2015 34th International Conference on Ocean,* Offshore and Arctic Engineering. St. John's, Canada.

Blackford, Jane R. 2007. "Sintering and Microstructure of Ice: A Review." *Journal of Physics D: Applied Physics* 40 (21): R355.

Boroojerdi, M. T., Ghobadi, M., Taylor, R., Bailey, E., 2016. Experimental study on shear strength of Freeze bonds in freshwater ice. *Arctic Technology Conference*, 24-26 October, St. John's, Newfoundland and Labrador, Canada.

Bowden, F. P., and T. P. Hughes. 1939. "The Mechanism of Sliding on Ice and Snow." *Proceedings of the Royal Society A,* 172: 280–98.

BP Energy Outlook 2035. February 2015. Available at: bp.com/energy outlook

Bruneau, S., 1997, "Development of a First-Year Ridge Keel Load Model," PhD thesis, Memorial University of Newfoundland, St. John's, Newfoundland., Canada.

Canada's Oil & Natural Gas Producers. Offshore projects and exploration in NL (2015) Available at: http://atlanticcanadaoffshore.ca/projects-exploration-newfoundland-labrador/ (Accessed: 1 February 2016).

Circum-Arctic Resource Appraisal: Estimates of Undiscovered Oil and Gas North of the Arctic Circle. 2008. The U.S. Geological Survey (USGS). At, Pubs.usgs.gov. URL: https://pubs.usgs.gov/fs/2008/3049/fs2008-3049.pdf

Colbeck, S. C., 1995. Pressure melting and ice skating. American Journal *of Physics*, 63, pp. 888-890.

Cornett, A., & Timco, G., 1995. Laboratory tests on the mechanical properties of saline ice rubble. NRC Report HYD-CTR-002, 171 pp.

Cornett, A.M., Timco, G.W., 1996. Mechanical properties of dry saline ice rubble. *Proceedings of the 6th International Offshore and Polar Engineering Conference*. Los Angeles, USA, vol. 2, pp. 297– 303.

Croasdale & Associates Ltd., 1996. In situ strength measurements of first year pressure ridges and rubble fields. A study for the National Energy Board, Canada, supported by PERD.

Croasdale & Associates Ltd., 1997. *In-situ* Ridge Strength Measurements. A study sponsored by NRC (PERD) and Exxon Production Research Co.

Croasdale & Associates Ltd., 1998. *In-situ* Ridge Strength Measurements. A study sponsored by NRC (PERD) and Exxon Production Research Co.

Croasdale, K. R., Bruneau, S., Christian, D., Crocker, G., English, J., Metge, M., Ritch, R., 2001. *In-situ* measurements of the strength of first-year ice ridge keels. *Proceedings of the 16th International Conference on Port and Ocean Engineering under Arctic Conditions (POAC'01)*. August 12-17, Ottawa, Ontario, Canada.

Croasdale, K.R., 2012. A simple model for first-year ridge loads on sloping structures. *Proceedings, IceTech*, Banff, 2012.

Dash, J. G., Mason, B. L., and Wettlaufer, J. S., 2001. Theory of charge and mass transfer in ice-ice collisions. *Journal of Geophysical Research,* 106, 20395.

Dash, J. G. and Wettlaufer, J. S., 2003. The surface physics of ice in thunderstorms. *Canadian Journal of Physics.* 81, 201 (2003)

Dolan, D.H. and GuptaY.M, 2004. *Journal of Chemical Physics* 121, 9050.

Ettema, R., & Schaefer, J., 1986. Experiments on freeze-bonding between ice blocks in floating ice rubble. *Journal of Glaciology,* 32 (112), pp. 397-403.

Ettema, R., Urroz, G., 1989. On internal friction and cohesion in unconsolidated ice rubble. *Cold Regions Science and Technology,* 16, pp. 237-247.

Ettema, R., Urroz, G., 1991. Friction and cohesion in ice rubble reviewed. *Proceedings. of the 6th International Speciality Conference*. Cold Regions Engineering. Hanover, USA, pp. 316-325.

Fransson, L., & Sandkvist, J., 1985. Brash ice shear properties - laboratory tests. *Proceedings of the 8th International Conference on Port and Ocean Engineering under Arctic Conditions*, Narssarssuaq, Greenland, vol. 1, pp. 75-87.

Gow, A.J., Ueda, H.T., Ricard, J.A., 1978. Flexural strength of ice on temperate lakes: comparative tests of large cantilever and simply supported beams. *USA Cold Regions* Research and Engineering Laboratory. CRREL report 78-9, pp. 1-14

Guy, E., Lasserre, F., 2016. Commercial shipping in the Arctic: new perspectives, challenges and regulations. *Cambridge University press*. Polar Record 52 (264), pp 294-304.

Heinonen, J., & Määttänen, M., 2000. LOLEIF ridge-loading experiments-analysis of rubble strength in ridge keel punch test. *Proceedings of the 15th International Symposium on Ice*, Gdnask, Poland, vol.1, pp. 63-72.

Hellmann, J., 1984. Basic investigations of Mush Ice. *Proceedings of the 7th International Symposium on Ice*, Hamburg, Germany, vol.3, pp. 37-55.

Hobbs, P.V., Mason, B.J., 1964. The sintering and adhesion of ice. *Philosophical* magazine. 9 (98), pp. 181-197.

Jensen, A., Høyland, K.V., Evers, K.-U., 2000. Scaling and measurements of ice rubble properties in laboratory tests. *Proceedings of the 15th International Symposium on Ice*. Gdansk, Poland, vol. 1, pp. 105–112.

Jensen, A., Løset, S., Høyland, K.V., Liferov, P., Heinonen, J., Evers, K.-U., Määttänen, M., 2001. Physical modelling of first year ice ridges, Part II: mechanical properties. Proceedings of the 16th International Conference on Port and Ocean Engineering under Arctic conditions, Ottawa, Canada Vol. 3, pp. 1493-1502.

Keinonen, A., & Nyman, T., 1978. An experimental model-scale study on compressible,frictional and cohesive behavior of broken ice masses. *Proceedings of the International Symposium on Ice*, Lulea, Sweden. Vol. 2, pp. 335-353.

Kingery, W. D., 1960. Regelation, surface diffusion, and ice sintering. *Journal of Applied Physics*, 31(5), pp. 833-838.

Kuroiwa, D., 1961. A study of ice sintering. *Tellus*, 13(2), pp. 252-259.

Lemee, E., & Brown, T., 2002. Small-scale plane strain punch tests. *Proceedings of the 16th IAHR International Symposium on Ice*, Dunedin, New Zealand, vol. 2, pp. 1-8.

Leppäranta, M., & Hakala, R., 1992. The structure and strength of first-year ridges in the Baltic Sea. Cold Regions Science and Technology 20, pp. 295-311.

Leppäranta, M., 2011. The Drift of Sea Ice, 2nd edition. Springer-Verlag, Heidelberg.

Liferov, P., Jensen, A., Høyland, K.V., Løset, S., 2002. On analysis of punch tests on ice rubble. *Proceedings of the 16th International Symposium on Ice*, Dunedin, New-Zealand, vol. 2, pp. 101– 109.

Liferov, P., & Bonnemaire, B., 2005. Ice rubble behaviour and strength: Part I. Review of testing and interpretation of results. Cold Regions Science and Technology 41, pp. 135-151.

Løset, S., & Sayed, M., 1993. Proportional strain tests of fresh water ice rubble. *Cold Regions Science and Technology* 7 (2), pp. 44-61.

Maeno, N., & Eniuma, T., 1983. Pressure sintering of ice and its implication to the densification of snow at polar glaciers and ice sheets. *The Journal of Physical Chemistry*, 87(21), pp. 4103-4110.

Møllegaard, A., 2012. Experimental study on freeze-bonds in laboratory made saline ice.

Palmer, A., Croasdale, K., 2013. Arctic offshore engineering. World Scientific Publishing.

Prodanovic, A., 1979. Model tests of ice rubble strength. *Proceedings of the 5th International Conference on Port and Ocean Engineering under Arctic Conditions*, Trondheim, Norway, pp. 89-105.

Repetto-Llamazares, A., & Høyland, K., 2011. Experimental studies of shear failure on freeze-bonds in saline ice part I: set-up, failure mode and freeze-bond strength. *Cold Regions Science and Technology*, 65, pp. 286-297.

Sayed, M., Timco, G. W., & Sun, L., 1992. Testing model ice rubble under proportional strains. *In Proceedings of the 11th International Conference On Offshore Mechanics and Arctic Engineering*, 4. Calgary, Canada.

Schulson E. M., and Fortt A. L., 2013. Static strengthening of frictional surfaces of ice. *Acta Mater*., 2013, 61, pp. 1616-1623.

Schwarz, J., Frederking, R., Gavrillo, V., Pertov, I. G., Hirayama, K. I., Mellor, M., Tyrde, P., Vaudrey, K.D., 1981. Standardized testing methods for measuring mechanical properties of ice. Cold Regions Science and Technology, 4, pp. 245-253.

Serré, N., Repetto-Llamazares, A. H., Høyland, K. V., 2011. Experiments on the relation between freeze-bonds and ice rubble strength, Part I: Shear box experiments. *Proceedings of the 21st International Conference on Port and Ocean Engineering under Arctic Conditions*, Montreal, Canada.

Shafrova, S., & Høyland, K., 2008. The freeze-bond strength in first-year ice ridges. Small-scale field and laboratory experiments. *Cold Regions Science and Technology*, 117(4), pp. 54-71.

Smirnov,V., Sheikin, I.B., Shushlebin, A., Kharitonov, V., Croasdale, K. R., Metge, M., Ritch, R., Polomoshnov, A., Surkov, G., Wang, A., Beketsky, S., and Weaver, J.S., 1999. Large Scale Strength Measurements of Ice Ridges: Sakhalin, 1998. *RAO Conference*, St. Petersburg, 1999.

Strub-Klein, L., and Sudom, D., 2012. A comprehensive analysis of the morphology of firstyear sea ice ridges. *Cold Regions Science and Technology*, 82, pp. 94–109.

Sudom, D., Timco, G., Sand, B., Fransson, L., 2011. Analysis of first-year and old ice ridge characteristics. *Proceedings of the 11th International Conference on Port and Ocean Engineering under Arctic Conditions*, Montreal, Canada.

Szabo, D., & Schneebeli, M. (2007). Subsecond sintering of ice. *Applied Physics Letters*, 90(15).

The Economy 2015, Newfoundland and Labrador's Offshore, Available at: http://www.economics.gov.nl.ca/E2015/TheEconomy2015.pdf (Accessed: 6 February 2016).

Thomson, James. 1860. "On Crystallization and Liquefaction, as Influenced by Stresses Tending to Change of Form in the Crystals." *Proceedings of the Royal Society of London* 11: 472–81.

Timco, G.W., 1986. 'EG/AD/S: a new type of model ice for refrigerated towing tanks. *Cold Regions Science and Technology* 12, pp. 175-195.

Timco, G.W., Frederking, R.M.W., 1990. Compressive strength of sea ice sheets. *Cold Regions Science and Technology*, 17, pp. 227–240.

Timco, G., Funke, E., Sayed, M., & Laurich, P., 1992. A laboratory apparatus to measure the behavior of ice rubble. *Proceedings of Offshore Mechanics and Arctic Engineering Conference*, Calgary, Canada, pp. 369-375.

Timco, G.W., Burden, R.P., 1997. An analysis of the shape of sea ice ridges. *Cold Regions Science and Technology*, 25, pp. 65–77.

Timco, G., & Cornett, A., 1999. Is ρ a constant for broken ice rubble? *Proceeding of the 10th Workshop on River Ice Management with a Changing Climate*, Winnipeg, Manitoba, Canada. *pp. 318-331*.

Timco, G., Croasdale, K., & Wright, B., 2000. An Overview of First-Year Sea Ice Ridges. NRC Publications Archive, Canada.

Urroz, G. E., & Ettema, R., 1987. Simple-shear box experiments with floating ice rubble. *Cold Regions Science and Technology*, 14, 185-199.

Wagner, W., Saul, A., Pruβ, A., 1994. International equations for the pressure along the melting and along the sublimation curve of ordinary water substance. *Journal of Physical and Chemical*. Vol. 23, No. 2. pp 515-527

Weiss, R., Prodanovic, A., & Wood, K., 1981. Determination of ice rubble shear properties . Proceeding of the International Symposium on Ice, Quebec, Canada, pp. 860-872.

Appendix A: Platen Area

The dimensions of the platen is one of the crucial parameters which requires special attention. In this study, the length of the platen is approximately equal to the box width, with a relatively small clearance allowance. Therefore, the width of the platen is the only variable. The platen area may affect the stress distribution through the ice rubble, the type of failure behavior (trapezoidal or triangular), nominal pressure, effective platen width and the effects these have on the deflection of bending. The problem in choosing a platen that is too small is that a singular ice block failure may be measured rather than the whole plug failure. The importance of this parameter will double when the dimensions and directions of the ice rubble in this experiment are random. Therefore, either the platen dimensions have to be appropriate for different sizes of ice rubble, or multiple platens must be made. Some parameters such as the minimum bending deflection, the ratio of platen width to box length, the number of ice-platen interactions, and the amount of buoyancy force can be used to define an interval for platen width and measure its critical value. In this experiment, the ratio of the platen width (B) and box length (l), and a minimum allowable number of ice blocks that interact with the platen are suggested as critical parameters to estimate the optimum platen width.

Appropriate platen size has been discussed for various punch tests. The ratio of the platen width and box length used by Azarnejad and Brown (2001) and Lemee and Brown (2002) was about 0.1. Jensen *et al.* (2000, 2001) used a ratio of 0.17. Heinonen and Määttänen (2000) proposed that both keel depth and platen perimeter should be ten times the ice

block thickness. Since the ice blocks have various dimensions, it is important that the platen pushes a sufficient amount of ice to find the average strength of the ice rubble.

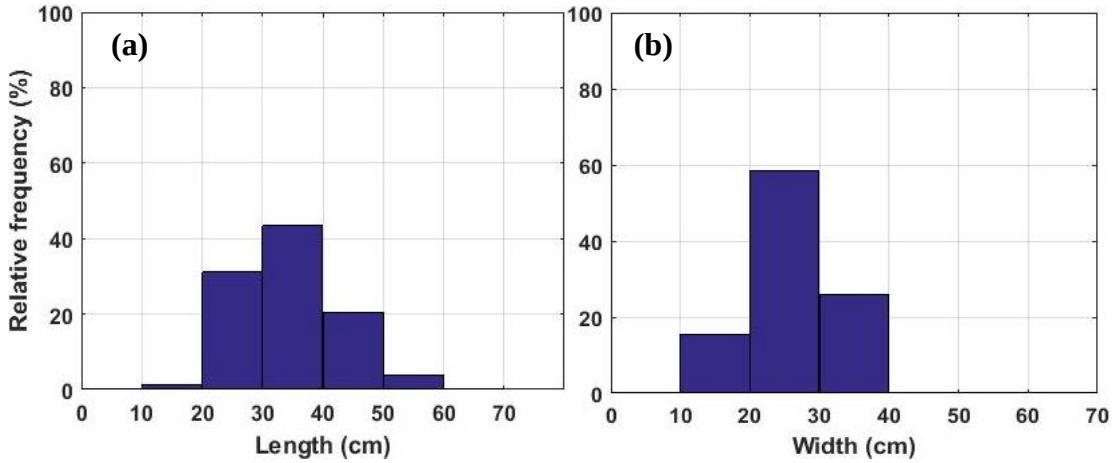

Figure A.1. Histograms of the length (a), width (b) of the ice blocks for DIRKS project

Figure A.1a and 1b show the length and width distributions of the ice blocks employed in the DIRKS project. In this study, the critical platen width was estimated based on the ice blocks dimensions used in the DIRKS project, as a similar methodology was used in this project to make ice blocks. Since the rubble dimensions vary in each test, the platen may correspondingly push differing quantities of rubble. As shown in Table A.1, to accommodate this randomness, the number of minimum allowable ice rubble interactions has been defined for various dimensions of the ice rubble. In a precautionary approach, the minimum allowable number of ice blocks is based on the maximum ice block length, not thickness. It is preferable that smaller ice blocks are under the platen because it will more closely simulate a plug failure. The calculated platen width is assumed to be the minimum. By increasing its width, more ice blocks are covered. The ice surface porosity is assumed to be equal to the overall volume porosity. Equation (A.1) shows the minimum number of ice blocks based on porosity, platen area and average area of the ice,

$$n = \frac{(1-\eta')A_{platen}}{A_{ice(average)}} \tag{A.1}$$

where, A_{platen} is the area of platen, $A_{ice(average)}$ is the average area of individual ice blocks, n is the number of ice blocks that are covered by the platen, η' is the porosity of the area (equal to the overall volume porosity).

By defining the ratio of the platen area and the punch box area shown in Equation (A.2), the platen width can be determined by multiplying the number of ice blocks defined as a function of the ratio found in Equation (A.3):

$$\mathrm{R} = \frac{A_{plate}}{A_{box}} = \frac{B}{l} \tag{A.2}$$

$$n = \frac{(1-\eta')A_{box}}{A_{ice(average)}} R \tag{A.3}$$

where A_{box} is the horizontal area of the box width. It is obvious that by increasing the platen size, more ice blocks can be displaced downwards. However, the width is limited by the maximum allowable ratio of platen width to box length (R). In this experiment, the maximum allowable ratio of $\frac{B}{l}$ is suggested to be 0.2. As a consequence of this, the maximum allowable platen width is $0.6m$. This will prevent the surrounding walls from significantly affecting the results for ice rubble shear failure.

Table A.1. Ice dimension classifications

Type	Thickness (m)	Width (m)	Length (m)
Small	0.1	0.15	0.2
Medium		0.25	0.35
Large		0.35	0.55
Most Frequent		0.2	0.25

According to Figure A.2, by assuming the maximum allowable ratio $R = 0.2$ (in which $B = 60cm$), the appropriate quantity of ice rubble is covered by the platen. In this case, the focus is on the most frequent ice rubble type, because the large and medium pieces of ice rubble can be moved to another location of the box.

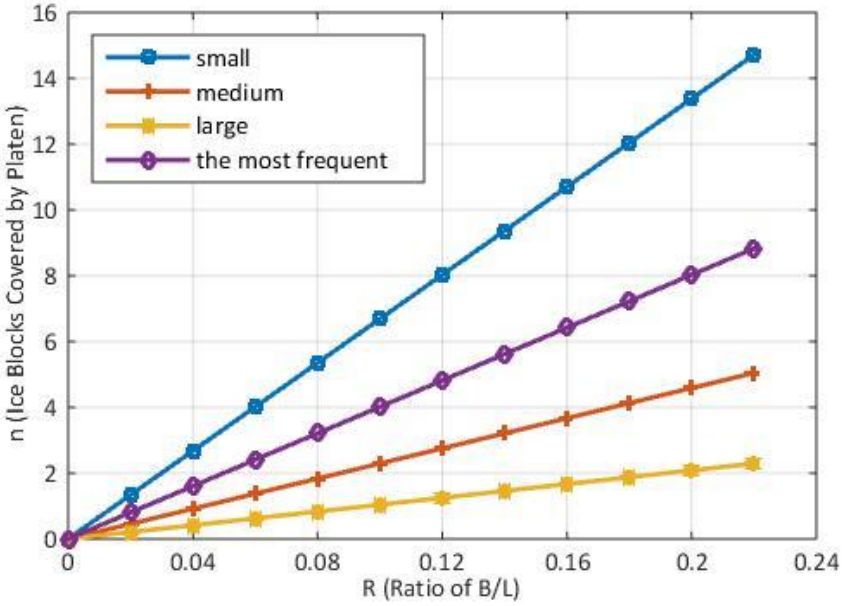

Figure A.2. Ratio for ice covered by platen

Lemee and Brown (2002) realized that in larger ice block tests a higher portion of the ice rubble is displaced downwards, which is called “effective width”. According to the effective width, the nominal platen width should be reduced enough to push down the

target width of ice rubble. In order to estimate the effective platen width, an assumption is made that if half or more of the ice block is in contact with the platen, it will be pushed down. Otherwise, it will rotate as illustrated in Figure A.3. In this estimation, the ratios of $R = 0.2$ ($B = 60cm$) and $R = 0.15$ ($B = 45cm$) are defined as higher and lower limits with regards to the minimum allowable ice rubble numbers. As a result, the modified platen width that roughly pushes the same amount of ice rubble is $0.45m$ and $0.35m$ for the ratios 0.2 and 0.15, respectively. In this experiment, the average of these two results ($0.45m$ and $0.35m$) is found appropriate for the punch box, which gives $B = 40cm$. Furthermore, the ratio R is about 0.13 which shows that the surrounding walls will have lower effects on the shear failure.

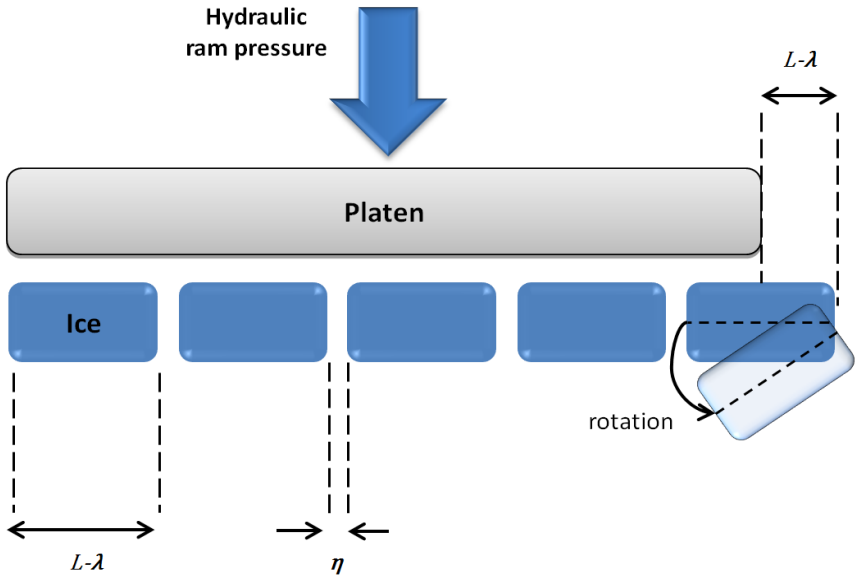

Figure A.3. The platen is shown only covering a portion of the block

Appendix B: Block Dimension Analysis

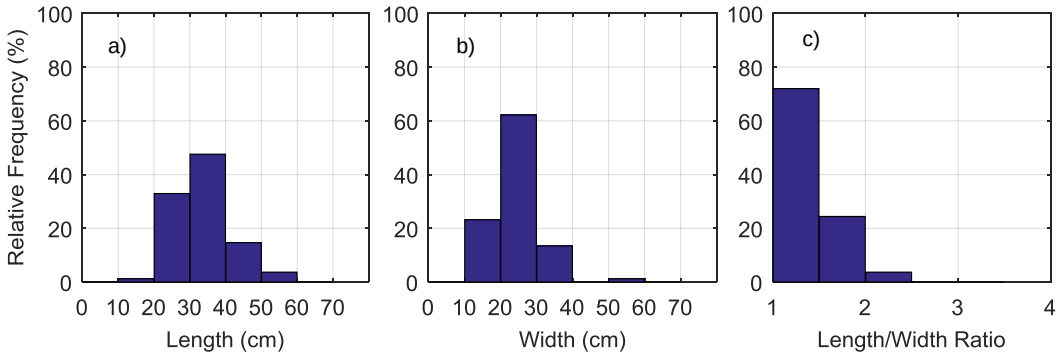

Figure B.1. Histograms of the length (a), width (b) and length to width ratio (c) of the ice blocks for consolidation time of 0.2 hours (Test 1).

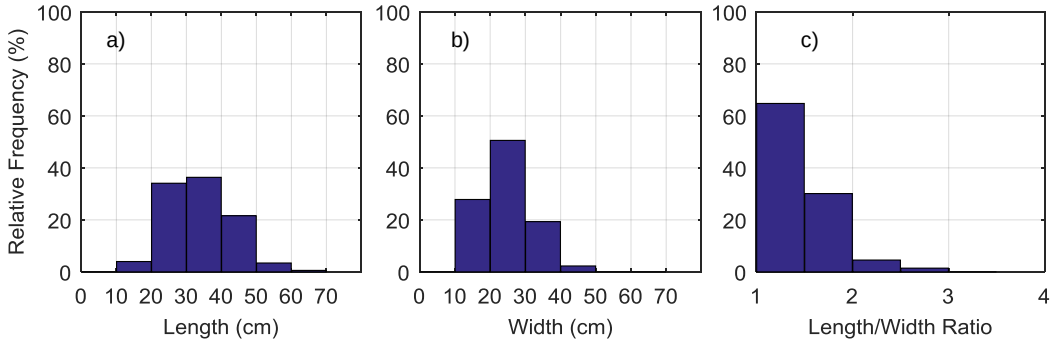

Figure B.2. Histograms of the length (a), width (b) and length to width ratio (c) of the ice blocks for consolidation time of 4.2 hours (Test 3).

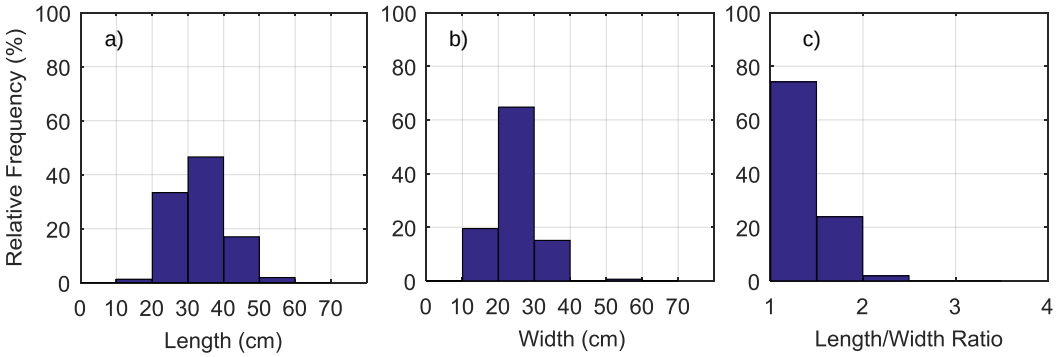

Figure B.3. Histograms of the length (a), width (b) and length to width ratio (c) of the ice blocks for consolidation time of 10.1 hours (Test 5).

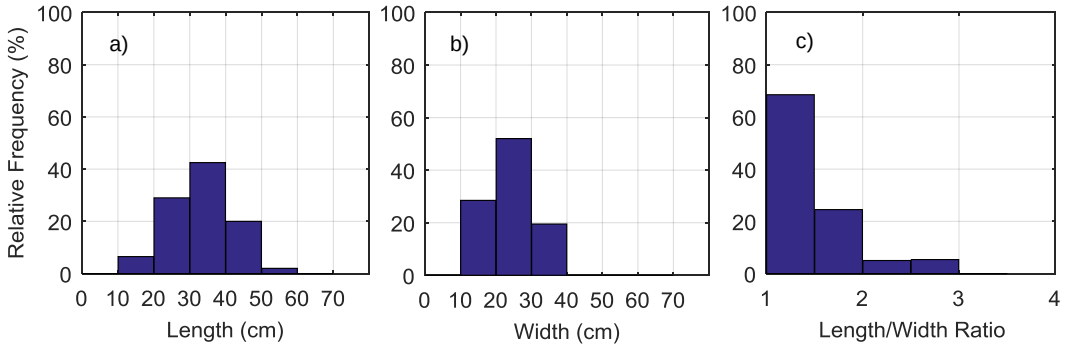

Figure B.4. Histograms of the length (a), width (b) and length to width ratio (c) of the ice blocks for consolidation time of 28.5 hours (Test 6).

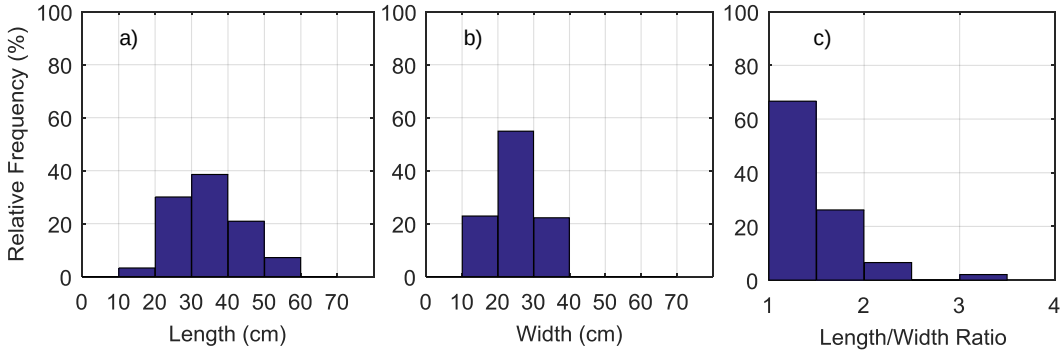

Figure B.5. Histograms of the length (a), width (b) and length to width ratio (c) of the ice blocks for consolidation time of 70.5 hours (Test 7).

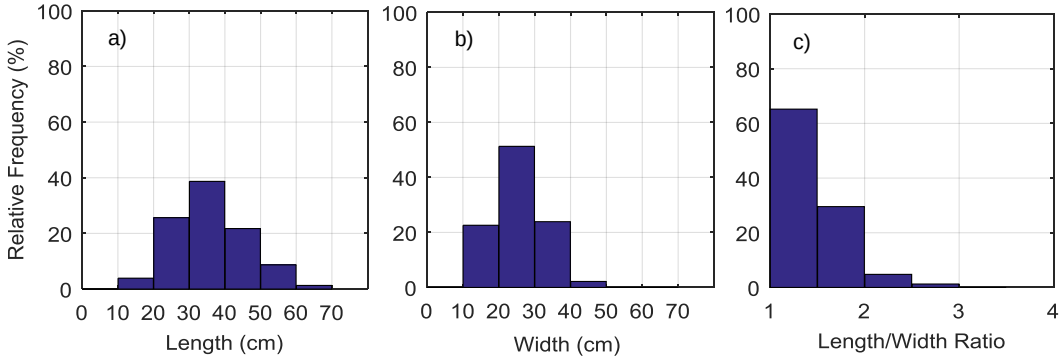

Figure B.6. Histograms of the length (a), width (b) and length to width ratio (c) of the ice blocks for consolidation time of 0.5 hours (Shakedown Test 2).

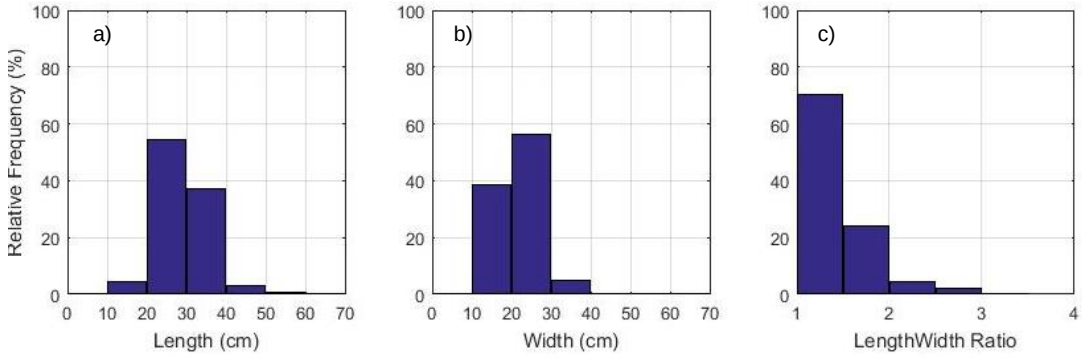

Figure B.7. Histograms of the length (a), width (b) and length to width ratio (c) for the small blocks test (Test 19).

Appendix C: Shakedown tests

Table C.1. Test matrix (shakedown tests)

Test number	Pressure confinement (kPa)	Initial ice temperature (°C)	Consolidation time (hrs) for 0kPa confinement	Block size
Test 1	0	-18	72	Same as DIRKS (Length 30-40 cm; Width 20-30 cm)
Test 2	0		0.5	
Test 3	0		72	
Test 4	0		4	
Test 5	0		4	
Test 6	10		4	
Test 7	10		4	

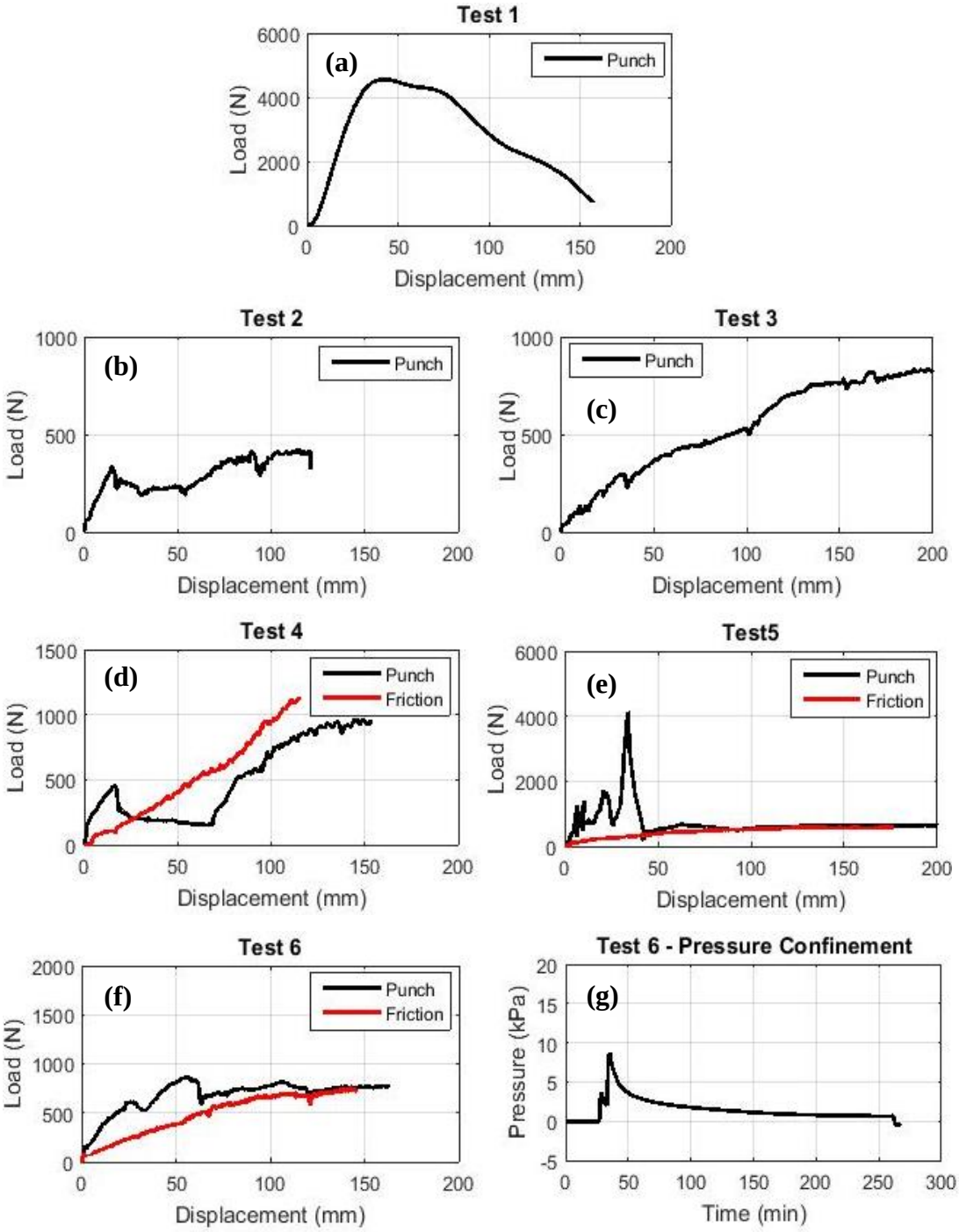

[Continued on page 156]

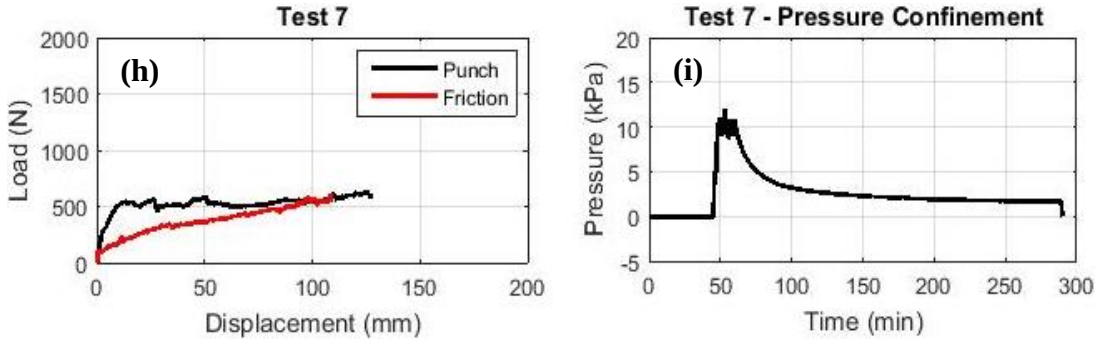

Figure C.1. Load-displacement and the history of consolidation time (Shakedown tests).

Appendix D: Temperature Data

Test 1:

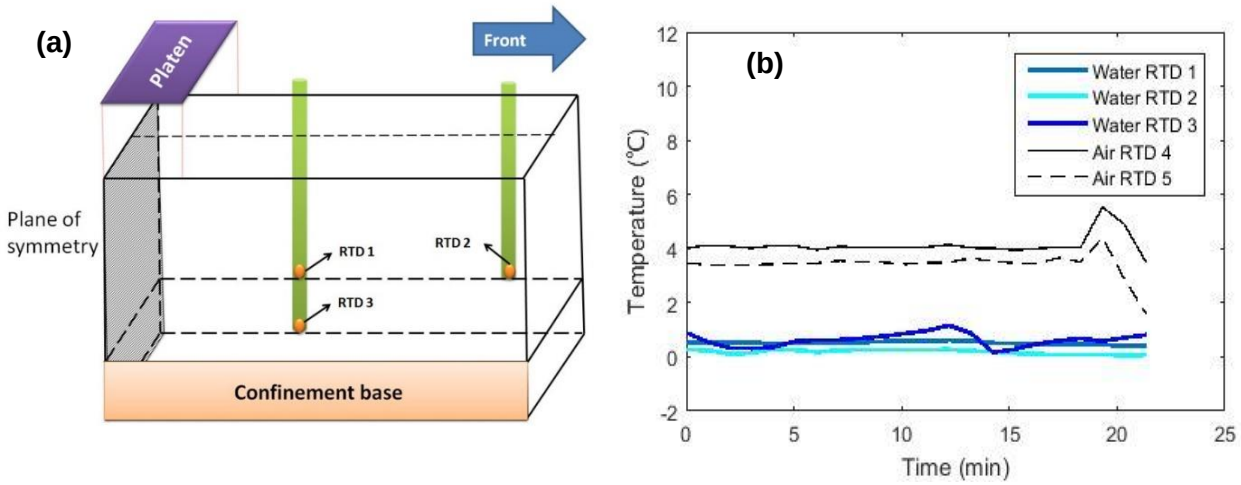

Figure D.1. Schematic showing the position of RTDs (a) and the water and air temperatures measured by the RTDs (b) for the 0.2 hours test. Note no internal ice block measurement were measured for this test.

Test 2:

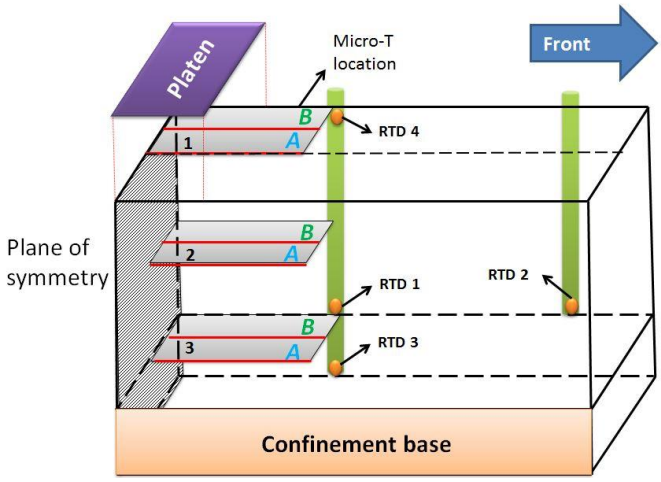

Location	Maximum length (cm)	Volume (cm^3)
1A	29	3987
1B	55	18967
2A	44	17469
2B	40	9874
3A	39	10703
3B	43	18680

Figure D.2. Position and dimensions of the ice blocks containing Micro-Ts and RTDs for the 2.4 hours test.

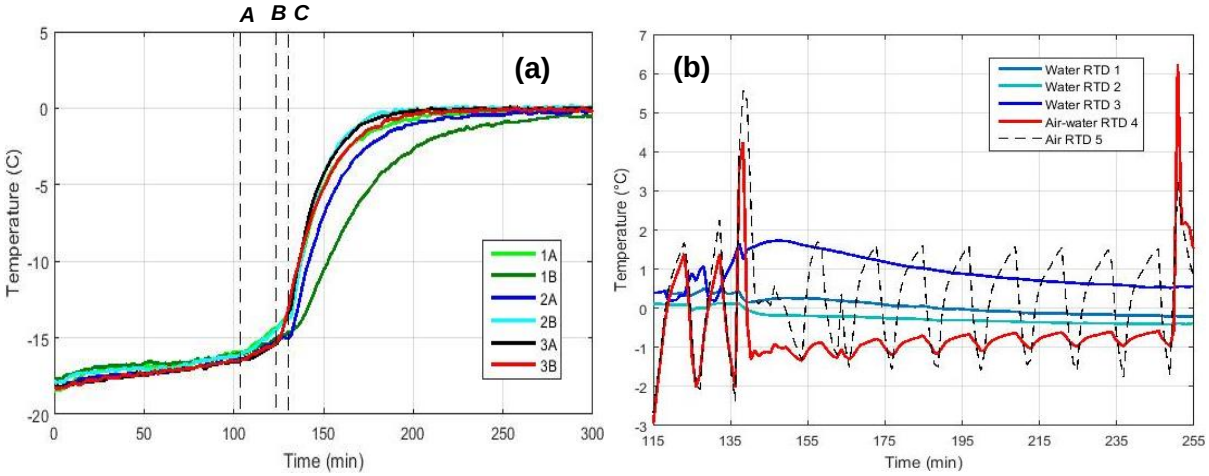

Figure D.3. Plots showing (a) the internal ice block temperature measured by the Micro-T sensors and (b) the water and air temperatures measured by the RTDs for the 2.4 hours test.

Test 3:

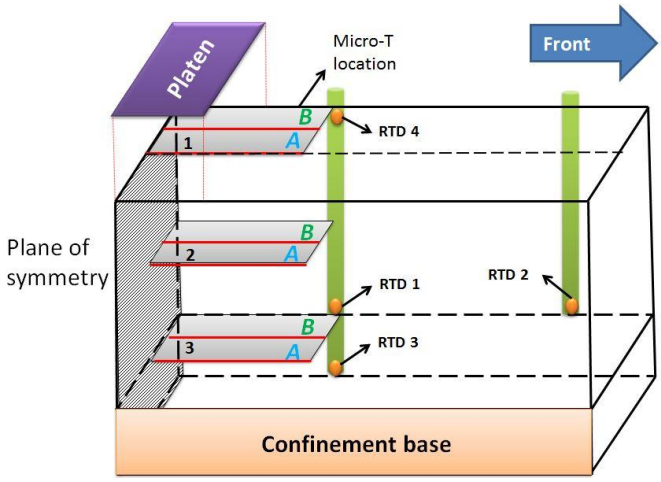

Location	Maximum length (cm)	Volume (cm^3)
1A	60	11921
1B	40	9005
2A	61	14170
2B	42	5786
3A	52	13035
3B	36	6389

Figure D.4. Position and dimensions of the ice blocks containing Micro-Ts and RTDs for the 4.2 hours test.

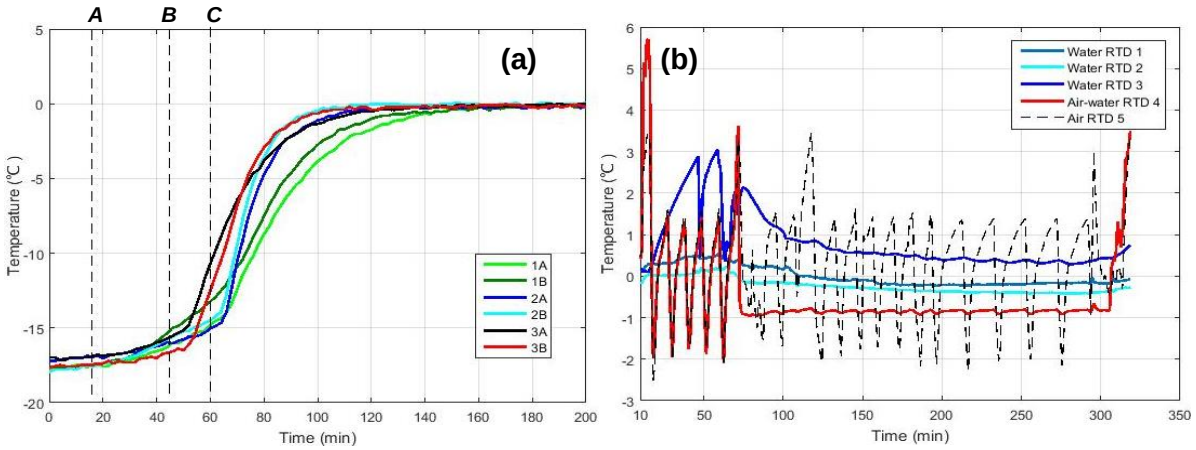

Figure D.5. Plots showing (a) the internal ice block temperature measured by the Micro-T sensors and (b) the water and air temperatures measured by the RTDs for the 4.2 hours test.

Test 4:

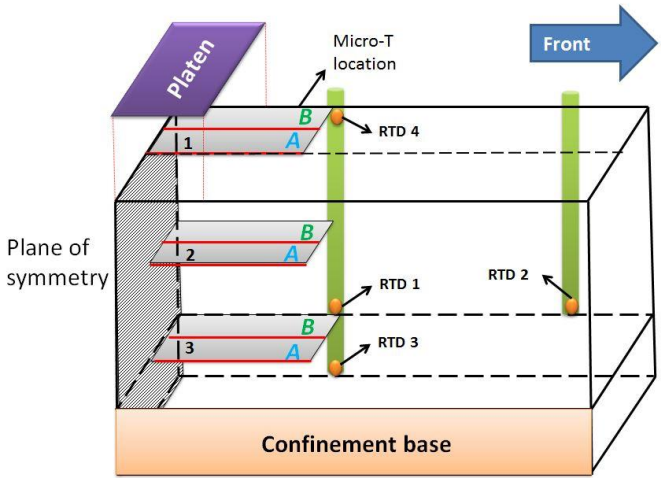

Location	Maximum length (cm)	Volume (cm^3)
1A	36	8197
1B	39	9287
2A	36	7841
2B	44	7267
3A	26	3928
3B	49	9380

Figure D.6. Position and dimensions of the ice blocks containing Micro-Ts and RTDs for the 4.4 hours test.

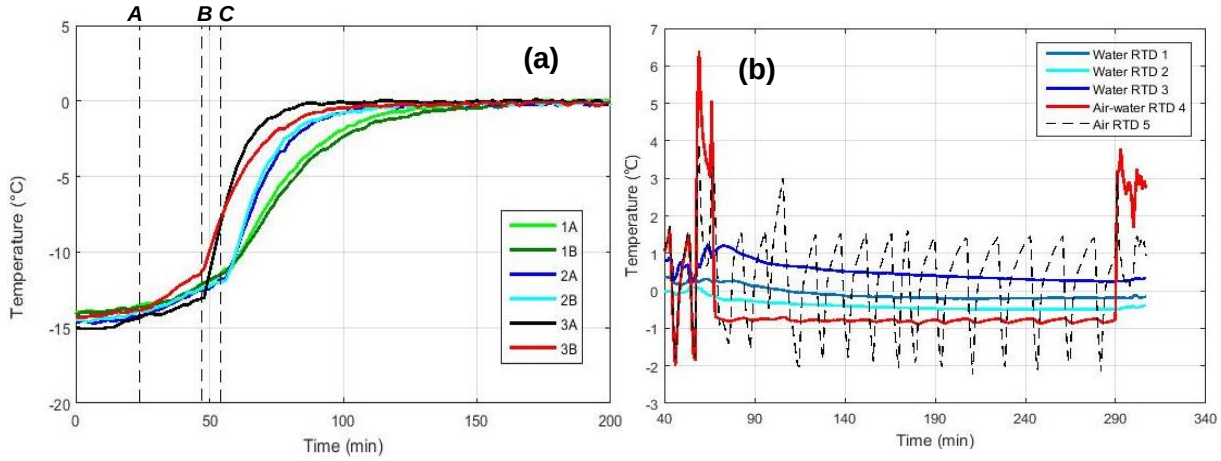

Figure D.7. Plots showing (a) the internal ice block temperature measured by the Micro-T sensors and (b) the water and air temperatures measured by the RTDs for the 4.4 hours test.

Test 5:

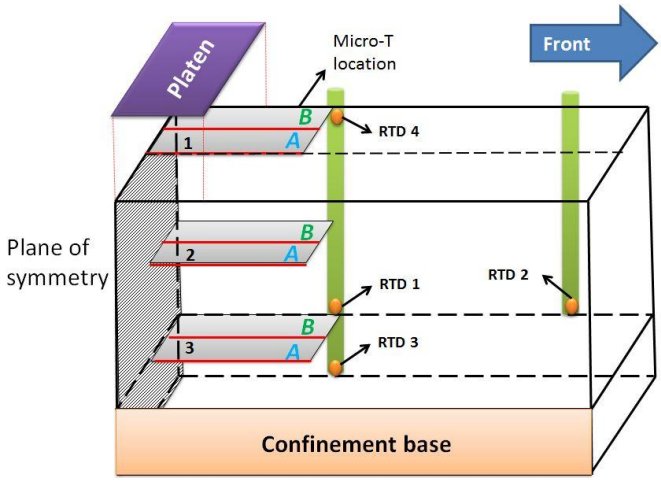

Location	Maximum length (cm)	Volume (cm^3)
1A	43	9142
1B	53	13190
2A	35	5483
2B	61	24791
3A	36	7674
3B	46	12697

Figure D.8. Position and dimensions of the ice blocks containing Micro-Ts and RTDs for the 10.1 hours test.

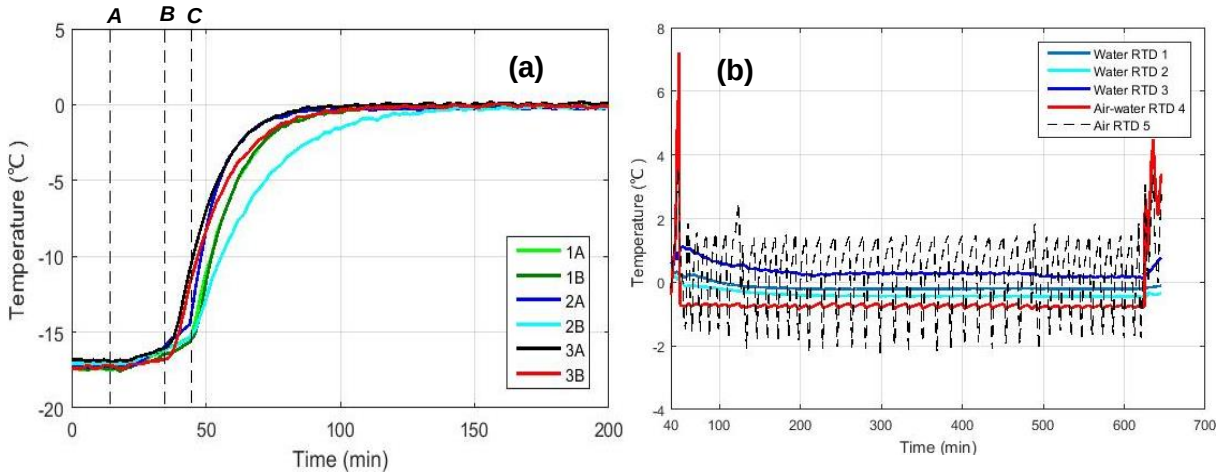

Figure D.9. Plots showing (a) the internal ice block temperature measured by the Micro-T sensors and (b) the water and air temperatures measured by the RTDs for the 10.1 hours test.

Test 6:

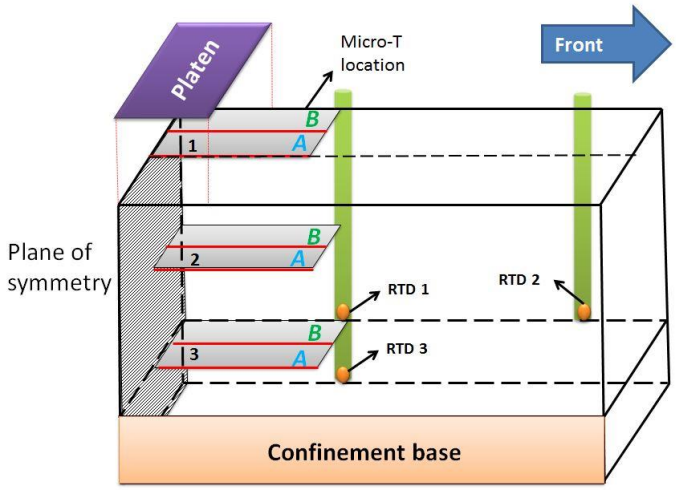

Location	Maximum length (cm)	Volume (cm^3)
1A	33	7103
1B	36	9304
2A	40	11832
2B	38	10380
3A	40	7206
3B	58	2026

Figure D.10. Position and dimensions of the ice blocks containing Micro-Ts and RTDs for the 28.5 hours test.

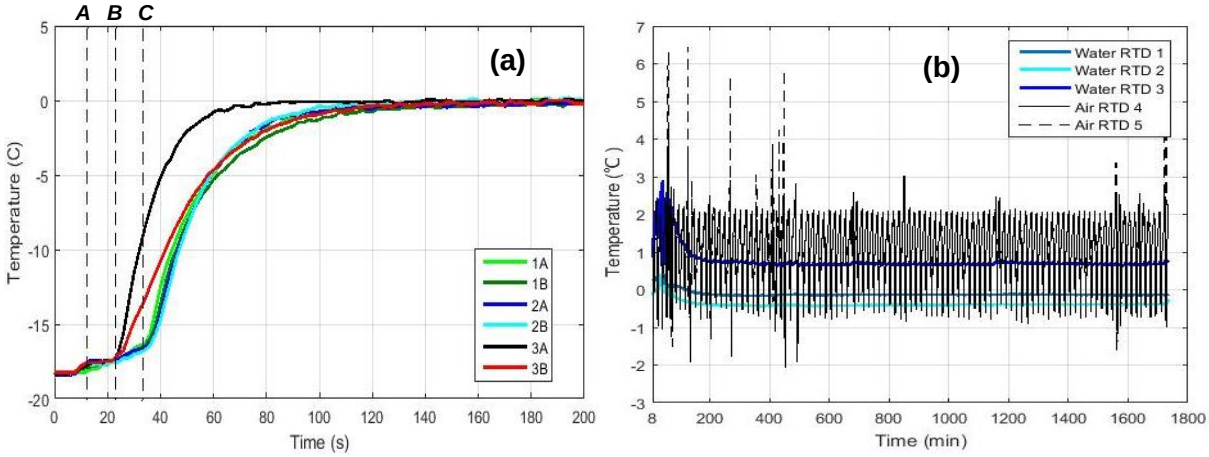

Figure D.11. Plots showing (a) the internal ice block temperature measured by the Micro-T sensors and (b) the water and air temperatures measured by the RTDs for the 28.5 hours test.

Test 7:

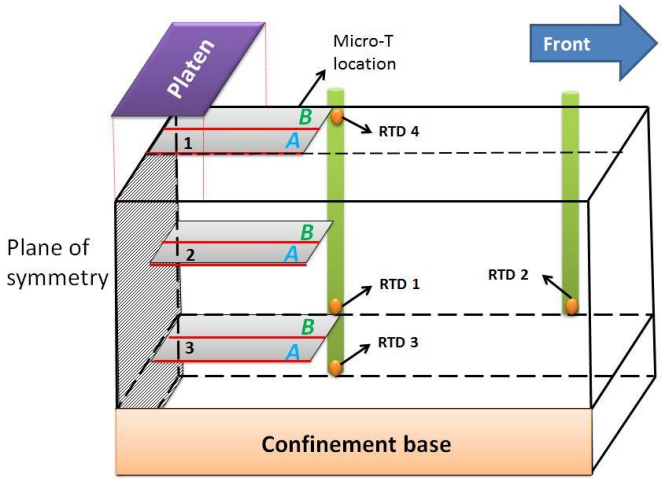

Location	Maximum length (cm)	Volume (cm^3)
1A	39	6317
1B	39	8839
2A	38	5934
2B	59	15182
3A	33	8684
3B	49	17080

Figure D.12. Position and dimensions of the ice blocks containing Micro-Ts and RTDs for the 70.5 hours test.

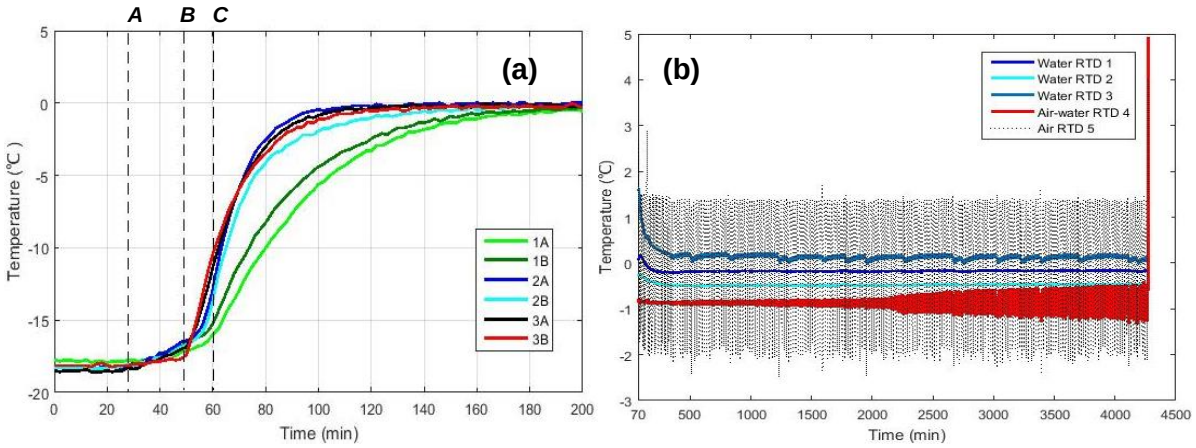

Figure D.13. Plots showing (a) the internal ice block temperature measured by the Micro-T sensors and (b) the water and air temperatures measured by the RTDs for the 70.5 hours test.

Test 8:

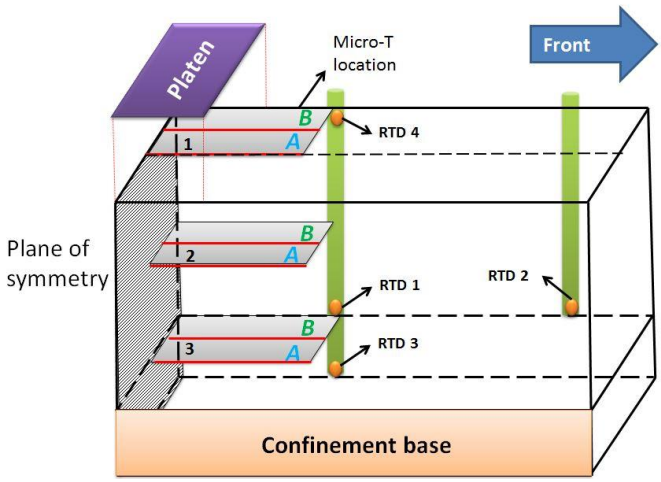

Location	Maximum length (cm)	Volume (cm^3)
1A	50	11727
1B	40	8920
2A	39	8550
2B	53	18705
3A	32	5373
3B	33	9040

Figure D.14. Position and dimensions of the ice blocks containing Micro-Ts and RTDs for the 0kPa pressure confinement.

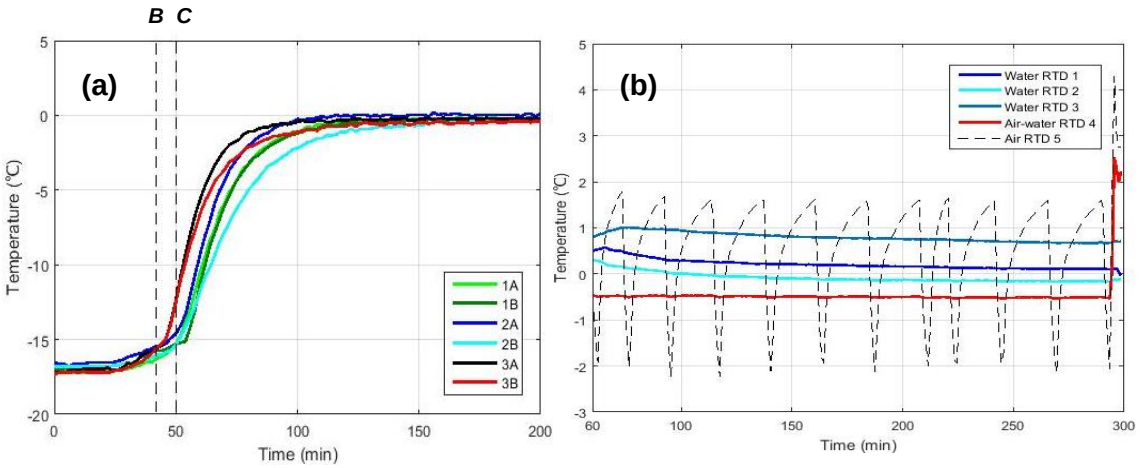

Figure D.15. Plots showing (a) the internal ice block temperature measured by the Micro-T sensors and (b) the water and air temperatures measured by the RTDs for the 0kPa pressure confinement.

Test 9:

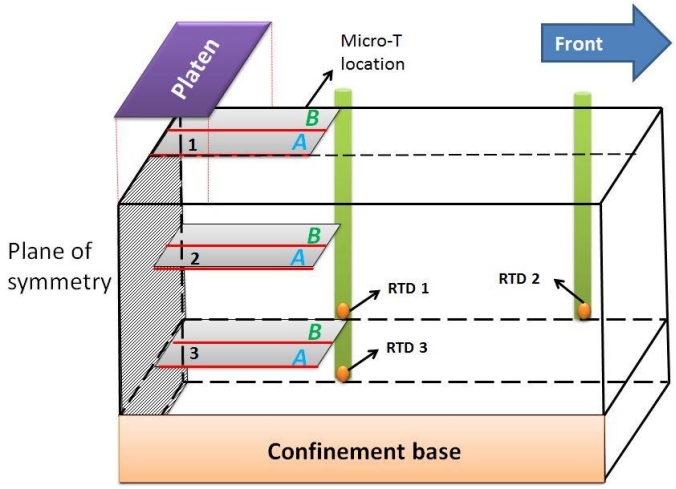

Location	Maximum length (cm)	Volume (cm^3)
1A	40	14065
1B	43	11951
2A	33	5667
2B	31	7699
3A	38	6674
3B	53	20188

Figure D.16. Position and dimensions of the ice blocks containing Micro-Ts and RTDs for the 10kPa pressure confinement.

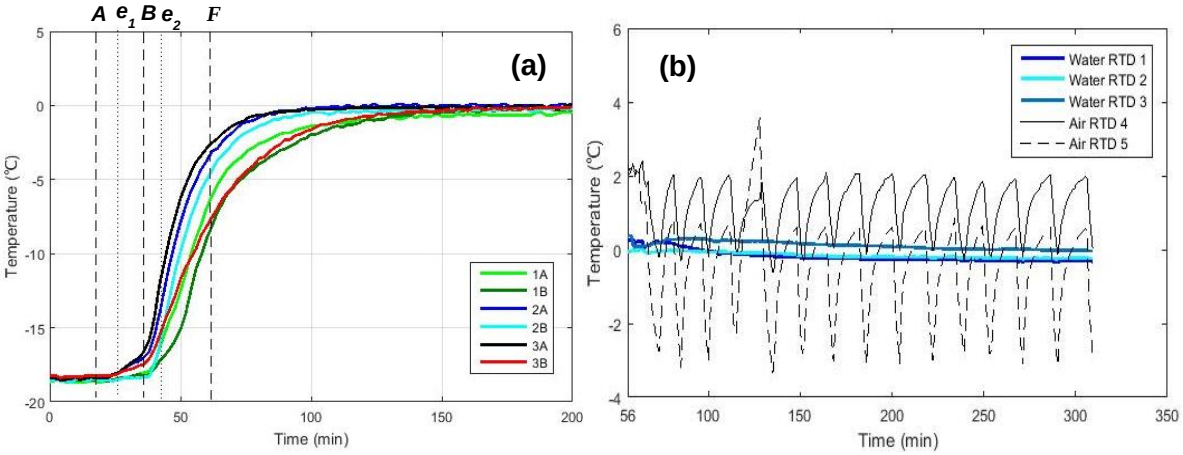

Figure D.17. Plots showing (a) the internal ice block temperature measured by the Micro-T sensors and (b) the water and air temperatures measured by the RTDs for the 10kPa pressure confinement.

Test 10:

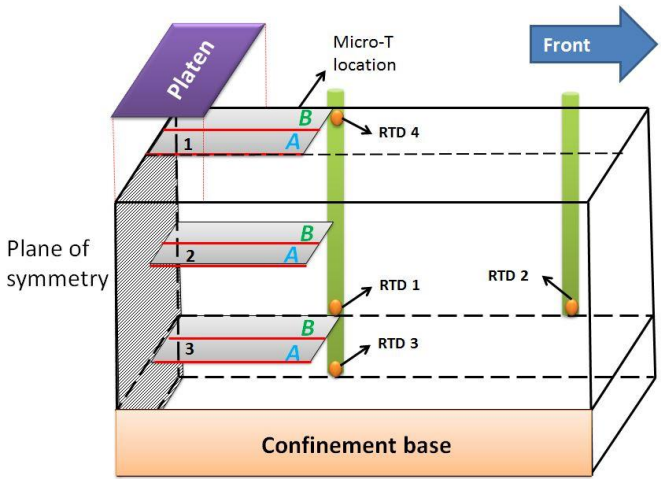

Location	Maximum length (cm)	Volume (cm^3)
1A	42	5742
1B	33	6838
2A	33	7033
2B	55	10415
3A	49	12626
3B	36	6825

Figure D.18. Position and dimensions of the ice blocks containing Micro-Ts and RTDs for the 10kPa pressure confinement.

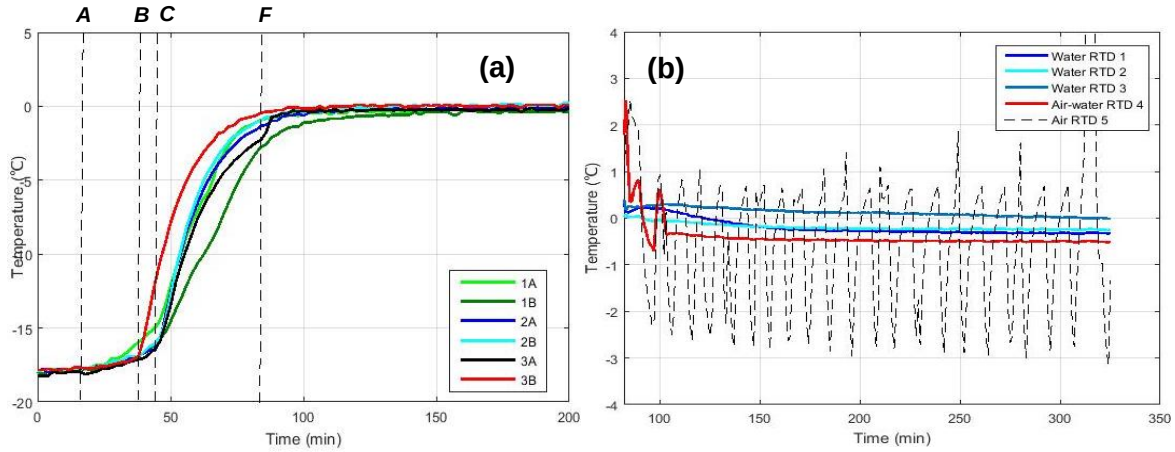

Figure D.19. Plots showing (a) the internal ice block temperature measured by the Micro-T sensors and (b) the water and air temperatures measured by the RTDs for the 10kPa pressure confinement.

Test 11:

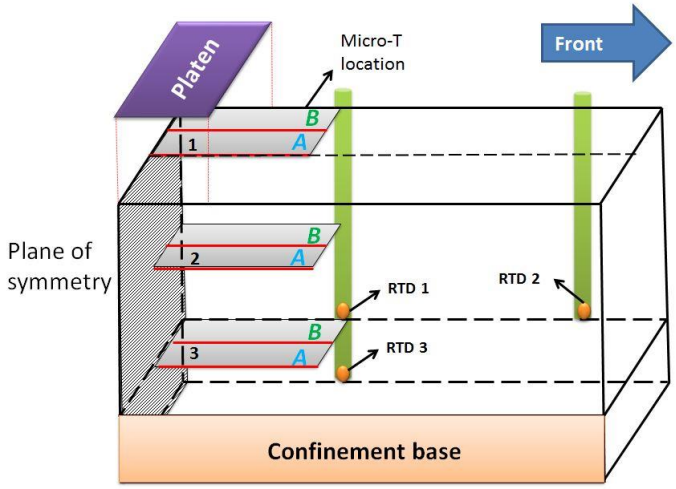

Location	Maximum length (cm)	Volume (cm^3)
1A	49	16182
1B	28	7417
2A	44	10734
2B	30	4741
3A	30	5313
3B	34	6731

Figure D.20. Position and dimensions of the ice blocks containing Micro-Ts and RTDs for the 25kPa pressure confinement.

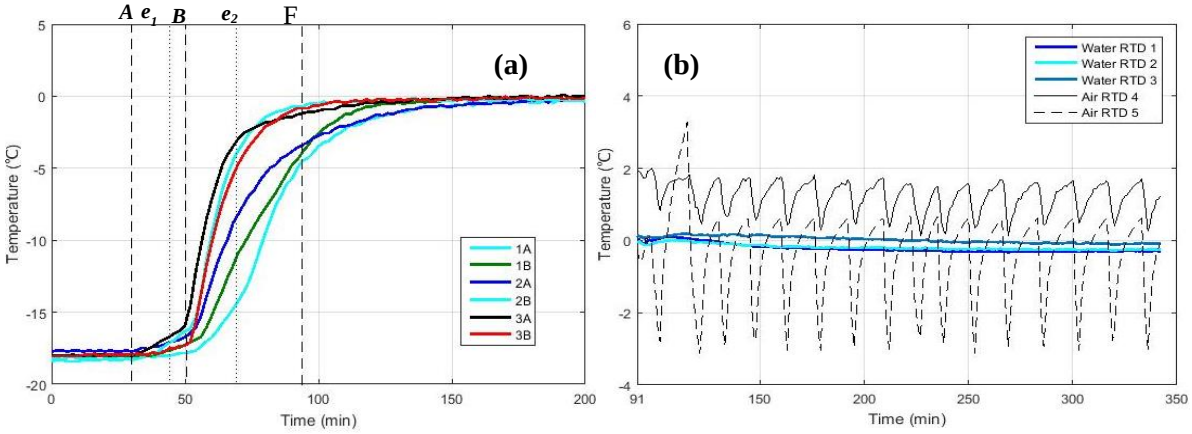

Figure D.21. Plots showing (a) the internal ice block temperature measured by the Micro-T sensors and (b) the water and air temperatures measured by the RTDs for the 25kPa pressure confinement.

Test 12:

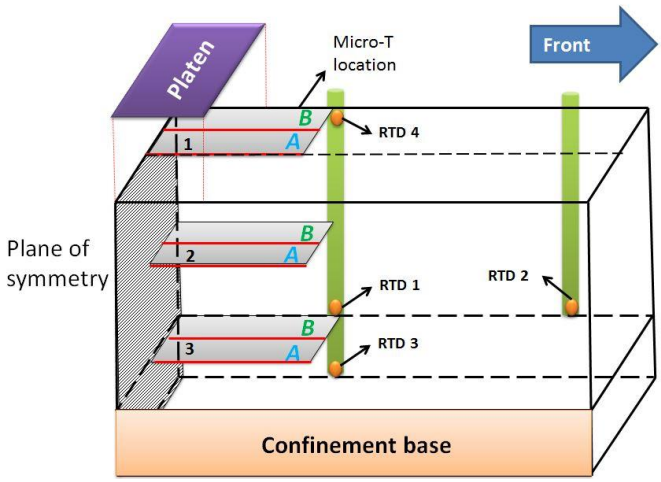

Location	Maximum length (cm)	Volume (cm^3)
1A	46	12437
1B	34	5427
4A	55	23102
4B	44	14439

Figure D.22. Position and dimensions of the ice blocks containing Micro-Ts and RTDs for the 25kPa pressure confinement.

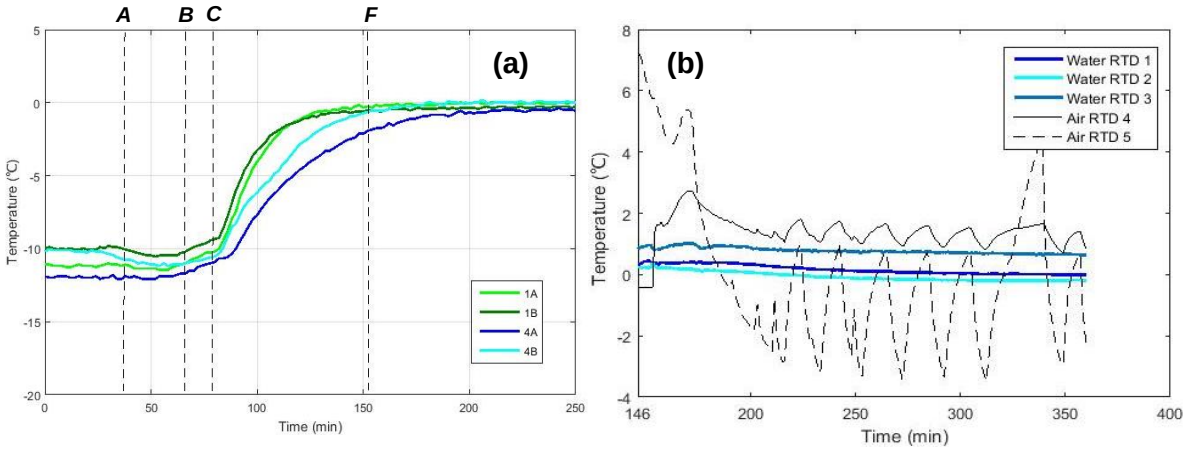

Figure D.23. Plots showing (a) the internal ice block temperature measured by the Micro-T sensors and (b) the water and air temperatures measured by the RTDs for the 25kPa pressure confinement.

Test 13:

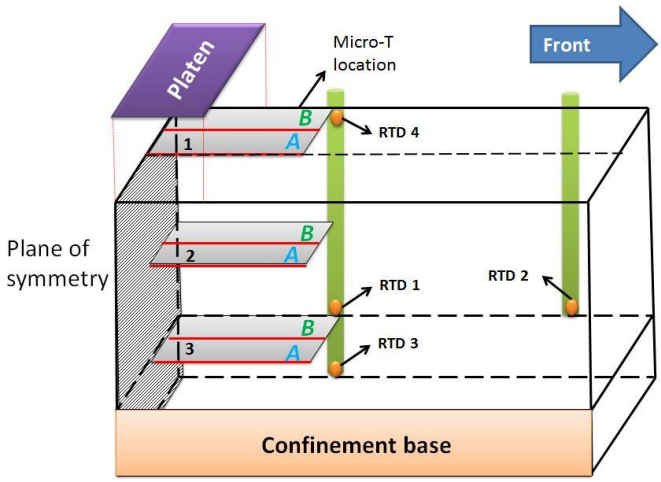

Location	Maximum length (cm)	Volume (cm^3)
1A	37	8802
1B	43	11123
2A	52	12621
2B	34	4458
3A	55	16186
3B	40	7676

Figure D.24. Position and dimensions of the ice blocks containing Micro-Ts and RTDs for the 40kPa pressure confinement.

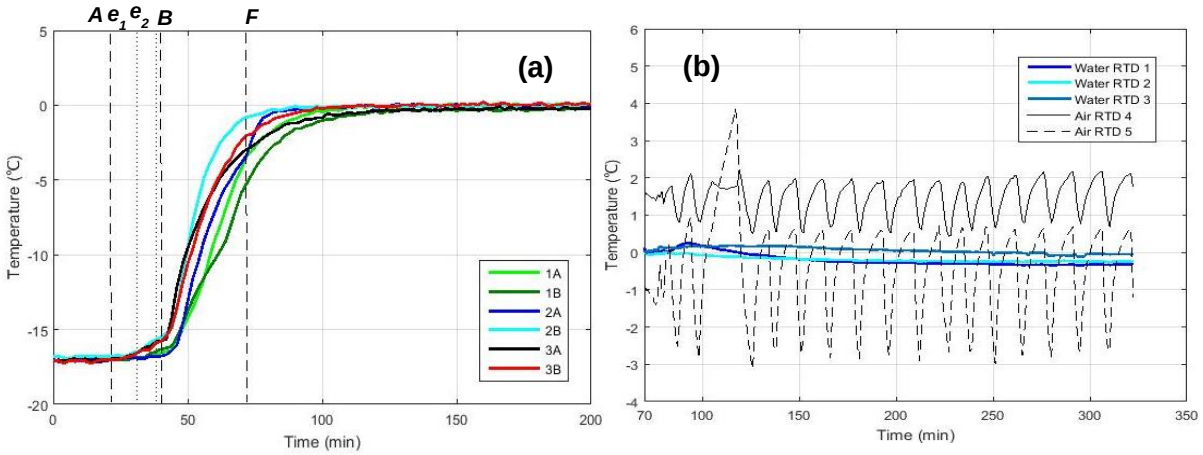

Figure D.25. Plots showing (a) the internal ice block temperature measured by the Micro-T sensors and (b) the water and air temperatures measured by the RTDs for the 40kPa pressure confinement.

Tet 14:

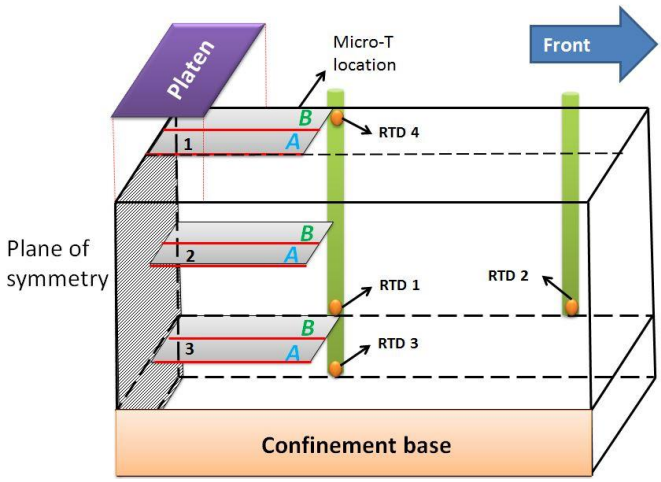

Location	Maximum length (cm)	Volume (cm^3)
1A	55	21850
1B	48	14355
2A	37	8644
2B	44	12756
3A	44	6793
3B	40	9077

Figure D.26. Position and dimensions of the ice blocks containing Micro-Ts and RTDs for the 40kPa pressure confinement.

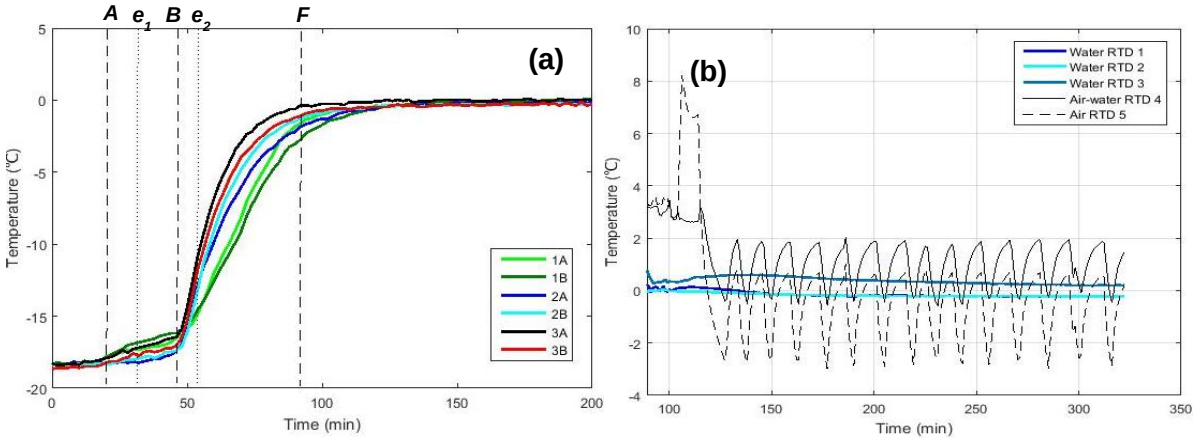

Figure D.27. Plots showing (a) the internal ice block temperature measured by the Micro-T sensors and (b) the water and air temperatures measured by the RTDs for the 40kPa pressure confinement.

Test 15

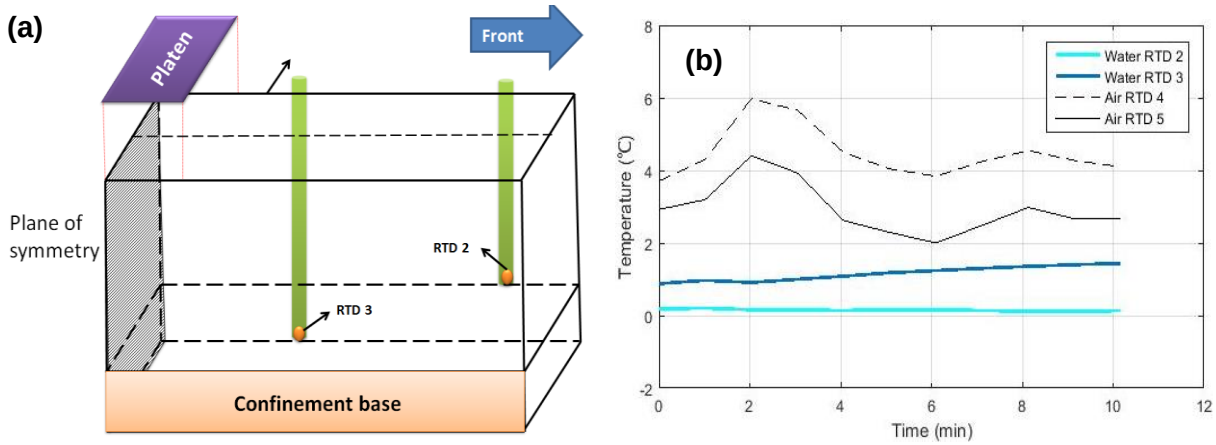

Figure D.28. Schematic showing the position of RTDs (a) and the water and air temperatures measured by the RTDs (b) for the 0.3 hours test. Note no internal ice block measurement were measured for this test.

Test 16

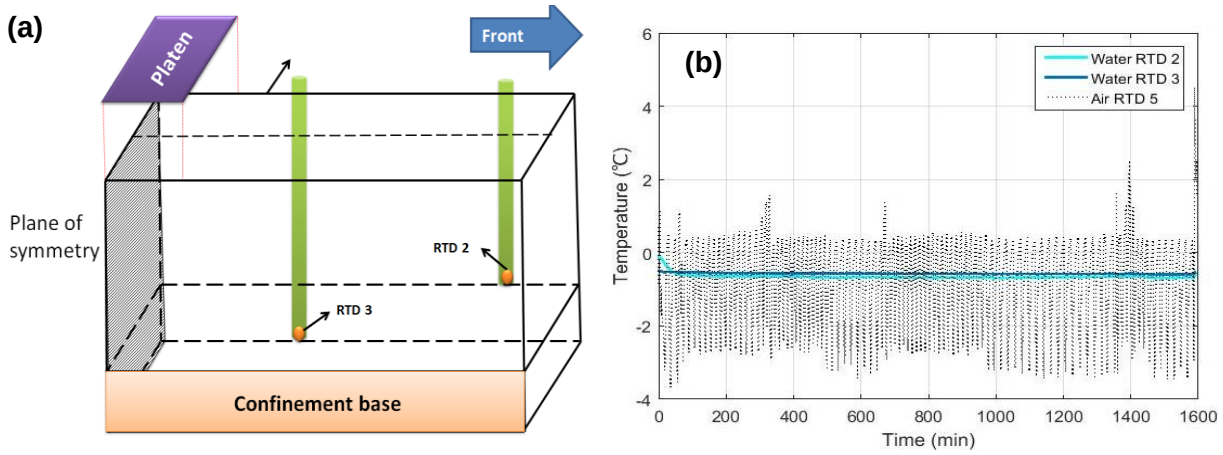

Figure D.29. Schematic showing the position of RTDs (a) and the water and air temperatures measured by the RTDs (b) for the 25 hours test. Note no internal ice block measurement were measured for this test.

Test 17

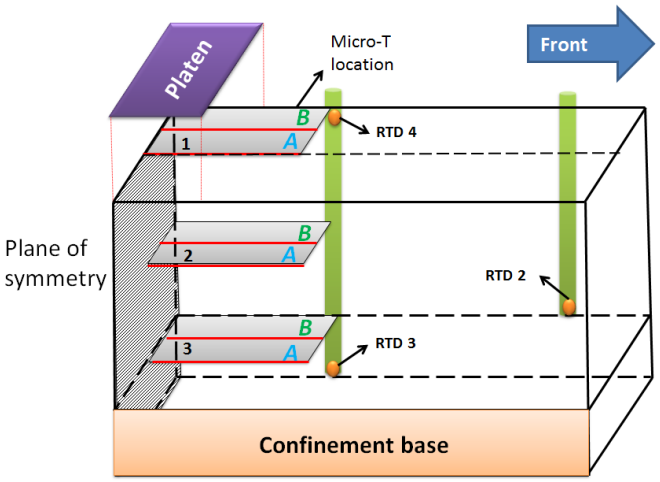

Location	Maximum length (cm)	Volume (cm^3)
1A	-	-
1B	33	8656
2A	41	11700
2B	35	8567
3A	36	9247
3B	36	9166

Figure D.30. Position and dimensions of the ice blocks containing Micro-Ts and RTDs for the 66.2 hours consolidation time.

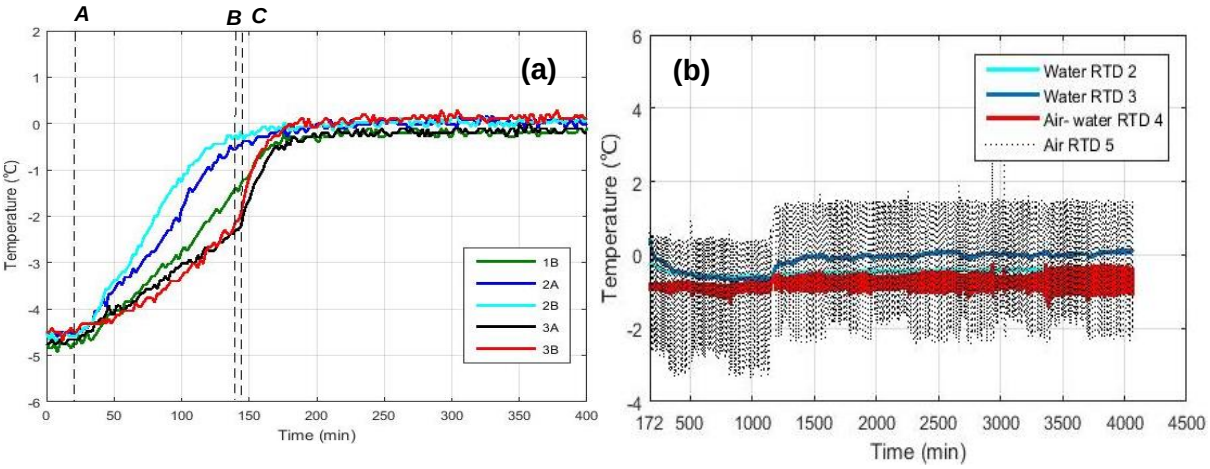

Figure D.31. Plots showing (a) the internal ice block temperature measured by the Micro-T sensors and (b) the water and air temperatures measured by the RTDs for the 66.2 hours consolidation time.

Test 18

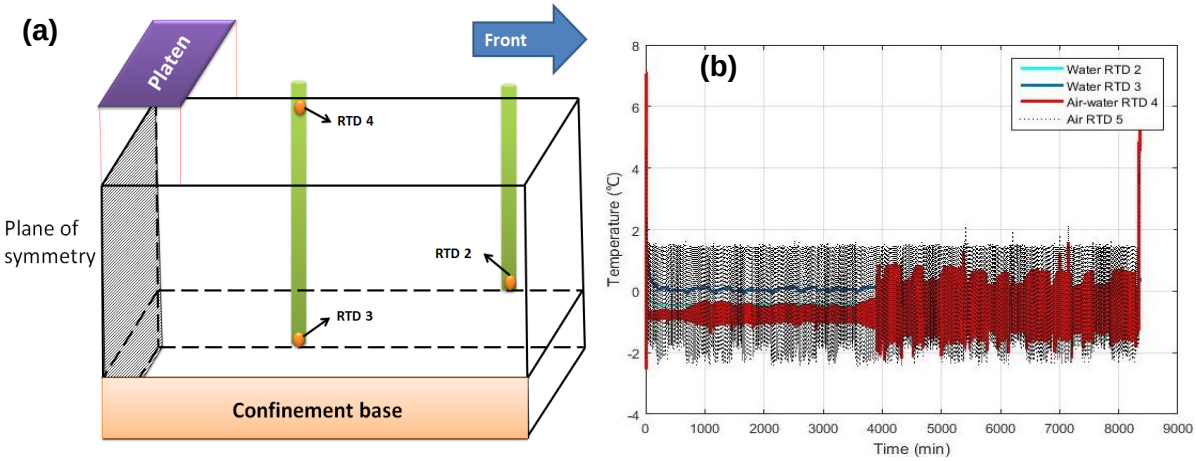

Figure D.32. Schematic showing the position of RTDs (a) and the water and air temperatures measured by the RTDs (b) for the 139.7 hours test. Note no internal ice block measurement were measured for this test.

Test 19

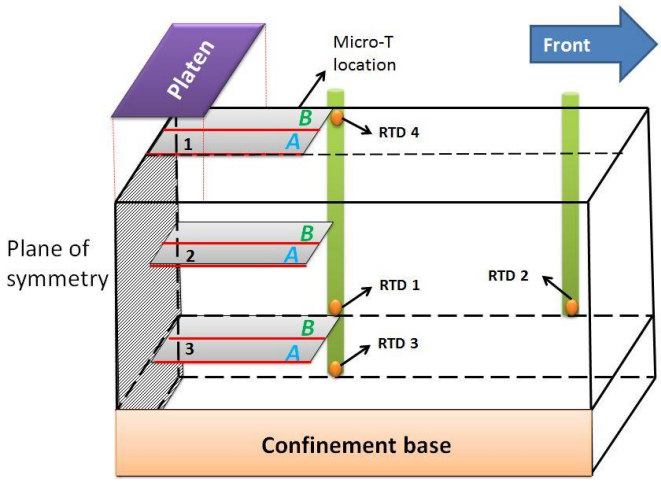

Location	Maximum length (cm)	Volume (cm^3)
1A	24	3998
1B	25	3735
2A	30	4753
2B	27	5658
3A	30	7681
3B	34	6926

Figure D.33. Position and dimensions of the ice blocks containing Micro-Ts and RTDs for the small blocks test.

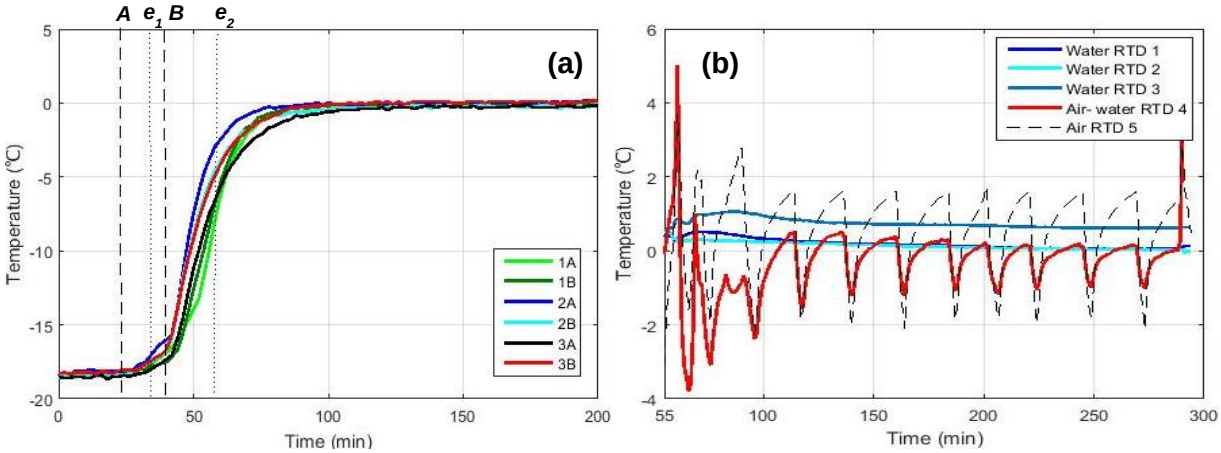

Figure D.34. Plots showing (a) the internal ice block temperature measured by the Micro-T sensors and (b) the water and air temperatures measured by the RTDs for the small blocks test.

Appendix E: Porosity estimation

Two methods were used to estimate ice rubble beam porosity.

Method I:

In this method, it is assumed that the volume of water before and after filling the box is constant. Therefore, Equation (E.1) can be defined:

$$\text{Volume}_{\text{water,1}} = \text{Volume}_{\text{water,2}} \quad \text{(E.1)}$$

According to Figure E.1, Equation (E.2) can be derived:

$$A_{box} h_1 = A_{box} h_2 - (1 - \eta)\, A_{block} H_s \quad \text{(E.2)}$$

By assuming that the box area (A_{box}) and the ice rubble beam plane area (A_{block}) are equal, Equation (E.2) can be modified to:

$$h_1 = h_2 - (1 - \eta) H_s \quad \text{(E.3)}$$

Therefore, the porosity based on Method I can be derived from (E.4):

$$\eta = 1 - \frac{h_2 - h_1}{H_s} \quad \text{(E.4)}$$

Method II:

In Method II, by assuming that the ice rubble beam is in hydrostatic equilibrium, (E.5) can be defined:

$$F_B = F_g \tag{E.5}$$

In which, F_B and F_g are buoyancy force and gravity force, respectively, which are defined as following:

$$F_B = \rho_w g(1-\eta)V_{\text{sumberged beam}} \tag{E.6}$$

$$F_g = m_{ice} g \tag{E.7}$$

By combining Equation (E.6) and Equation (E.7), the porosity can be derived as following:

$$\eta = 1 - \frac{m_{ice}}{\rho_w V_{sumberged\ beam}} \tag{E.8}$$

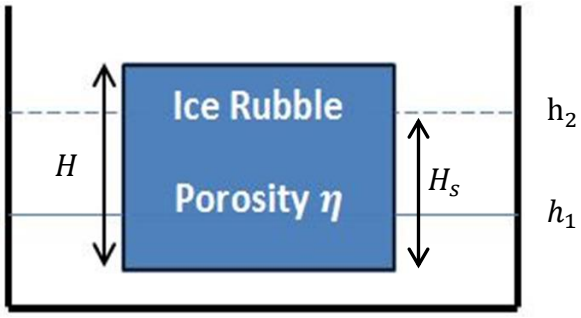

Figure E.1. The changes of water level from h_1 to h_2 after filling the box by ice rubble

Appendix F: Buoyancy of Platen

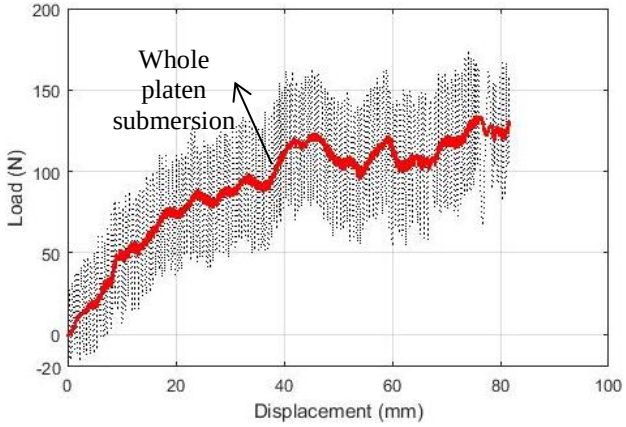

Figure F.1. Load-displacement for buoyancy test.

Appendix G: Shear and flexural strength

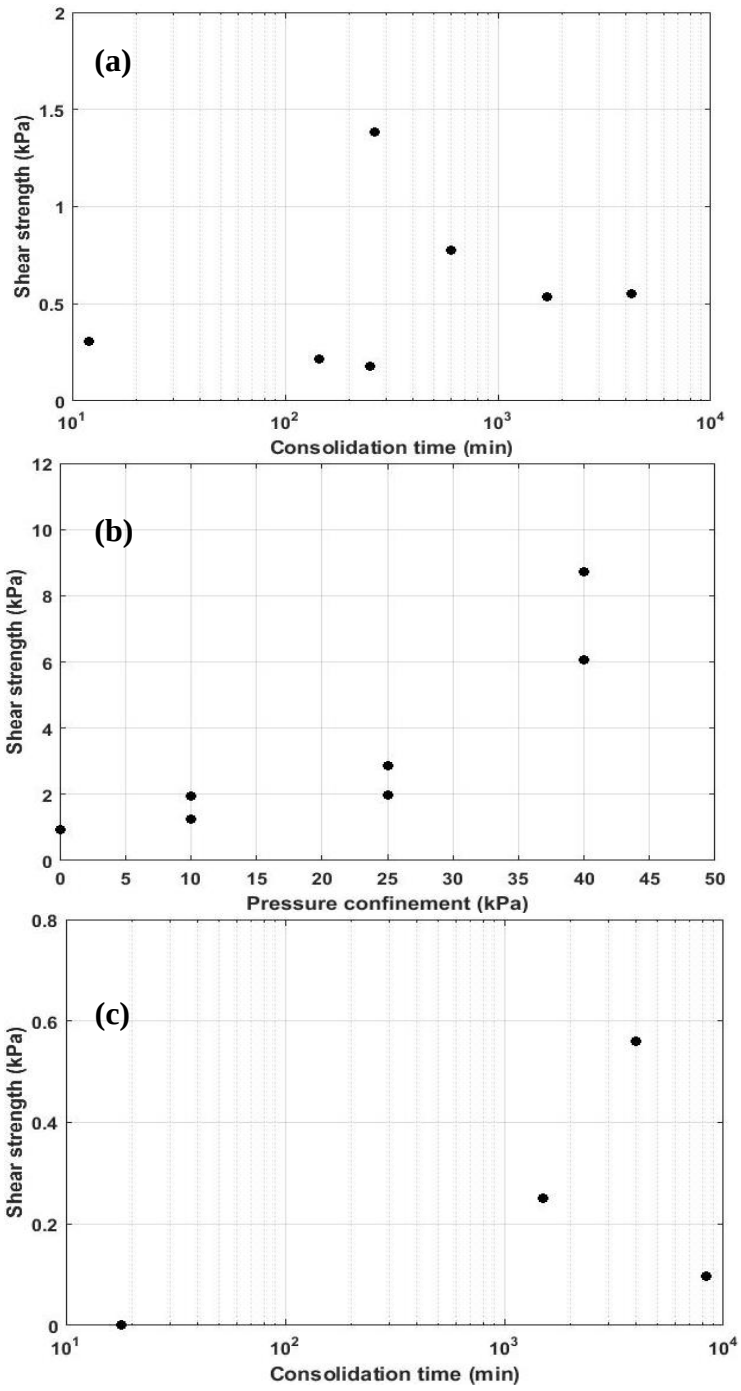

Figure G.1. The shear strength of a) consolidation time tests (Phase I); b) pressure confinement tests (Phase II); and c) sintering tests (Phase III).

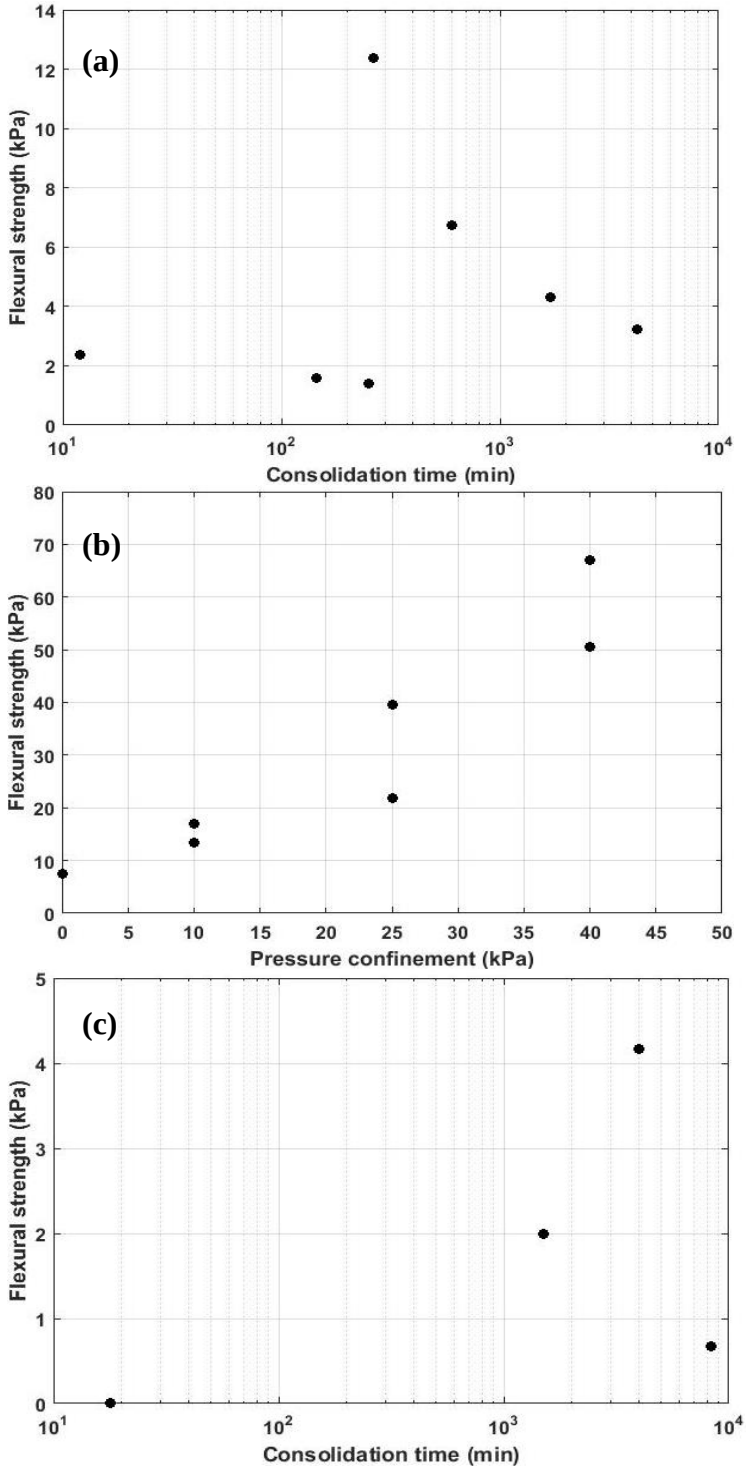

Figure G.2. The flexural strength in a) consolidation time tests (Phase I); b) pressure confinement tests (Phase II); and c) sintering tests (Phase III).

Appendix H: Ice block FB formation

Test 2

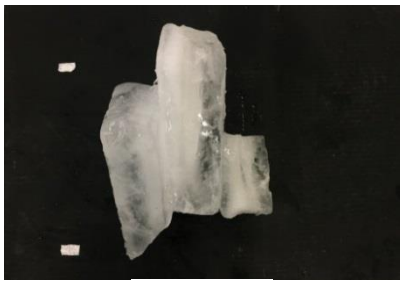

Test 3

Test 4

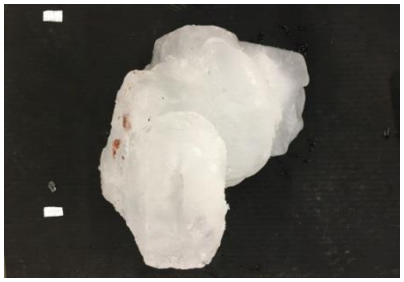

Test 5

Test 6

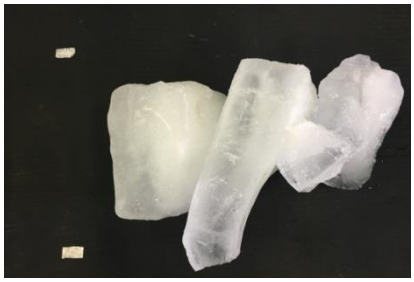

Test 6

Test 7

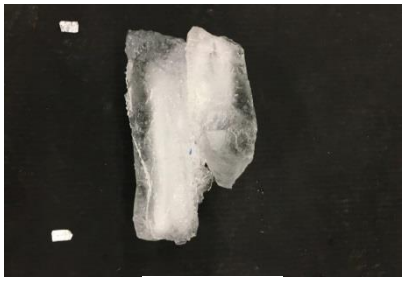

Test 16

Test 17

Test 17

Test 18

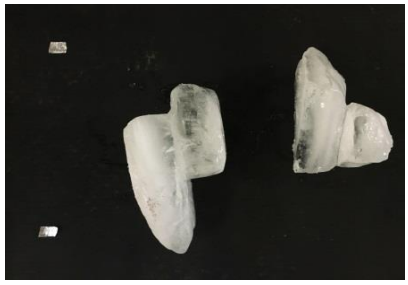

Shakedown Test 2

[Continued on page 182]

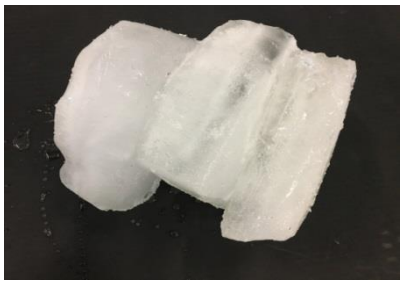

Shakedown Test 6

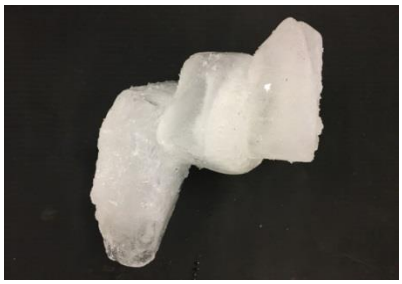

Shakedown Test 6

Figure H.1. Freeze-bond formation

Appendix I: Test setup

(a)

(b)

(c)

[Continued on page 184]

(d)

(e)

(f)

Figure I.1. Test setup.

This page is intentionally left blank